Springer Series in Computational Neuroscience

Ana Rita Londral
Pedro Encarnação
José Luis Pons Rovira *Editors*

Neurotechnology, Electronics, and Informatics

Revised Selected Papers from Neurotechnix 2013

Springer

Springer Series in Computational Neuroscience

Volume 13

More information about this series at http://www.springer.com/series/8164

Ana Rita Londral • Pedro Encarnação
José Luis Pons Rovira
Editors

Neurotechnology, Electronics, and Informatics

Revised Selected Papers from Neurotechnix 2013

Springer

Editors
Ana Rita Londral
Faculty of Medicine
Universidade de Lisboa
Lisboa, Portugal

José Luis Pons Rovira
Bioengineering Group
Spanish Research Council
Arganda del Rey, Madrid, Spain

Pedro Encarnação
Católica Lisbon School of Business
and Economics
Universidade Católica Portuguesa
Lisboa, Portugal

ISSN 2197-1900 ISSN 2197-1919 (electronic)
Springer Series in Computational Neuroscience
ISBN 978-3-319-15996-6 ISBN 978-3-319-15997-3 (eBook)
DOI 10.1007/978-3-319-15997-3

Library of Congress Control Number: 2015940533

Springer Cham Heidelberg New York Dordrecht London

Printed on acid-free paper

Springer International Publishing AG Switzerland is part of Springer Science+Business Media (www.springer.com)

Preface

The present book includes extended and revised versions of a set of selected papers from the *First International Congress on Neurotechnology, Electronics and Informatics* (NEUROTECHNIX 2013), held in Vilamoura, Algarve, Portugal, from 18 to 20 September, 2013.

The purpose of the International Congress on Neurotechnology, Electronics and Informatics is to bring together researchers and practitioners in order to exchange ideas and develop synergies towards new advancements of neurotechnology either in general or regarding a particular case, application or pathology.

NEUROTECHNIX 2013 was co-sponsored by INSTICC (Institute for Systems and Technologies of Information, Control and Communication) and MedinRes – Medical Information and Research, held in cooperation with Neurotech Network, Nansen Neuroscience Network, Associação Portuguesa de EEG e Neurofisiologia Clínica, Sociedade Portuguesa de Neurologia and Fp7 Project Enlightenment, and held in collaboration with Antibodies Online.

The congress received submissions from 21 countries, in all continents. To evaluate each submission, a double-blind paper review was performed by the Program Committee, whose members are highly qualified researchers in the NEUROTECHNIX topic areas.

NEUROTECHNIX's program included panels and four invited talks delivered by internationally distinguished speakers, namely Kevin Warwick (University of Reading, United Kingdom), François Hug (University of Queensland, Australia), Aldo Faisal (Imperial College London, United Kingdom) and Alexandre Castro-Caldas (Universidade Católica Portuguesa, Portugal).

We would like to thank the authors, whose research and development efforts are recorded here for future generations.

Lisboa, Portugal — Ana Rita Londral
Lisboa, Portugal — Pedro Encarnação
Madrid, Spain — José Luis Pons Rovira

Contents

Contributors

Axel Blau Department of Neuroscience and Brain Technologies (NBT), Neurotechnologies (NTech), Fondazione Istituto Italiano di Tecnologia (IIT), Genoa, Italy

Fernando Brunetti Catholic University of Asunción, Asunción, Paraguay

Bioengineering Group, Spanish Research Council (CSIC), Madrid, Spain

Antonio J. del-Ama Biomechanics and Technical Aids Unit, National Hospital for Spinal Cord Injury, Toledo, Spain

David Feess Robotics Innovation Center, German Research Center for Artificial Intelligence (DFKI GmbH), Robert-Hooke-Str. 1, 28359 Bremen, Germany

Chair of Global Business, Faculty of Business Administration and Economics, University of Augsburg, Universitaetsstr. 16, 86159 Augsburg, Germany

Diego Galeano Catholic University of Asunción, Asunción, Paraguay

Ángel Gil-Agudo Biomechanics and Technical Aids Unit, National Hospital for Spinal Cord Injury, Toledo, Spain

Asiyeh Golabchi Department of Neuroscience and Brain Technologies (NBT), Neurotechnologies (NTech), Fondazione Istituto Italiano di Tecnologia (IIT), Genoa, Italy

Rouhollah Habibey Department of Neuroscience and Brain Technologies (NBT), Neurotechnologies (NTech), Fondazione Istituto Italiano di Tecnologia (IIT), Genoa, Italy

Hans-Jochen Heinze Department of Neurology, University Medical Center A.ö.R., Magdeburg, Germany

Leibniz Institute for Neurobiology, Magdeburg, Germany

German Center for Neurodegenerative Diseases (DZNE), Magdeburg, Germany

Georg Hettich Neurocenter, Neurological University Clinic, Freiburg, Germany

Hermann Hinrichs Department of Neurology, University Medical Center A.ö.R., Magdeburg, Germany

Leibniz Institute for Neurobiology, Magdeburg, Germany

German Center for Neurodegenerative Diseases (DZNE), Magdeburg, Germany

Matthias Kennel Fraunhofer Institute for Factory Operation and Automation IFF, Magdeburg, Germany

Rudolf Kruse Department of Knowledge and Language Processing, Otto-von-Guericke University, Magdeburg, Germany

Vittorio Lippi Neurocenter, Neurological University Clinic, Freiburg, Germany

Thomas Mergner Neurocenter, Neurological University Clinic, Freiburg, Germany

Juan C. Moreno Bioengineering Group, Spanish Research Council (CSIC), Madrid, Spain

Stefano Piazza Bioengineering Group, Spanish Research Council (CSIC), Madrid, Spain

José Luis Pons Rovira Neural Rehabilitation Group, Cajal Institute, Spanish Research Council (CSIC), Madrid, Spain

Christoph Reichert Department of Neurology, University Medical Center A.ö.R., Magdeburg, Germany

Department of Knowledge and Language Processing, Otto-von-Guericke University, Magdeburg, Germany

Jochem W. Rieger Department of Applied Neurocognitive Psychology, Carl-von-Ossietzky University, Oldenburg, Germany

Ulrich Schmucker Fraunhofer Institute for Factory Operation and Automation IFF, Magdeburg, Germany

Anett Seeland Robotics Innovation Center, German Research Center for Artificial Intelligence (DFKI GmbH), Robert-Hooke-Str. 1, 28359 Bremen, Germany

Sirko Straube Robotics Group, Faculty of Mathematics and Computer Science, University of Bremen, Robert-Hooke-Str. 1, 28359 Bremen, Germany

Robotics Innovation Center, German Research Center for Artificial Intelligence (DFKI GmbH), Robert-Hooke-Str. 1, 28359 Bremen, Germany

Diego Torricelli Bioengineering Group, Spanish Research Council (CSIC), Madrid, Spain

Kevin Warwick School of Systems Engineering, University of Reading, Reading, UK

Posturography Platform and Balance Control Training and Research System Based on FES and Muscle Synergies

Diego Galeano, Fernando Brunetti, Diego Torricelli, Stefano Piazza, and José Luis Pons Rovira

Abstract Balance control plays a key role in neuromotor rehabilitation after stroke or spinal cord injuries. Computerized Dynamic Posturography (CDP) is a classic tool to assess the status of balance control and to identify potential disorders. In this paper, we present the development of a low cost system and tool for the assessment and training of balance based on static posturography and functional electrical stimulation (FES). The assessment features are built upon a classic a CDP basis, while for training routines, the system uses bioinspired FES patterns and algorithms based on muscle synergies. This system includes low cost technology like the Wii Fit Balance Board and the Kinect. The work described is this paper includes the implementation of the system and first results as a CDP tool.

Keywords Posturography • FES • Muscle synergies • Kinect • Wii balance board

1 Introduction

There are several diseases that can affect human balance and posture control. Such diversity requires the participation of different specialists in the diagnosis and treatment process like neurologists, otolaryngologists and ophthalmologists among others. Posturography is defined as an objective assessment technique of postural control based. In this way, the monitoring of the center of pressure of the

D. Galeano (✉)
Catholic University of Asunción, Asunción, Paraguay
e-mail: diego.galeano@uca.edu.py

F. Brunetti
Catholic University of Asunción, Asunción, Paraguay

Bioengineering Group, Spanish Research Council (CSIC), Madrid, Spain

D. Torricelli • S. Piazza
Bioengineering Group, Spanish Research Council (CSIC), Madrid, Spain

J.L.P. Rovira
Neural Rehabilitation Group, Cajal Institute, Spanish Research Council (CSIC), Madrid, Spain

A.R. Londral et al. (eds.), *Neurotechnology, Electronics, and Informatics*,
Springer Series in Computational Neuroscience 13, DOI 10.1007/978-3-319-15997-3_1

person has proven to be an effective tool complementary to clinical diagnosis in order to quantify this neuromotor disorder. This technique also can be used as a complementary tool to help clinicians with the diagnosis of vertigo.

Posturography evaluates each of the sensory systems (visual, somatosensory and vestibular) involved in the complex balance system. Its purpose is to isolate the contribution of each of these systems to evaluate the status of each one separately. It also assesses movement strategies for maintaining balance, and examines the stability limits of the person and the ability to control voluntary movement.

Balance control is an important functional component of human gait. After spinal cord injury (SCI) or stroke, balance control is one of the first rehabilitation objectives towards the restoration of functional gait. In this scenario, posturography plays a key role to evaluate the progress of the affected subject. Classic therapies of posture control rehabilitation include exercises to improve stability limits or guided movements to reinforce control efforts of patient.

Over the last years muscle synergies have been described for several composed movements like those exerted during normal postural control. Muscle synergies can be understood as functional muscle co-activation patterns [1]. This theory proposes the existence of simplified mechanisms and signals that can control several muscles at the same time. The most interesting aspect of this theory is the consistency of these synergies among subjects, and its stability intra subject. The use of this knowledge for rehabilitation is still a research goal, as well as the assessment of muscle synergies in functional tasks after stroke or SCI [2].

The use of Functional Electrical Stimulation (FES) to interact with muscle synergies during the rehabilitation of balance is a novel approach proposed by Piazza et al. in 2009 [3]. This paper presents a low cost system that enables the implementation of this novel rehabilitation paradigm. It is a posturography tool to help with the assessment of postural control and its rehabilitation. The main contribution of the work lies in its simplicity and its potential use in rehabilitation. It is an exploratory device to study new rehabilitation approaches of balance control while monitoring the status of human balance and postural control system. The presented tool enables the evaluation of the effectiveness of current treatments and the design of new ones. The paper presents technical details of the system and preliminary results.

Further stages of this work include the validation of the designed posturography system comparing to similar ones like the NedSVE/IBV® [4] of the Institute of Biomechanics of Valencia, or the SMART Balance Master of Neurocom®. After this validation, the design of new therapies based on FES and muscle synergies will be possible and its evaluation in clinical environment.

2 Assessment Methodology and Postural Control Rehabilitation

In this section, balance assessment methods used in posturography are reviewed, as well as the tests designed for this purpose. Finally existing proposals for rehabilitation based on synergies are described.

2.1 The Computerized Dynamic Posturography (CDP)

Computerized Dynamic Posturography (CDP) was designed and developed by Nashner. It was clinically studied in collaboration with Black [17] and Wall and marketed in 1986 as Equitest by Neurocom Inc. [5].

The CDP is a technique that analyzes subject's postural control in static standing and his/her response to destabilizing conditions. It is based on the idea that the center of gravity (COG) oscillations reflect postural instability. Generally CDPs are based on dynamometric platforms. These systems analyze the postural oscillations by recording the vertical projection of gravity force, known as Center of Pressure (COP). More frequent tests made with similar platforms are:

- **Sensory System or Romberg's Test.** It is aimed at determining the ability of the patient to integrate the three systems responsible for assessing standing balance and body sway while different sensory conditions are applied. The results of this test are compared with results of normal subjects. It is performed with eyes open and eyes closed, with and without foam on which the subject stands. It can also be performed with the patient's head retroflexed, causing distortion in neck proprioceptors. These tests can also be used to evaluate proprioceptive information by making patients to rely in vestibular information to maintain the balance [6].
- **Stability Limit Test.** It assess the capacity of the subject to bring his COP to the border of his/her stability limit. Basically, this test is used to assess the maximum distance the patient can move his/her COP without changing the base of support, i.e. without moving his/her feet. During the test, the subject can see his/her COP representation on a computer screen in front of him, and he/she should move it toward the stability limits without moving its base of support. The test includes up to eight sequential different targets located around theoretical stability limits (according to previous measurements with healthy subjects).
- **Rhythmic and Directional Tests.** These tests try to assess subject's ability to perform rhythmic movements around of its center of gravity (COG). The subject is a asked to follow with his/her COP moving targets whose speed and range are configurable. The target is moved to a percentage of the stability limit previously calculated for the subject. This test is usually performed in the anteroposterior and mediolateral directions.

2.2 Hybrid Approaches in Assisted Neuromotor Rehabilitation

Hybrid exoskeletons have emerged as a way to improve motor assistance using the benefits of FES and robotic exoskeletons. They overcome individual limitations of the methods used separately. The FES uses natural muscles as actuators to generate a movement, which provides not only functional benefits but also physiological. Robotic exoskeletons artificial actuators are used to move the lims that can not be fully or partially controlled voluntarily.

Generally, people affected by stroke and SCI have healthy muscles. The hybrid approach proposes the use of their own muscles to complement the action of the robotic exoskeleton. Muscles are activated coordinately with the exoskeleton controller by means of an electrical stimulation system [7]. This approach results in a reduction of energy demand and allows the exoskeleton to use lighter and less powerful actuators. Moreover, this solution is considered more natural and help to preserve existing biological structures. Main problem when using FES is that it can produce muscle fatigue after long periods of stimulation. This problem limits the time of use. This is not a problem when using exoskeletons, which can be used for a longer time.

Balance control is an important not only when rehabilitating after stroke or SCI but also when using exoskeletons. Hyper is a Spanish research project aimed at developing new neurorobotics and neuroprosthetics therapies for people affected by stroke or SCI. First clinical interventions include the rehabilitation of balance and postural control. The use of hybrid approaches is well considered by clinicians but they way they are used in this rehabilitation process and it effectiveness is not clear yet for the scientific community.

The control of the assistive device is also not clear in terms of compensation actions and movement routines. The most common approach over the last years was the so called “assist-as-needed” (AAN) paradigm [8]. Following this paradigm, the interaction between the assistive device and the natural involved mechanisms in the considered task is given in terms of the final results, and not considering the underlying status of biological control mechanisms. In this way, Hyper encourages the study and development of new therapies to support classic ones. These novel treatments are mainly driven by bioinspired mechanisms for better and deeper interaction between the assistive device and remaining neuromotor control structures, in order to reinforce and rehabilitate them in a more natural way.

2.3 Muscle Synergies

The study of human control system is a open research field where there are still many questions to answer. One of them is how is coded the information to control the large number of degrees of freedom of human movements. More specifically, this problem states that to generate a specific motor task, there are multiple combinations

of muscle activations that can generate similar results. Muscle synergies theory is a proposed answer to this question. The central nervous system can solve the complex task by choosing a specific set of muscle activations through a combination of a small set of neural patterns, called *synergy* [1].

Each muscle receives as input a modulating signal from higher neural centers, and outputs a weighted activation signal to activate a set of muscles. The activation of each muscle can be seen is a weighted sum of all synergies commands connected to it [9]. Then, muscle synergies can translate small sets of variables coming from the central nervous system into higher dimensional signals. They are strictly correlated to the functional performance and their modulation are related with user workspace. The most interesting characteristic of muscle synergies is that they are consistent inter healthy subjects [1, 3].

Mathematically, as indicated in [9], muscle synergies are explained by the following equation that describes the activation of a single muscle m,

$$m(t) = \sum_{i}^{K} c_i(t) w_i, \tag{1}$$

where m is the activation of the muscle function of time, c is the neutral command i-th synergy function of time, w is the constant weight of the i-th synergy referred to the m-muscle and K is the number of synergies.

The use of muscle synergies knowledge to rehabilitate postural control is still not clear. However, their role in functional movements and their importance have being already reported [10, 11]. This encourages Hyper scientific team to take them into account to promote the development of more efficient rehabilitation therapies by closely interacting with involved muscle synergies in balance control. In this way, FES can be used to develop and interact with synergies and muscle activation patterns.

3 Proposed System

In this section we describe the low-cost platform developed to perform static posturography tests and explore new therapies based of FES and muscle synergies. Balance control assessment platforms are usually not open and they are commercially available only as a posturography tool. Thus, a novel low cost and open posturography platform was developed to use it in this novel scenario. The main objective of this platform is to support the development of novel balance control rehabilitation therapies in the framework of the Spanish Hyper project.

Figure 1 shows the outline of the developed platform and a functional diagram of the different components that are further described in next sections. The platform is based on a centralized non real-time architecture, which includes several components: the Posturography Controller, the Neuroprosthetic Controller, a Wii Fit Balance Board, a Kinect camera and the TEREFES electrostimulation system [12].

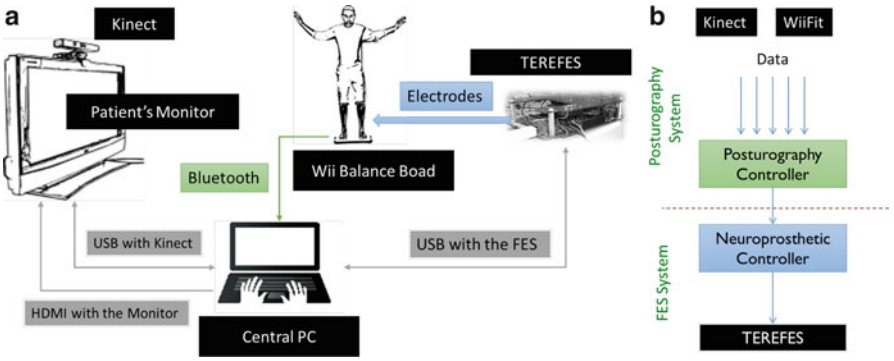

Fig. 1 (**a**) Proposed platform architectural and (**b**) the functional description diagram including the different components: the posturography system (balance control assessment) and the FES system (balance control training and rehabilitation)

3.1 Wii Fit Balance Board

Wii Fit balance board is an input device included in the Wii Fit from Nintendo®. It is a wireless device that uses Bluetooth technology to communicate with the Wii console. It is equipped with four resistive pressure sensors located in each corner of the table. In effect, it measures the displacement of the center of pressure and the weight of the user. It also gives an indication of the battery status.

Over the last years, the Wii Fit Balance Board have been used by the scientific community, specially as computer interface for disabled [13]. This device has two attractive features: it is wireless and low-cost. In our project, the Board will be used to measure the COP.

Data from Wii Fit Balance Board is accessed through a Microsoft Visual Studio C# application, using a library called WiimoteLib available at www.wiimotelib.codeplex.com. Visual C# was chosen because it is also compatible with the *Kinect* and its *Windows Software Development Kit* (SDK). Thus, the Wii Fit is connected as a HID interface device. Provided services by the Board are detected using the Service Discovery Protocol (SDP) of Bluetooth.

An important aspect to consider is the sampling frequency at which the Wii Fit sends the data to the PC, or more specifically, how often the data arrives, considering the nature of wireless transmission and the operating system behavior. To answer this question, we measured the time interval between samples using methods and public properties of the Microsoft Visual Studio C# class `System.Diagnostics.Stopwatch`. The program is executed in a almost dedicated HP Pavilion g6-1b70us Notebook (Intel Core i3 CPU M 370 @ 2.4 GHz, 4 GB of RAM) running 64-bit Windows 8. According to the obtained results, the average sampling frequency is 100 samples/s.

The aim of this analysis it to know how deterministic is the access to the data of the Board in terms of time. In other words, we want to know the probability that the

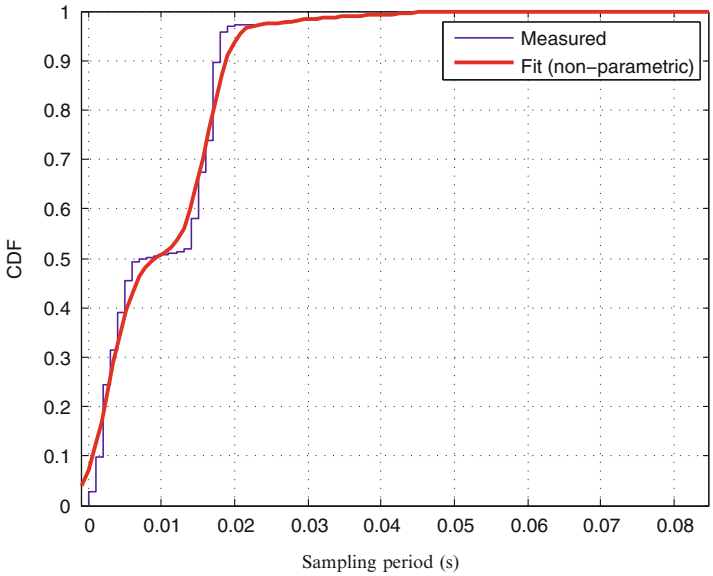

Fig. 2 Cumulative distribution function as a function of the sampling period (s)

sampling period of the Wii Fit is less than or equal to any given time. Cumulative distribution function for the Wii Fit data is depicted in Fig. 2. For example, the probability that the sampling period remains less than or equal to 0.02 s is 94.02 %.

3.2 Microsoft Kinect

The Kinect device is a natural user interface, which allows users to interact with games without physical contact. It was developed by PrimeSense Company. The user becomes the controller itself, having to rely on movements, natural gestures and voice commands to control game elements.

Kinect is equipped with an RGB-D camera that acquires images of 640 × 480 at 30 fps. It has a visual field range from 1.2 to 3.5 m, but can be reduced by optical coupling, as Niko Zoom Lenses®. Furthermore, its viewing angle is 57° horizontally, and 43° vertically. The vertical visual field can be expanded 27° with its servomotor. It is also equipped with an array of four microphones, each with a recording resolution of 16 bits sampled at 16 kHz. It also contains a stack of signal processing hardware that is able to handle all the data generated by cameras, infrared light, and microphones. By combining the output of these sensors, a program can track and recognize objects in front of it, determine the direction of the sound signals, and isolate them from the background noise.

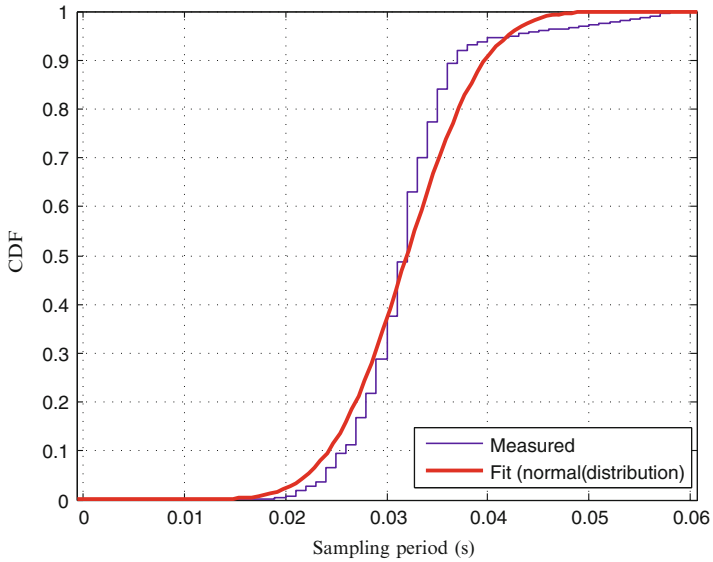

Fig. 3 Cumulative distribution function of the sampling period Kinect

The role of the Kinect in the platform is to enrich the visual feedback provided to the patient. Common posturography platforms are limited to provide users information about the center of pressure but the user does not know precisely his/her position and how good it is for the intended task. In this way, the Kinect provides kinematic information of full body segments, thus providing more complete information to users as well to the Neuroprosthetic Controller enabling better actuation commands.

Both, the Wii Fit as the Kinect, help to give visual feedback to the evaluated subject, and the information generated can be used by the Neuroprosthetic Controller to generate more precise and adequate stimulation patterns. A similar analysis done with the Wii Fit Board, was carried out with Kinect to evaluate the jitter effect when acquiring the frames.

The cumulative distribution function is shown in Fig. 3. For example, the probability that the sampling frequency is maintained below 35 fps is 75 %, approximately.

3.3 Posturography Controller

The Posturography Controller is implemented in a personal computer running Windows 8 operating system. The developed software includes traditional posturography tools and tests like Romberg's test, test of the stability limits and the rhythmic directional test.

The software was developed for easy use by medical personnel. It includes a database in which data of each patient is stored, allowing the physician to evaluate subject progress after several sessions. It also helps to diagnose potential diseases and program rehabilitation exercise routines for each evaluated subject. The application is also able to generate Matlab scripts containing the center of pressure points recorded during each rehabilitation session. In this way, the therapists can analyze data recorded in previous sessions.

The Posturography Controller receives all the data from the Kinect camera and the Wii Fit Balance Board. It fuses and displays the acquired data showing information like the center of pressure, the rigid body kinematic chain of the studied/analyzed subject, and information about current routines and tests. This controller and the Neuroprosthetic Controller are implemented in the same computer.

In next sections details on the parameters used to quantify the results of each test will be described [14].

– **Romberg's Test.** The subject is positioned on the Wii Fit Balance Board in an upright position with arms straight and close to the body trying not to move the head in neutral position facing forward, bare feet at an angle Opening of 30°. In this position is assessed for T seconds (configurable by the doctor) their ability to maintain balance in the following conditions:

  - Eyes Open (REO) and Eyes Closed (REC).
  - Foam on Wii Fit with Eyes Open (RGA) and Eyes Closed (RGC).

  The parameters evaluated in each test are:

  - *Shift angle (degrees)*. The angle of the vector extending from the initial point to the subject portion to the end point of the trajectory.
  - *Swept area (mm^2)*. It estimates the area swept by the COP by mean of an ellipse whose axes correspond to the maximum mediolateral and anteroposterior displacement.
  - *Average speed (cm/s)*. It estimates the average speed, which is the ratio between the displacement and time, T, that lasts the test.
  - *Maximum mediolateral and anteroposterior displacements (mm)*. These parameters represent the longest displacement in the mediolateral and anteroposterior axes during the exercise.

  Figure 4 shows a screenshot during the execution of the application designed in this project. Specifically, this screenshot corresponds to a REO Test. The figure shows two visual feedbacks. The first one is the position of the center of pressure on the Wii Fit Balance Board, and the second, provided by Kinect, is the RGB image and a trace of its skeleton. The screen provides information about subject's skeleton (skeleton blue) and a given reference (red skeleton). The reference indicates correct estimated position during the tests.

  Some parameters are provided online by the application. For example, regarding the Kinect, it monitors the status of the tracking task, which can be *Tracking* (OK) or *not skeleton* (Subject not detected). Another parameter is the

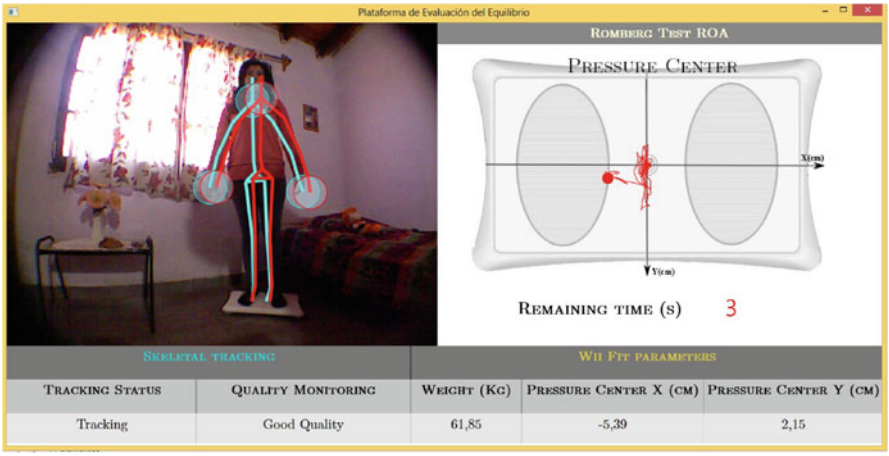

Fig. 4 Screenshot during the execution of REO Test. On the *right*, it is shown the center of pressure on the Wii Fit while on the *left* the subject with his/her skeleton (*blue lines*) and the given reference (*red lines*)

quality of the skeleton. This parameter indicates if the Kinect is showing the complete skeleton of the subject (*Good Quality*). This will help the therapist to point the camera in the correct position. Regarding the Wii Fit Balance Board, the parameters observed are subject's weight and the coordinates of the COP.

– **Stability Limit Test.** This test evaluates the following parameters:

  - *LE max (mm)*. It is the maximum value reached by the COP in the corresponding direction (8 targets separated of 45° and whose radial distance from the origin is configurable).
  - *Stability zone (cm)*. It is approximately the mean distance at which the patient is 90 % of time. It is calculated for each direction.

  Figure 5 shows a screenshot during the execution of limit test. The displacement of the COP on the Wii Fit for the Limit Test is depicted on the right side. The red circle represents the current target to which the subject should direct his/her COP, while the green ones represent those already targeted. Traces of COPs in these directions have been deleted to not disturb the patient while reaching current target.

– **Rhythmic and Directional Test.** In this test, the patient is asked to follow the movements of a moving target (configurable frequency) in mediolateral (ML) and anteroposterior (AT) directions. The maximum excursion limit is calculated based on the parameters of normal stability limits (previously recorded with healthy subjects).

  The following parameters are evaluated for each direction.

  - *Reaction time (s)*. It is defined as the time that the subject takes to bring his/her center of gravity closer than two centimeters from the reference target.

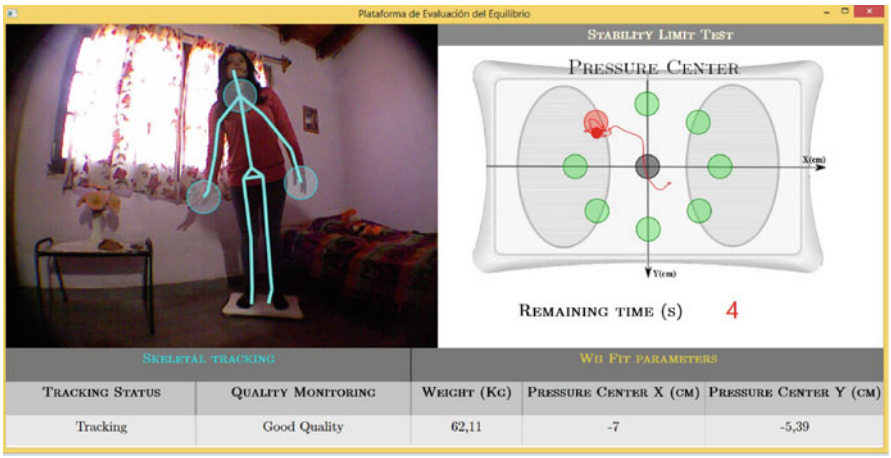

Fig. 5 Screenshot during the execution of the limit test. On the *right side* of the screen, the COP on the Wii Fit is shown in real time. On the *left side* is shown the patient with his/her stickman representation (*blue lines*)

- *Tracking capability (%)*. It quantifies subject's ability to follow the movement of the target in ML or AT directions. This parameter is calculated as the mean of error ($DesiredCOP - MeasuredCOP$), after the reaction time. If the error is lower than 2 cm (configurable), in other words the COP is inside the target circle, it is considered as zero for this sample.
- *Directional control (%)*. It quantifies the subject's ability to remain in the expected direction of the test. For example, if the target moves in the axis ML, the index is evaluated considering the AT axis error using the same process for calculating the tracking capability.

3.4 Neuroprosthetic Controller

The Neuroprosthetic Controller is responsible for the generation of muscle activation patterns and control of the actuation system: the TEREFES electrostimulator. It receives from the Posturography Controller all the kinematic data of the subject (acquired with the Kinect) and the coordinates of the center of pressure (COP). A driver decodes and converts the information into muscle activation patterns and specific TEREFES commands according to previously programmed synergies sets, theory and rehabilitation parameters. Full details of the proposed synergistic controller can be found in [15]. The functional stimulator TEREFES must act synchronously according with the exerted movements. Since Windows is not a real time operating system, a best effort approach is used in the Neuroprosthetic Controller. The TEREFES (real time system) is used to monitor possible delays in the Neuroprosthetic Controller. In next stages, system timing should be further analyzed.

3.5 TEREFES

The TEREFES was proposed in the framework of the TERERE and Hyper projects [12]. The TEREFES electrostimulator provides up to 32 stimulation channels driven by controllable and stable and close loop current sources. In addition, the system is portable and flexible. This functional stimulator is powered by 4 AA batteries and includes a USB communication interface that allows its online configuration through an external software. Monophasic and biphasic stimulation signals can be obtained in its 32 available channels. These channels are divided in two independent groups of 16 channels each, that can be sequentially activated.

4 Preliminary Results

In this section preliminary results of posturography software are presented. Described results were obtained with six healthy people, four men and two women. The purpose of this functional validation is to technically verify the platform and to compare result between different subjects. Unfortunately, at this stage of the work, the system could not be tested with previously diagnosed pathological subjects, and the results could not be compared with those obtained with other commercial platforms like Neurocom.

The procedures for the tests were explained in previous sections. REO and REC tests were conducted, as well as Stability Limit and Rhythmic tests. All of them were realized a couple of times in order to make sure that the subjects understand the test but without producing fatigue or previous learning/training [14]. The sampling frequency was 30 frames/s, enough to detect any COP displacement [16].

4.1 Romberg's Test

Each Romberg's test lasted 30 s. The results of the six subjects are shown in Table 1.

All proposed parameters were calculated and presented in Table 1. Results suggest a decrease of fine postural control in most subjects when they close their eyes. For both men and women, the displacement angle is usually in the second quadrant, and no significant differences are found among REO and REC tests. In fact, according to [14], this parameter does not change significantly under these test conditions.

Figure 6 shows the results of subject 4. Using similar data, proposed parameters were calculated for each subject.

Regarding the swept area, calculated according to [17], it does not reflect noticeable changes with the changing sensory conditions. Balaguer, in his work, [14], has suggested that the calculation by fitting a geometric figure may not be adequate to quantify this parameter.

Table 1 REO and REC test results

			Disp. angle (°)		S. area (cm^2)		A. speed (cm/s)		Disp. ML (cm)		Displ. AT (cm)	
Subject	Gender	Years	REO	REC	REO	REC	REO	REC	REO	REC	REO	REC
1	M	23	108.22	114.45	18.28	17.21	1.94	2.28	2.42	3.16	1.82	3.00
2	M	26	90.77	91.45	2.71	6.06	1.25	1.65	0.817	1.552	1.01	1.22
3	M	34	95.89	113.77	12.91	12.52	1.69	2.15	2.46	2.71	2.01	2.31
4	M	47	76.55	75.71	9.05	4.88	1.23	1.34	1.81	1.55	1.85	1.21
Average			92.86	98.84	10.74	10.17	1.53	1.86	1.88	2.23	1.67	1.94
5	F	19	122.49	112.1	4.94	5.85	1.53	1.95	2.06	2.05	1.06	2.45
6	F	18	106.79	103.85	8.99	7.45	1.34	1.65	2.15	2.03	1.13	2.32
Average			114.64	107.96	6.97	6.65	1.44	1.80	2.11	2.04	1.095	2.385

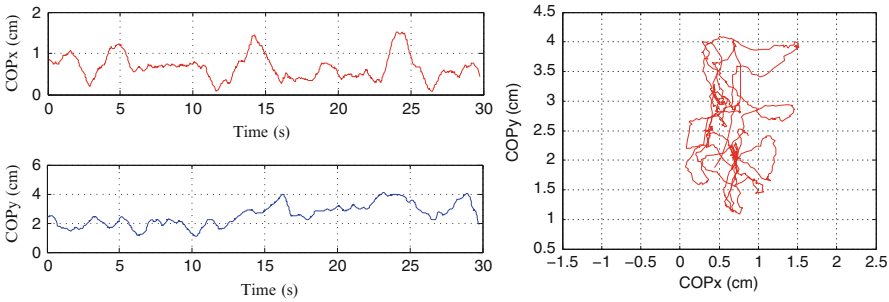

Fig. 6 Subject 4 (S4) REC Romberg's test plotted using Matlab. Parameters for S4 were calculated with these data

Table 2 Stability limit test results

	Average max. LE (cm)		Average stability zone (cm)	
	Gender			
Direction	Male	Female	Male	Female
Front	7.51	9.04	5.77	8.32
Front-right	9.68	9.695	8.05	8.73
Right	10.59	9.165	9.28	7.70
Rear-right	9.44	8.58	8.92	7.33
Rear	10.06	8.00	8.68	6.915
Rear-left	9.88	9.33	8.32	8.64
Left	11.01	10.05	9.00	8.35
Front-left	9.335	9.97	8.2675	8.55

Average values are shown. Similar data can be used to obtain normality patterns

Finally, the average speed of displacement, is found to increase without visual feedback. This same behavior is observed in the ML and AT displacement. Therefore, these parameters are used to differentiate visual system impact and potential dysfunction in balance control. Both men and women present larger variations in the ML direction, being even larger in men in these particular tests.

4.2 Stability Limit Test

The stability limit test lasted 10 s for each direction, and each target was located at a distance of 10 cm from the origin. The subject was asked to make his/her best effort to reach the targets.

Figure 7 shows the results of subject 1. Using similar data, proposed parameters were calculated for each subject (Table 2).

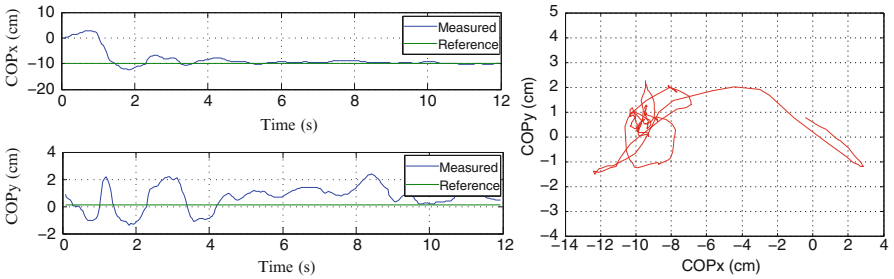

Fig. 7 Subject 1 (S1) limit test in left direction results plotted using Matlab. Parameters for S1 are calculated with these data

Table 3 Rhythmic control test results

			Reaction time (s)		Tracking capability (%)		Directional control (%)	
Subject	Gender	Years	ML	AT	ML	AT	ML	AT
1	M	23	0.037	0.50	81.86	85.7	81.7	99.9
2	M	26	0.119	0.039	80.55	70.44	90.17	99.05
3	M	34	0.12	1.059	87.7	63.8	78.22	99.83
4	M	47	0.198	1.046	79.6	57.8	77.51	99.92
Average			0.1185	0.66025	82.43	69.43	81.9	99.675
5	F	19	0.40	0.035	66.5	70.23	79.7	98.5
6	F	18	0.42	0.21	71.5	55.26	88.53	96.94
Average			0.4125	0.1225	69.0	62.74	84.11	97.72

According to these tests, areas of stability in both men and women vary with direction. In general terms, there are no significant differences. These results agree with [18]. However, a larger population is needed to obtain robust conclusions. Balaguer found that subject owns subjective perception (Previous Q&A about disability condition of the subject) of his/her skill or disabilities does not influence the stability limits [14].

4.3 Rhythmic and Directional Control Test

For the rhythmic tests, windows of 10 cm (configurable) long were defined directionally, first in the ML direction and then in the AT one. The subject was asked to follow a moving target traveling at a frequency of 0.25 Hz. Each test lasted 20 s. The results are shown in Table 3 for each patient.

Figure 8 shows the results of subject 5 (S5). Similar results were used to calculate all parameters for each subject.

According to these results, the reaction time increases with age. In addition, there is a shorter reaction time in women. In men, the reaction time is better in the ML

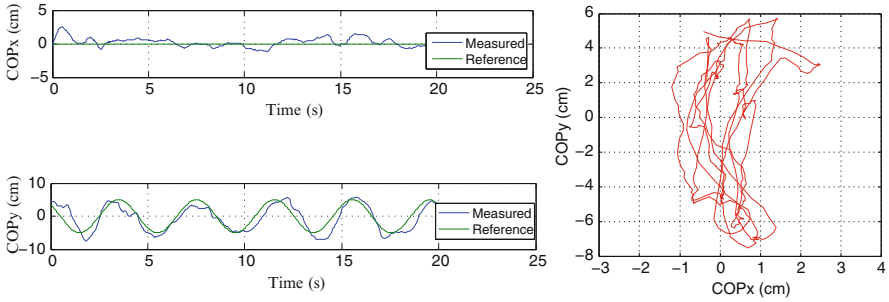

Fig. 8 Subject 5 (S5) rhythmic test results in the AT direction plotted using Matlab. Parameters for S5 are calculated with these data

direction with respect to the AT direction. Although this work has not made a study of subjects with specific pathologies [14] found that vestibular disorders can affect rhythmic and directional control in disagreement with the findings of Cortés [18].

5 Discussions

Posturography helps to assess the influence of any vestibular dysfunction in postural and balance control. However, a pathology that affects the balance in one patient, in other word the vestibular-spinal reflex, not necessarily will have the same effect it in another subject. In this case, tools like the one described in this work are not effective to help the diagnosis of the impairment.

Regarding the tool presented in this paper, it i not very clear in the literature the way how different assessment parameters are calculated. This lack of information makes more difficult to compare results. However, overall conclusions and trends obtained with this tool are similar to those reported in the literature and obtained with other platforms.

Nowadays, there is still a discrepancy between scientists regarding the results of each parameter and associated information. According to [14], this discrepancy exits because it is difficult to find clear relationships between functional assessment of balance and patient-perceived disability. Tests may be influenced by many factors like social, professional, technical, psychological, affective, and cognitive ones.

The current drawback of classical static posturography is limited only to study the subject during standing position, so it does not provide information on the dynamic aspects of postural control. To solve this shortcoming, we have followed the line proposed by García [14] and set dynamic tests, such as the rhythmic test.

Regarding the Neuroprosthetic Controller and the potential use of the system as a tool for training the balance control, it is ready to be used. However, specific scenarios and protocols should be defined to validate technically the tool in a better way.

6 Conclusions and Future Work

Postural rehabilitation boosts patient confidence and contribute to their self-improvement. In addition, knowledge of the particular deficit in postural control helps clinician and patient to develop prevention plans to avoid falls, and as mentioned before, it is the first step towards the rehabilitation of more complex processes like gait.

Current research projects in neuromotor rehabilitation like Hyper, are devoted to develop novel bioinspired rehabilitation treatments. The use of hybrid solutions including neurorobotics and neuroprosthetics devices has been shown as an efficient approach. However, the use and development of modern rehabilitation therapies based on novel knowledge need the support of non existing research tools.

We have seen how to make a low cost posturography system. It is based on a Wii Fit Balance Board, the Microsoft Kinect and the TEREFES electrostimulator. This tool can serve as a low cost balance control assessment tool and will allow the implementation of novel therapies that could improve current ones for the rehabilitation of balance control.

Future work includes the evaluation of the tool and developed system in clinical environments. After this validation, the final integration of the Neuroprosthetic Controller and the implementation of therapies based on muscle synergies will be done.

References

1. D'Avella A, Bizzi E. Shared and specific muscle synergies in natural motor behaviors. Proc Natl Acad Sci USA. 2005;102:3076–81.
2. Torricelli D, Aleixandre M, Alguacil IM, Cano R, Molina F, Carratalá M, Piazza S, Pons JL. Modular control of mediolateral postural sway. In: Proceedings of 34th annual international conference of the engineering in medicine and biology society (EMBC'12); 2012.
3. Piazza S, Torricelli D, Brunetti F, del-Ama AJ, Gil-Agudo A, Pons JL. A novel FES control paradigm based on muscle synergies for postural rehabilitation therapy with hybrid exoskeletons. In: Proceedings of 34th annual international conference of the engineering in medicine and biology society (EMBC'12); 2012.
4. Baydal J, Castelli A, Garrido J, Bermejo I, Broseta J, Amparo M, Perez J, Moya M. NedSVE/IBV v.5 a new system for postural control assessment in patients with visual conflict. Revista de Biomecánica (54). Valencia: Instituto de Biomecánica de Valencia; 2010.
5. Faraldo A. Registro postural en personas sanas: evaluación del equilibrio mediante el estudio comparativo entre la posturografía dinámica computerizada y el sistema sway star. Doctoral thesis, Universidad de Santiago de Compostela, Spain; 2009.
6. Khasnis A, Gokula R. Romberg's test. J Postgrad Med. 2003;2:169–72.
7. Del-Ama AJ, Koutsou AD, Moreno JC, Pons JL. Review of hybrid exoskeletons to restore gait following spinal cord injury. J Rehab Res Dev. 2012;49:497–514.
8. Cai LL, Fong AJ, Yongqiang L, Burdick J, Edgerton VR. Assist-as-needed training paradigms for robotic rehabilitation of spinal cord injuries. In: Proceedings of the 2006 IEEE international conference on robotics and automation (ICRA'06); 2006.

9. Torricelli D, Moreno JC, Pons JL. A new paradigm for neurorehabilitation based on muscle synergies. In: Proceedings of 34th annual international conference of the engineering in medicine and biology society (EMBC'12); 2011.
10. D'Avella A, Portone A, Fernandez L, Lacquaniti F. Control of fast-reaching movements by muscle synergy combinations. J Neurosci. 2006;26:7791–810.
11. Piazza S. Muscle synergies in postural sway movements: neurophysiological evidences and rehabilitation potentials. Master's thesis, University Carlos III of Madrid, Spain; 2013.
12. Brunetti F, Garay A, Moreno JC, Pons JL. Enhancing functional electrical stimulation for emerging rehabilitation robotics in the framework of hyper and project. In: 2011 IEEE international conference on rehabilitation robotics rehab week Zurich, ETH Zurich Science; 2011.
13. Martin A., Study and development of man-machine interface based on wireless sensor, Master Thesis, Escuela Técnica Superior de Ingeniería, Universidad Pontificia de Comillas; Madrid, Spain 2008.
14. García RB. Valoración de un método de posturografía estática con pruebas dinámicas para evaluar funcionalmente pacientes vestibulares en edad laboral y su relación con el índice de discapacidad. Doctoral thesis, Universidad Politécnica de Valencia, Spain; 2012.
15. Denis W, Brunetti F, Piazza S, Torricelli D, Pons JL. Functional electrical stimulation controller based on muscle synergies. In: Proceedings of the first international conference on neurorehabiltiation, converging clinical and engineering research on neurorehabilitation; 2012.
16. Enbom H, Magnusson M, Pyykko I, Schalen L. Presentation of a posturographic test with loading of the proprioceptive system. Acta Otolaryngol Suppl. 1988;455:58–61.
17. Black FO, Shupert CL, Peterka RJ, Nashner LM. Effects of unilateral loss of vestibular function on the vestíbulo-ocular reflex and postural control. Ann Otol Rhinol Laryngol. 1989;98:884–9.
18. Cortés O. Análisis clínico y posturográfico en ancianos con patología vestibular y su relación con las caídas. Doctoral thesis, Universidad Politécnica de Valencia, Spain; 2007.

A Pilot Study on the Feasibility of Hybrid Gait Training with Kinesis Overground Robot for Persons with Incomplete Spinal Cord Injury

Antonio J. del-Ama, Ángel Gil-Agudo, José Luis Pons Rovira, and Juan C. Moreno

Abstract Hybrid actuation and control have a considerable potential for walking rehabilitation of neurologically impaired people, but there is a need of novel hybrid control strategies that adequately manage the balance between functional electrical stimulation (FES) and robotic controllers. A case-study of a hybrid cooperative control strategy for overground gait training with a wearable robotic exoskeleton for persons with incomplete spinal cord injury (SCI) is presented. The feasibility of the control strategy to overcome muscular stimulation electromechanical delay, deterioration of muscle performance over time, and to balance muscular and robotic actuation cyclic overground walking is tested in one subject with incomplete spinal cord injury (L4, AIS grade D). The results show that the proposed hybrid cooperative control in Kinesis overground robot is able to autonomously compensate a bilateral pathologic walking pattern and the suitability of Kinesis hybrid gait training robot for conducting clinical experimentation.

Keywords Spinal cord injury • FES • Exoskeleton • Gait training

1 Introduction

Most therapies for rehabilitation of walking rely on the assumption that task-oriented practice promotes mechanisms of neural plasticity, muscle strength and learning of compensation strategies that increase walking ability of the person with SCI. Robotic technology holds a considerable potential to drive such interventions. Ambulatory robots, that have been developed mainly for functional compensation of walking, can offer a challenging and rich walking therapy. Furthermore, functional electrical stimulation can drive rehabilitation interventions of SCI providing several

A.J. del-Ama (✉) • Á. Gil-Agudo
Biomechanics and Technical Aids Unit, National Hospital for Spinal Cord Injury, Toledo, Spain
e-mail: ajdela@sescam.jccm.es

J.C. Moreno
Bioengineering Group, Spanish National Research Council, Madrid, Spain

J.L.P. Rovira
Neural Rehabilitation Group, Cajal Institute, Spanish Research Council (CSIC), Madrid, Spain

A.R. Londral et al. (eds.), *Neurotechnology, Electronics, and Informatics*,
Springer Series in Computational Neuroscience 13, DOI 10.1007/978-3-319-15997-3_2

physiological and psychological benefits to the user through artificial activation of paralyzed muscles. On the other hand, robotic exoskeletons can be used to manage the unavoidable loss of performance of FES-driven muscles. Hybrid exoskeletons are then regarded as a promising approach that blends complementary robotic and neuroprosthetic technologies. The overview of the state of the art on hybrid gait systems has demonstrated that such redundant actuated solutions can produce feasible systems for accurate control of joint movement [1]. Also, it has shown that diverse muscle fatigue management strategies could be applied for an effective closed-loop control of FES.

Under this hybrid scenario, the assist-as-needed control strategy has been proposed as a new redundant neuroprosthetic and robotic system that cooperates to optimize the outcome of the active control of the motion of the knee joint while providing assistance [2]. While various wearable exoskeletons were successful in achieving gait in subjects with incomplete spinal cord injury (SCI) [3–5] this has generally been proposed as a functional substitution. In this case study, we tested the feasibility of a novel hybrid gait training approach with an overground robot on a person with an incomplete SCI.

2 Material and Methods

2.1 Kinesis: Robotic Platform for Hybrid Therapy of Walking

Kinesis is a hybrid robotic device that has been developed for overground gait training in incomplete spinal cord injuries. Incomplete lesions were targeted because, first, prognosis of functional recovery of walking for these patients is that the they can walk short distances but depending on the wheelchair for community ambulation, therefore a successful hybrid walking therapy could provide benefits to this population. Second, motor-incomplete lesions have preservation of lower limb muscles innervation. This is a key feature when considering neuromuscular stimulation for therapy, because denervated muscles do not contract under artificially-delivered electric pulses. Among the different syndromes of incomplete spinal cord injury, target population is comprised by patients whose lesion is categorized as *Conus Medularis* [6], and those patients whose lesion met the functional characteristics of the *Conus Medularis*. These functional characteristics are intact upper body function and hip function preserved, while the knee and ankle muscles can vary from paralysis to healthy, depending on the specific characteristics of the injury.

The Kinesis system is a bilateral wearable knee-ankle-foot orthosis. Hip joint was not considered as the target population have preserved this function. Kinesis features active actuators at the knee hinges (Maxon DC flat motor, 90 W with Harmonic-Drive 100:1 gear) and a passive elastic actuator at the ankle. Force sensing resistors are employed for monitoring floor contact and custom force sensors are available to measure interaction torques. Kinesis has a PC-controlled stimulator (Rehastim,

Hasomed GmbH) which delivers biphasic current-controlled rectangular pulses. Rehastim can be pulse width and current controlled in real time.

The high-level control approach to achieve a cooperative behavior comprises four main components: (1) a knee joint robotic controller, (2) FES controller, (3) muscle fatigue estimator (MFE), and (4) a finite-state machine (FSM) that orchestrates the FES and joint controllers. Further details on the implementation of the high-level control can be found in [2, 7]. The cooperative behavior of Kinesis allows obtaining adequate and personalized stimulation patterns, estimating muscle fatigue and reducing robotic assistance during ambulatory walking. The ultimate goal is to give priority to the muscle-generated torque during gait training. A finite-state machine is employed to iteratively control the FES of knee muscles in a learning scheme for each leg while adapting torque field stiffness for a reference kinematic pattern. In this scheme, the resulting interaction torque (with added mass and inertia of the leg) is monitored and used towards convergence of stimulation parameters. The robot modulates its assistance by reducing joint stiffness, as shown in next section, ensuring the target flexion angle for effective swing of the leg. A muscle fatigue estimator is employed (based on the measurement of interaction torque) to trigger a fatigue compensation strategy (change stimulation firing rate). More details on the muscle fatigue monitoring and management strategy can be found in [8, 9]. A more detailed descriptions of the technique for hybrid cooperative control of Kinesis are discussed in [2, 7].

2.1.1 Robot Stiffness Modulation Strategy

The strategy to modulate the exoskeletal knee stiffness during cyclic walking is described in this section. The efficacy of the FES controller to generate the knee movement is inherently limited, due to the low efficiency of the force generated by the stimulated muscles and the electromechanical delay between the stimulus and the onset of joint movement. The goal of the hybrid control strategy was therefore to exploit the joint movement generated by the stimulation controller while supporting the movement through the joint controller. A controller was employed to provide compliant assistance to the knee, depending upon the parameter K_k, the stiffness of the force field applied around the trajectory.

Modulation of K_k was executed depending on the gait phase and the contribution of the FES to the knee trajectory. Thus, gait phase and muscle contribution were managed within a finite state machine (FSM), comprised of two FSMs operating in parallel: one FSM runs in the time domain (t-FSM) while the other operates in the cycle domain (c-FSM). The t-FSM detected the main walking states and the transitions among them. The c-FSM operated with discrete values, during each swing phase, that are related to performance of the stimulated muscle. Muscle fatigue results in a decrease of muscle performance thus increasing the interaction torque. This increase can be automatically compensated with the closed-loop FES controller reducing the interaction torque. This allows to uncouple the closed-loop control of stimulation from the muscle fatigue monitoring and management.

The t-FSM modulated the force field stiffness K_k and set the kinematic pattern, depending on the walking state. The compliant behavior of the exoskeleton was achieved by controlling knee trajectory through a first order torque field imposed around the joint trajectory. As a result, the joint torque imposed by the robot depended on the deviation of the knee trajectory from the kinematic pattern and the stiffness of the torque field K_k. The width of a virtual tunnel where the knee can actually move could be adjusted along time. During stance, a high stiffness torque field was imposed to provide support and avoid knee collapse. Conversely, the supportive actions of the exoskeleton must be reduced during the swing phase to allow for the contribution of stimulated muscles and passive dynamics. The former requirement was achieved by reducing the support of the robot through a wider virtual tunnel. At the end of each swing phase, prior to contacting the floor, the robot gradually increased its support to ensure full knee extension, through a progressive increment in the force field stiffness. However, this late stiffness for foot contact is insufficient for weight support and therefore, a quick transition to high stiffness required for stance was implemented.

2.2 Subject

A 43-year old male (75 kg and 1.77 m height) with a traumatic lesion at L4 (AIS [10] grade D) volunteered for participating in the experiment. He had preserved hip flexion ability, partial ability to generate voluntary knee extension and is in presence of mild spasticity. As consequence of the accident, the patient had a limited articular range of motion at both knees, which led to adaptation of the kinematic pattern of the left leg to meet these physical constraints (Table 1). The joint angle for the stance phase of the left leg was set at the maximum knee extension angle, and the kinematic pattern for the swing phase was consequently adapted. The subject provided written informed consent by signing a form that was approved by the Spinal Cord National Hospital Review Board.

2.3 Protocol

The patient participated in the hybrid gait training testing session (HGTT) to determine the feasibility of overground control of walking with Kinesis. Prior to the HGTT, the patient underwent a stimulation test and a training session in separate days. The stimulation test was employed to quantify the muscular response to the

Table 1 Articular range of knee joint

	Left leg	Right leg
Range of movement	20–100°	5–150°

Table 2 Stimulation test results: maximum force-time integral achieved (absolute and normalized by patient's leg weight)

Movement direction	Left leg	Right leg
Extension (N)	60 (134 %)	70 (156 %)
PA (mA)	40	48
Flexion (N)	10 (22 %)	25 (56 %)
PA (mA)	60	58

Stimulation PD was set to 450 μs, train frequency to 70 Hz, pulse train duration 14 s and duty cycle 43 %

muscle stimulation and also to get the patient used to the stimulation. Within this stimulation test, both flexor and extensor knee muscle groups of both legs were stimulated for 15 min. The results from the stimulation test are showed in Table 2. The only noticeable finding was a reduced performance of the left leg's flexor muscles.

After the stimulation test, a training session took place in which the subject carried out learning exercises with the Kinesis system. In this training session the basic walking technique was explained to the user (bend to the side to lift the heel prior to initiate a step and then pressing a manual button). Kinesis was adjusted to the patient anthropometry within this session. Total time walking in this training session did not exceed from 10 min. During HGTT kinesis hybrid-cooperative controller modulated both stimulation and robotic assistance during walking.

3 Results

The analysis of feasibility was performed at the biomechanical level. We assessed the actual knee joint kinematics and stiffness during overground hybrid control of gait. In Fig. 1, the kinematic pattern designed to meet patient's left knee angular limitation is showed (blue curves, light blue curves are actual knee angle). Looking at the right leg, high interaction forces towards flexion during stance were appreciated (Fig. 1c, d red curve, leg over exoskeleton). These flexor forces reflected on the kinematics, where the right knee is flexed during stance. In contrast, the interaction forces of the left leg during stance were lower, and the actual knee angle during stance remained close to the reference. Transition from stance to swing phase of the right leg resulted also on a transition of the interaction forces from flexor direction for stance, to markedly extensor direction for swing. Stimulation of flexor muscles for both legs exhibited in general a saturated pattern for the swing phase (black curves).

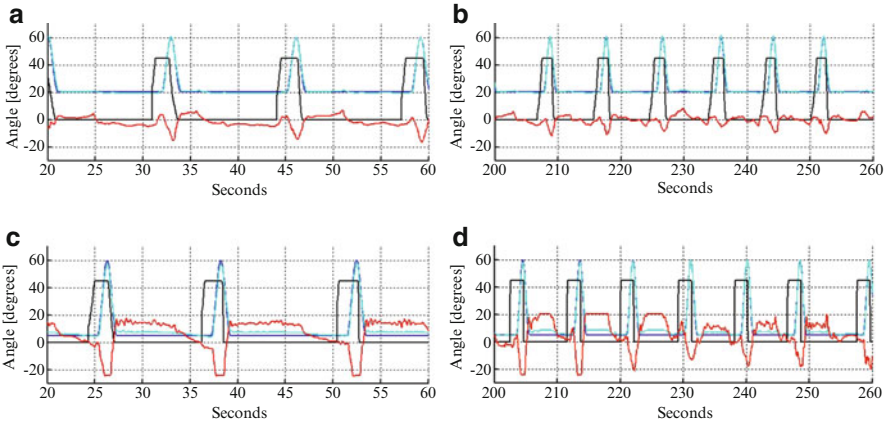

Fig. 1 Pattern (*blue curve*, deg) and actual (*light blue curve*, deg) knee kinematics, interaction torque (*red curve*, N·m/deg) and stimulation controller output (*black curve*, μs, only stimulation of flexor muscles is showed for representation purposes). (**a**) First steps of left leg; (**b**) last steps of left leg; (**c**) first steps of right leg; (**d**) last steps of right leg

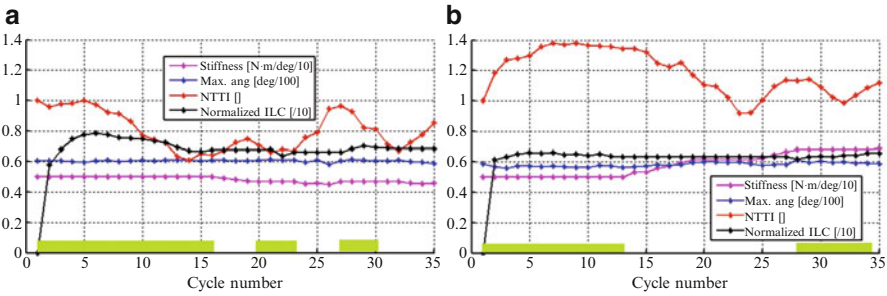

Fig. 2 Experiment results in cycle domain. Stiffness of the robotic knee joint (*magenta curve*, N·m/deg), maximum angle achieved during flexion (*blue curve*, deg) normalized torque-time integral (NTTI, *red curve*), and normalized stimulation controller output for knee flexor muscles (NILC, *black curve*) of both legs for the entire walking experiment. *Green boxes* shows *learning* state active. No box means *monitoring* state active. Controller stiffness, maximum angle and normalized stimulation curves are scaled for representation purposes. (**a**) Left leg; (**b**) right leg

Maximum flexion angle of the right leg for the first learning period was slightly lower than 60° (Fig. 1c,[1] blue and light blue curves). This was further compensated during the first monitoring period by an increase in the stiffness (Fig. 2b). It was also noticeable the difference in step cadence between the beginning and the end of the walking experiment, which indicates that the patient increased expertise and confidence on the use of Kinesis after a number of cycles (Fig. 1a–d respectively.)

[1]This is actually difficult to observe in the figures. During the first learning period, the maximum flexion angle was 58° in average.

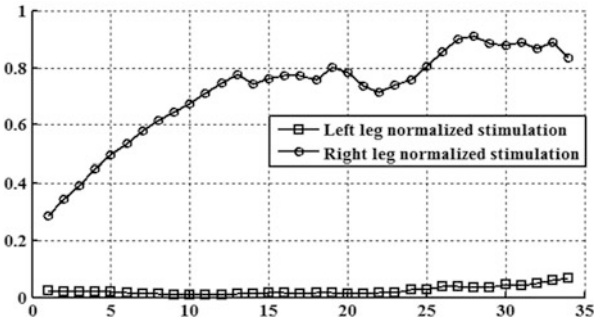

Fig. 3 Normalized quadriceps stimulation during stance phase of walking (both legs). X axis: number of steps

Figure 2a, b shows the operation of Kinesis within cycles, thus the c-FSM operation. The averaged interaction torque during the swing phase was obtained, and divided by the first averaged interaction torque. This procedure allowed for monitoring the cycle-to-cycle evolution of the physical interaction between the leg and the exoskeleton (NTTI, red curve in the figure). Furthermore, the stimulation controller output for knee flexor muscles was averaged for the entire swing phase and divided by a saturated stimulation for the entire swing phase. The value obtained reflect an scalar value that is representative of the stimulation intensity during the swing phase (NILC, black curve in the figure).

NILC for both legs achieved the 70 % of the maximum achievable stimulation intensity for the swing phase. After the first learning period of the right leg, a decrease on NTTI is observed along with an increase on the stiffness. In cycle 27 fatigue was detected and a new learning period took place (Fig. 2b). Regarding the left leg, a more moderated increase on stimulation intensity (Fig. 2, black curve) for the first learning period was observed, reaching similar stimulation intensity than for the right leg, corresponding with a decrease on NTTI. After the learning period, the stiffness was slightly reduced.

Figure 3 shows the averaged quadriceps stimulation intensity for the stance phases, for both legs, during the HGTT. These value was obtained similarly to the NILC procedure. It is noticeable the high stimulation intensity applied to the right leg, in response to the flexion posture exhibited by the patient during stance phases. Furthermore, as the experiment progressed and more steps were taken, the stimulation intensity progressively augmented until reaching a plateau (step 13), although after step 22, stimulation intensity increased across cycles.

4 Discussion

During and after the HGTT, no adverse effects were observed, and the patient reported neither uncomfortable nor excessive physical demand. He was able to learn the use of the system after 1 day of practice, although increases in the number of

steps were observed in the experiment, which could be related to gaining expertise in the use of Kinesis.

The specific functional deficit of the subject lead to a limitation on the maximum (left) knee extension, which caused the patient to exert compensating actions. These compensations were effectively counteracted by the hybrid gait control. The compensating actions differed for both side and stance and swing phases of gait. During stance, on average, the patient flexed the right knee in an attempt to compensate for the flexion angle of the left knee. The robotic actuation compensated the stimulation as needed: the displayed stiffness was sufficient to provide compliant but adequate support during stance phases. We also noticed that during pre-swing phases, the subject consistently changed from flexion to extension, probably as a response to the limited range of movement of the right knee.

The results from the case study presented here supports performing a more detailed clinical study in order to investigate the impact of the HGTT in the walking ability of an adequate sample of spinal cord injured patients.

5 Conclusion

The HGTT delivered by Kinesis was tolerated by the patient, completing the 6 min of walking test. Mutual adaptations were observed between the patient and Kinesis that were assessed through the analysis of the physical interaction. The hybrid cooperative control in Kinesis is able to compensate a bilateral pathologic walking pattern by autonomously increasing the stimulation of the flexor muscles and increasing the displayed stiffness of the robotic actuator.

Acknowledgements This work was supported by grant CSD2009-00067 CONSOLIDER INGENIO 2010. The authors thanks to all the participants that volunteered for the experiments, and the clinical staff from National Hospital for Spinal Cord injury.

References

1. del-Ama AJ, Koutsou AD, Moreno JC, de los Reyes-Guzmán A, Gil-Agudo A, Pons JL. Review of hybrid exoskeletons to restore gait following spinal cord injury. J Rehab Res Dev. 2012;49(4):497–514.
2. del-Ama AJ, Gil-Agudo Á, Pons JL, Moreno JC. Hybrid FES-Robot cooperative control of ambulatory gait rehabilitation exoskeleton. J Neuroeng Rehab. 2014;11:27. doi: 10.1186/1743-0003-11-27.
3. Dollar AM, Herr H. Active orthoses for the lower-limbs: challenges and state of the art. IEEE Int Conf Rehab Robot. 2007;1:968–77.
4. Dollar AM, Herr H. Lower extremity exoskeletons and active orthoses: challenges and state-of-the-art. IEEE Trans Robot. 2008;24(1):144–58.
5. Hesse S, Waldner A, Tomelleri C. Innovative gait robot for the repetitive practice of floor walking and stair climbing up and down in stroke patients. J Neuroeng Rehab. 2010;7:30.

6. Hayes K, Hsieh JTC, Wolfe D, Potter P, Delaney G. Classifying incomplete spinal cord injury syndromes: algorithms based on the international standards for neurological and functional classification of spinal cord injury patients. Arch Phys Med Rehab. 2000;81(5):644–52.
7. del-Ama AJ, Moreno JC, Gil-agudo Á, Pons JL. Hybrid FES-robot cooperative control of ambulatory gait rehabilitation exoskeleton for spinal cord injured users. In: 2012 international conference on neurorehabilitation (ICNR2012): converging clinical and engineering research on neurorehabilitation; 2012. p. 155–9.
del-Ama AJ, Gil-Agudo A, Pons JL, Moreno JC. Hybrid FES-robot cooperative control of ambulatory gait rehabilitation exoskeleton. J Neuroeng Rehabil. 2014;11:27. doi:10.1186/1743-0003-11-27.
8. del-Ama AJ, Koutsou AD, Bravo-Esteban E, Gómez-Soriano J, Gil-agudo Á, Pons JL, Moreno JC. A comparison of customized strategies to manage muscle fatigue in isometric artificially elicited muscle contractions for incomplete SCI subjects. J Autom Control. 2013;21(1):19–25.
9. del-Ama AJ, Moreno JC, Gil-Agudo A, De-los-Reyes A, Pons JL. Online assessment of human-robot interaction for hybrid control of walking. Sensors (Basel). 2012;12(1):215–25.
10. Maynard FM Jr, Bracken MB, Creasey G, Ditunno JF Jr, Donovan WH, Ducker TB, Garber SL, Marino RJ, Stover SL, Tator CH, Waters RL, Wilberger JE, Young W. International standards for neurological and functional classification of spinal cord injury. American Spinal Injury Association. Spinal Cord. 1997;35(5):266–74.

Human-Like Sensor Fusion Implemented in the Posture Control of a Bipedal Robot

Georg Hettich, Vittorio Lippi, and Thomas Mergner

Abstract Posture control represents the basis for many human sensorimotor activities such as standing, walking or reaching. It involves inputs from joint angle, joint torque, vestibular and visual sensors as well as fusions of the sensor data. Roboticists may draw inspirations from the human posture control methods when building devices that interact with humans such as prostheses or exoskeletons. This study describes multisensory fusion mechanisms that were derived from human perception of ego-motion. They were implemented in a posture control model that describes human balancing of biped stance during external disturbances. The fusions are used for estimating the disturbances and the estimates, in turn, command joint servo controls to compensate them (disturbance estimation and compensation, DEC, concept). An emergent property of the network of sensory estimators is an automatic adaptation to changes in disturbance type and magnitude and in sensor availability. Previously, the model described human and robot balancing about the ankle joints in the sagittal plane. Here, the approach is extended to include the hip joints. The extended human-derived model is again re-embodied in a biped posture control robot constructed with human anthropometrics. The robot is tested in direct comparison with human subjects. Results on hip and ankle sway responses to support surface rotation are described. Basic resemblance of the results suggests that the robot's DEC controls capture important aspects of the human balancing.

Keywords Sensor fusion • Postural control • Sensory feedback • Humanoid robot

1 Introduction

Sensors and sensor fusion play a fundamental role in the sensorimotor behavior of animals and humans. Their use offloads computational burdens to the periphery and early processing stages of the central nervous system (CNS; e.g. [1]). Furthermore,

G. Hettich (✉) • V. Lippi • T. Mergner
Neurocenter, Neurological University Clinic, Freiburg, Germany
e-mail: georg.hettich@uniklinik-freiburg.de; vittorio.lippi@uniklinik-freiburg.de; thomas.mergner@uniklinik-freiburg.de

A.R. Londral et al. (eds.), *Neurotechnology, Electronics, and Informatics*,
Springer Series in Computational Neuroscience 13, DOI 10.1007/978-3-319-15997-3_3

sensor data fusions represent the basis for the perceptual reconstruction of the external world and the interaction with it. Current understanding of the involved mechanisms in humans owes mainly to sensory physiology and to psychophysics, a research method that relates the perception to the physical stimuli it evokes, allowing inferences on the underlying information processing. The founders were, more than a century ago, Fechner and Weber (see [2]) and major contributions dealt with visual and vestibular mechanisms. Cybernetics then introduced engineering methods of describing information processing and control into biomedical research [3]. The present study uses psychophysical findings on human ego-motion perception and their model-based descriptions for the sensorimotor control of a humanoid robot. This represents a neurorobotics approach where neuroscientists apply engineering methods to unveil human neural control and roboticists draw inspirations from the human control methods [4].

Human sensorimotor control involves not only movement planning and movement commanding, but also posture control. Posture control is an instrumental constituent of skeletal motor activity. It copes with inter-segmental coupling torques and movement coordination, adequate buttressing of movements (e.g. push off), maintaining balance, and automatizing the compensation of external disturbances. Posture control functions may be selectively impaired in neurological patients as witnessed by disabling consequences. Both, sensory loss and cerebellar lesions cause ataxia with jerkiness of movements, dysmetria (inappropriate metrics), falls, and motor timing problems [5]. In basal ganglia diseases such as Parkinson's disease, the posture control impairment causes falls, akinesia (difficulties in movement execution), movement freezing, impaired motor adaptability to external disturbances, and muscular stiffness ('rigor') [6].

Modeling the role of sensors and sensor fusions in human posture control has been successful only recently. The problem to overcome was how humans manage to deal with sensory feedback despite long neural time delays (see [7]). Before, it was often held that passive joint stiffness and viscosity, stemming from intrinsic musculoskeletal properties and acting virtually without time delay, play a major role, for example in stabilizing biped stance [8]. Later work showed, however, that this owes primarily to the neural reflexes (ankle joint: [9, 10]; ankle, knee and hip joint: [11, 12]). Several types of reflexes appear to be involved, some with short time delay (40–80 ms) and others with long time delay (>100 ms), and this applies not only to proprioceptive reflexes, but also to the vestibular reflexes [13].

The total time delay of the reflexive feedback mechanisms in biped balancing is approximately 180 ms (e.g. [10]). Yet the neural control of biped balancing in the ankle joints is stable, owing mainly to the fact that the loop gain is very low, hardly exceeding the minimum required for the balancing [10, 14]. The sensory feedback stems primarily from joint angle and torque proprioception, the vestibular system and vision (see [15]). The underlying neural sensor fusions, often referred to as 'multi-sensory integration', allow humans to adapt their posture control to changes in the environmental conditions and to the availability of sensory information. They do so mainly by changing sensory weights, which has been called 'sensory reweighting' [10, 14, 16–18]. The sensory integration and reweighting mechanisms are still a topic of on-going research.

This paper presents a concept of human-derived sensor fusion mechanisms for use in the posture control of a humanoid robot that balances biped stance. In the following, basic aspects of the multi-sensory fusions are explained, before their use in the human posture control model is described and the model is implemented in a humanoid robot for balancing biped stance in the ankle joints. The model is then extended to include the hip joints in the balancing and is again re-embodied into a robot for direct robot-human comparisons. Finally, an outlook is given on how the control concept can further be extended in a modular control architecture for humanoid robots that we expect to show human-like characteristics when interacting behaviorally with humans or in the form of prostheses or exoskeletons.

2 Sensor Fusion and Posture Control Mechanisms

Sensor fusion is an important technical issue. Position tracking design technologies rely heavily on the integration of several sensors: e.g. inertial measuring units (IMUs) integrates gyros and accelerometers, and IMUs output itself is often fused with global positioning system (GPS) data. Published work on sensor fusion for postural control in robots typically used Kalman filters [19–22]. Simulation models for human posture control [23, 24] also implemented Kalman filters, combining in 'sensory integration centers' multiple sensory signals with centrally generated information (motor command) to find the most accurate sensory representation for a given environmental situation. Drawbacks of these approaches are high demands on computational power in multi degree of freedom (DoF) systems and problems of control stability if the plant is not accurately reflected in the model.

A different disturbance estimation method was used in the posture control model considered here. It proceeded from psychophysical work that investigated (i) which sensory information are humans using for their ego-motion perception during passive motion of the body or parts of it (e.g. head, trunk, legs, feet with respect to each or in space), (ii) how humans fuse sensor data to obtain information that is not directly available from their sensors (e.g. trunk motion in space), and (iii) how they obtain estimates of external disturbances that may affect the ego-motion. The approach was model-based and originally aimed to formally describe the experimentally obtained human responses in the form of time series and performance data.

The psychophysical studies showed, for example, that humans involve joint proprioceptive information when using the vestibular information arising in the head for estimating the kinematic state of the trunk and legs in space as well as of the haptically experienced body support. From this information, humans internally reconstruct the external disturbances, which in the experiments consisted of support surface rotation and translation, and experienced their self-motion as a consequence of these external physical stimuli (see [25, 26]).

The concept of external disturbance estimation was extended to include field forces such as gravity or Coriolis forces (e.g. [27]) and to contact forces such

as a push against, or a pull on the body [17, 28]. Neural correlates of some of the observed sensor fusions were found in neuron recordings in the vestibular nuclei [29, 30] and in cortical vestibular centers [31]. Furthermore, down and up channeling of vestibular signals in pathways of the spinal cord and their convergence with proprioceptive signals, have been described [32]. Also, representations of processed sensory signals in terms of kinematic variables have been observed in spino-cerebellar pathways [33–35].

It was hypothesized that humans use the same or similar sensory information as observed in, or inferred from the psychophysical studies also for their sensori-motor control, at least as concerns re-active (sensor-driven) responses to external disturbances. On this basis, human posture control experiments were performed and modeled, leading to a disturbance estimation and compensation, DEC, concept.

2.1 Sensor Fusion in the DEC Concept

The DEC concept involves essentially two steps of sensor fusion, schematically illustrated in Fig. 1. In the first step, information from several sensory transducers is fused to obtain measures of kinematic and kinetic variables. In the second step, these physical variables are combined to yield estimates of the external disturbances.

2.1.1 Fusion of Sensory Transducer Data

An example of the first step is the human sense of joint angle proprioception. It combines information from several sensory transducers such as muscle spindles, Golgi tendon organs and cutaneous receptors [36]. This also applies to the human perception of head on trunk rotation, which in addition is complicated by the fact that rotations between several segments of the cervical vertebral column are

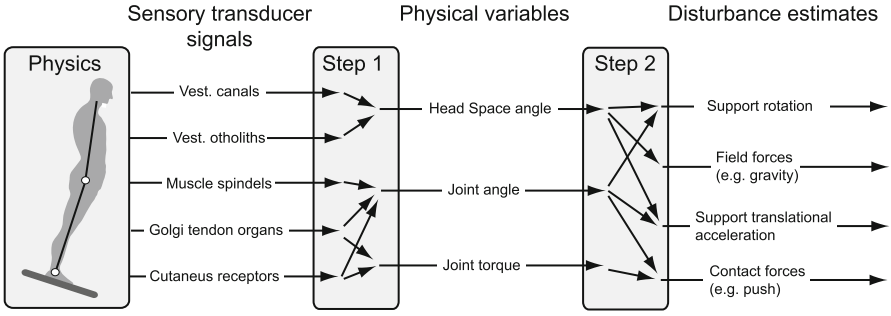

Fig. 1 Schematic illustration of the sensor fusion mechanisms. Information of sensory transducer signals is fused in the first step to yield physical variables. These variables are used in the second step to reconstruct external disturbances

involved. Yet, the result is a sense of angular head-on-trunk velocity and position, as if an angular rate sensor and a goniometer in a single joint were measuring head-trunk speed and rotation, respectively [37, 38].

Another example for the first step, well known to engineers who work with IMUs, is the fusion of angular and linear accelerometer signals. A problem with linear accelerometers is that they do not distinguish between inertial and gravitational forces (i.e. between linear acceleration and tilt of the sensor). There exists also a problem with the angular accelerometers, often used in the form of gyros that measure angular velocity. They show low frequency signal variations over time ('drifts'). Both problems can be solved for the earth vertical planes by fusing the inputs from the two sensors in an appropriate way. This has an analogy in the human vestibular system that is located in the inner ears. Its otolith organs and canal systems represent biological equivalents of linear and angular accelerometers, respectively [39]. The solutions for both, the technical system and its biological equivalent involve information of the gravitational vector. In the horizontal translational and rotational planes, however, there is no such information available, so that further sources of information are required. In technical systems, often the GPS is used. Humans usually use the visual system for this purpose.

In the following we will speak of joint angle and angular velocity sensors and by this we mean virtual sensors that result from step one. The same applies when we refer to the vestibular sensor and its three output measures, i.e. 3D angular velocity and linear acceleration in space and 2D orientation with respect to the gravitational vertical. These measures of the physical variables represent the inputs to the second step of the sensor fusions.

2.1.2 Disturbance Estimation

In the second step of Fig. 1, the signals of the variables resulting from step one are combined to reconstruct external disturbances that have impact on the body. In the DEC concept, it is assumed that four physical quantities suffice to define the external disturbances that affect human balancing in moderate stimulus conditions (body sway amplitudes and velocities, $<8°$ and $<80°$/s; frequencies, <3 Hz). The four types of external disturbances are: (1) Support surface rotation, (2) support surface translational acceleration, (3) field forces such as gravity, and (4) contact forces such as a pull on, or push against the body.

The second step in Fig. 1 was originally motivated by reports of the subjects in the aforementioned psychophysical experiments. When asked to report their percepts during passive rotations on a rotation chair, subjects typically started the report with the rotation of the chair, even though the percept primarily stems from the vestibular system in the head. Thus, without being aware of it, the subjects reconstructed the physical cause of their body rotation, i.e. the chair rotation in space, by internally reversing the linkages from the vestibular signal 'head rotation in space' via the proprioceptive signal 'trunk rotation relative to the head' to the haptical information of 'sitting on the chair'. This can formally be described in

terms of a transformation by which the trunk and chair kinematics are referenced to the vestibular derived notion of inertial space [25]. The concept applies to both, the vestibular-able subjects' estimation of 'support rotation' and 'support translational acceleration' in Fig. 1 (formal description in Sect. 2.2).

Vestibular-able subjects furthermore use vestibular information for estimating body lean with respect to the earth vertical when balancing stance in the sagittal plane. From lean of the whole-body's center of mass (COM_B) above the ankle joints and knowledge about body mass and COM height they to estimate the required ankle joint torque to compensate for the gravity effect. For field forces in general, it is known that subjects, when presented with a new aspect of a field force, they perceive it and readily learn to counteract its impact on the body. Thereafter, they no longer perceive it consciously, as has been shown in Coriolis force experiments by Lackner and DiZio [27]. The subconscious estimation and compensation of field forces makes it difficult to study them psychophysically.

Estimation of contact force effects on the ankle joint balancing requires internal measurement of the overall ankle torque (or related measures such as the center of pressure, COP, shift) and the distinct contributions to the ankle torque such as active torque and the gravitational torque. Details have been described before [40] for sagittal plane balancing of moderate disturbances, where the balancing is performed predominantly in the ankle joints ('ankle strategy'; [41, 42]). In such situations, a single inverted pendulum, SIP, can approximately mimic human biomechanics.

2.1.3 Feedback Control Model

The two steps of sensor fusion are used for feedback control of one joint (Fig. 2). Its lower half represents a servo control consisting of a negative joint angle proprioceptive feedback and a controller with a proportional and a derivative factor (PD controller). The controller provides the motor command that is transformed by the muscles into joint torque (not shown in Fig. 2). Given appropriate parameters

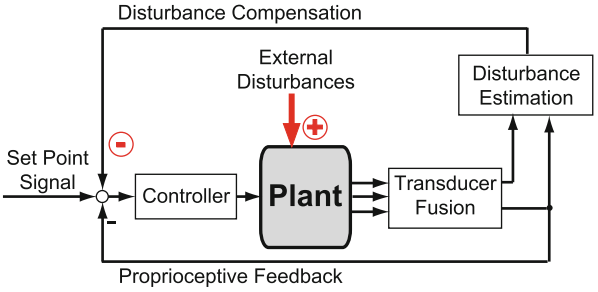

Fig. 2 Simplified feedback control scheme of the Disturbance Estimation and Compensation (DEC) concept. The *Proprioceptive Feedback* loop yields a servo control, by which actual joint angle approximately equals the desired joint angle. Signals from the *Disturbance Estimation* part command the servo to compensate the disturbances

of the servo control, actual joint angle approximately equals the desired joint angle without requiring a feed forward of plant dynamics. Feedback from passive stiffness and viscosity with virtual zero delay is assumed to amount to 10 % of the proprioceptive feedback (not shown in Fig. 2).

Noticeably, in the SIP scenario, the P and D factors identified in human stance control are surprisingly low [10, 14, 43]. They appear to be geared to the pendulum mass m, the height h of the COM, and gravitational acceleration g (mgh; $P \approx mgh$; $D \approx mgh/4$). The values that humans use for balancing are only slightly higher. A consequence is that the servo alone is insufficient to cope with external disturbances such as gravity or a push against the body.

The upper half of Fig. 2 shows schematically the loop that carries the estimates of the external disturbances and compensates for them. To insure control stability in face of the neural time delays, the field and contact force estimates are not used directly, but in the form of body-space angle equivalents. For example, the estimate of body lean commands the servo to compensate for the gravitational torque it produces. Then, the loop gain (at the level of the controller) is raised accordingly. Noticeably, the increase occurs only at the time of, and to the extent that the disturbance has impact. Note furthermore that disturbance compensation applies even with superposition of several disturbances as well as with superposition of disturbances and voluntary movements [39].

The DEC loops are not simply representing additional sensory feedback loops, but are thought to represent long-latency loops through basal ganglia and cerebral cortex [40]. They contain central detection thresholds and allow for voluntary scaling the disturbance compensations and for predictions of the disturbance estimates (e.g. self-produced disturbances during voluntary movements).

It has been shown by comparing human data with model simulations that the DEC concept describes the human ankle joint balancing in a variety of disturbance scenarios. Furthermore, the control automatically adapts to changes in disturbance scenario and magnitude as well as sensor availability. This also applied when the model was implemented in a humanoid robot with ankle joint actuation, and tested in the human experimental setup (PostuRob I; overview [39, 40]). These experiments demonstrated that the DEC concept is robust against real world problems such as inaccurate and noisy sensors and mechanical dead zones.

The following describes an extension of the DEC concept to include the hip joints in the balancing. The hip joints contribute considerably when strong transient disturbances are applied (‘hip strategy’; [41, 42]). Then humans may use hip joint accelerations to produce shear forces under the feet to counteract body COM excursions. Another, more common involvement of the hip joints deals with adding to the task of body COM balancing a secondary task of keeping the orientation of the upper body upright. This ‘head stabilization in space’ task is thought to improve under dynamic conditions such as walking the sensory feedback from the vestibular and visual cues arising in the head [44, 45].

2.2 Extended DEC Concept: Sensor Fusion in Ankle and Hip Joint

The extension of the DEC concept for including the hip joints entails that double inverted pendulum (DIP) rather than SIP biomechanics are considered, and with this the occurrence of inter-segmental coupling torques [46]. In an extended DEC concept for DIP biomechanics, we postulated two DEC controls, one for the hip joint and the other for the ankle joint. This approach allowed to use again the above described sensor fusion principles for disturbance estimation.

2.2.1 DIP Biomechanics

The DIP biomechanical model is shown in Fig. 3. In Fig. 3a, COM_T, COM_L and COM_B stand for the COM of the trunk (including head and arms), leg and whole body, respectively. Leg length is given by l_L, the trunk and leg COM heights are given by h_T and h_L, respectively. Figure 3b shows the angular excursion of the trunk and leg segments with respect to earth vertical (trunk-space angle α_{TS}, leg-space angle α_{LS}). Angular excursion of COM_B is defined as body-space angle α_{BS}. The foot has firm contact with the support surface, therefore platform tilt angle equals foot angle with respect to earth horizontal (foot-space angle α_{FS}). The trunk-leg joint angle is α_{TL} and the leg-foot joint angle is α_{LF}. In perfectly upright body position, all angles are 0°. Angular speed during reactive human balancing can be assumed to be slow enough such that the Coriolis and centrifugal forces can be neglected; the model can be linearized using small angle approximation, assuming that the subject is maintaining his upright position close to the vertical.

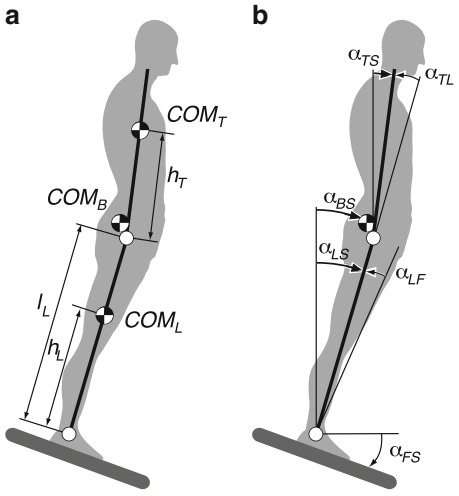

Fig. 3 DIP biomechanics

Maintaining upright stance in the situation of a support surface tilt in the sagittal plane requires corrective joint torque in the ankle and hip joints. This torque can be expressed by the following equations for hip torque T_H

$$T_H = \left(J_T + m_T h_T^2 + m_T l_L h_T\right) \ddot{\alpha}_{LS} + \left(J_T + m_T h_T^2\right) \ddot{\alpha}_{TL} - (m_T g h_T)\alpha_{LS} - (m_T g h_T)\alpha_{TL} \quad (1)$$

and for ankle torque T_A

$$T_A = \left(J_L + J_T + m_L h_L^2 + m_T (l_L^2 + h_T^2 + 2 l_L h_T)\right) \ddot{\alpha}_{LS} + \left(J_T + m_T h_T^2 + m_T l_L h_T\right) \ddot{\alpha}_{TL} - (m_L g h_L + m_T g l_L + m_T g h_T)\, \alpha_{LS} - (m_T g h_T)\alpha_{TL} \quad (2)$$

where $\ddot{\alpha}_{LS}$, and $\ddot{\alpha}_{TL}$ represent angular accelerations, m_L *and* m_T are the segment masses, and J_L and J_T the segment moments of inertia (details in Al Bakri [47]).

In the extended DEC concept for the DIP, the hip joint is used for orienting and balancing the trunk segment and the ankle joint for balancing the whole-body using two separate controls. The vestibular-derived signals used for the controls are: the trunk-space angle α_{ts}, trunk-space angular velocity $\dot{\alpha}_{ts}$, and head translational acceleration $\ddot{x}_{Head}$. The proprioceptive signals are: the trunk-leg angle α_{tl} and the trunk-leg angular velocity $\dot{\alpha}_{tl}$; the leg-foot angle α_{lf} and the leg-foot angular velocity $\dot{\alpha}_{lf}$. Uppercase letters in the angle subscripts indicate physical angles, lowercase letters the sensory derived representations of these angles.

2.2.2 Hip Joint Control

The DEC control of the trunk reflects the principles described already above for the SIP biomechanics. Considering the support surface tilt scenario in the sagittal plane shown in Fig. 3, the legs tend to rotate somewhat with the platform, due to passive ankle joint stiffness and a imperfect tilt compensation that is typical in humans with eyes closed. Since the legs represent the support base for the trunk, an eccentric hip rotation represents:

(a) A support base tilt disturbance for the trunk, evoked by the leg rotation, α_{LS}.
(b) A hip translational acceleration $\ddot{x}_{Hip}$. It produces a hip torque (T_{H_in}) in relation to m_T, h_T and J_T. This torque is treated here as if it were an external disturbance rather than an inter-segmental coupling effect.

Furthermore, trunk lean is associated with a gravitational hip torque disturbance (T_{H_grav}).

These three disturbances are estimated in the DEC control of the hip joint control in the following form:

(i) Estimation of leg tilt, $\widehat{\alpha}_{LS}$. This estimate is derived from fusing the vestibular velocity signal $\dot{\alpha}_{ts}$ with the proprioceptive velocity signal $\dot{\alpha}_{tl}$ by $\dot{\alpha}_{ls} = \dot{\alpha}_{ts} - \dot{\alpha}_{tl}$ (Assumption: these transformations are performed as vector summations of co-planar rotations, separately for the three body planes). $\widehat{\alpha}_{LS}$ is obtained by applying to the signal a detection threshold and a mathematical integration.

(ii) Estimation of hip translational acceleration $\widehat{\ddot{x}}_{Hip}$. The estimate is derived from fusing the vestibular signals $\dot{\alpha}_{ts}$ and $\ddot{x}_{Head}$ in the form

$$\widehat{\ddot{x}}_{Hip} = \ddot{x}_{Head} - \frac{d\,(\dot{\alpha}_{ts})}{dt} l_T, \tag{3}$$

where the trunk length l_T gives the height of the vestibular system above the hip. $\widehat{\ddot{x}}_{Hip}$ is, in turn, used to estimate the inertial disturbance torque in the form of

$$\widehat{T}_{H\_in} = \widehat{\ddot{x}}_{Hip} m_T h_T. \tag{4}$$

(iii) Estimation of gravitational hip torque $\widehat{T}_{H\_grav}$. Using the vestibular signal α_{ts}, the third and fourth term of Eq. (1) becomes

$$\widehat{T}_{H\_grav} = m_T g h_T \alpha_{ts}. \tag{5}$$

2.2.3 Ankle Joint Control

The DEC control of the ankle joints is used to balance the whole body above the ankle joint. To this end, it combines the leg and trunk angular excursions in the form of COM_B excursions in space, α_{BS}. In this respect, also the DEC control of the ankle deals with a SIP. The following three disturbances that have impact on the ankle torque during support surface tilts are:

(a) The support surface tilt, α_{FS}.
(b) The gravitational ankle torque, T_{A_grav}. It results from α_{BS}.
(c) Inter-segmental coupling torque in the ankle joint, T_{A_coup}. It arises with angular acceleration of the trunk segment.

For the estimation of these disturbances, the DEC control of the ankle fuses sensory signals from the vestibular system and the hip *and* ankle joint proprioception. To this end, sensory signals from the hip DEC control are transmitted ("down-channeled") to the ankle joint DEC control. The estimates are:

(i) Estimation of foot-space rotation, $\widehat{\alpha}_{FS}$. This estimate uses a down-channeled version of $\dot{\alpha}_{ls}$ and combines it with the ankle joint angular velocity signal $\dot{\alpha}_{lf}$ in the form

$$\dot{\alpha}_{fs} = \dot{\alpha}_{ls} - \dot{\alpha}_{lf}. \tag{6}$$

Analogous to $\widehat{\alpha}_{LS}$, the estimate $\widehat{\alpha}_{FS}$ contains a detection threshold and a mathematical integration.

(ii) Estimation of gravitational ankle torque, $\widehat{T}_{A\_grav}$. This estimate relates to the third and fourth term of Eq. (2), which are mathematically combined in the COM_B excursion α_{bs}. From this, the gravitational torque is obtained in the form

$$\widehat{T}_{A\_grav} = m_B g h_B \alpha_{bs} \tag{7}$$

where m_B represents whole-body mass and h_B represents COM_B height. Small angular excursions allow approximating h_B by a constant value.

(iii) Estimation of the inter-segmental coupling torque, $\widehat{T}_{A\_coup}$. This torque arises upon trunk rotational acceleration and tends to evoke a leg counter-rotation. In view of the DEC concept, the trunk acceleration exerts a 'push' against the hip like a contact force disturbance (compare external torque estimate in [40]). This disturbance is expressed by the second component of Eq. (2). Since its implementation was not critical for the stability of the DIP control in the present context (compare [48]), it is omitted in the following.

The hip and the ankle DEC controls can be viewed as separate control modules that are interconnected by 'down-channeling' of sensory information from the hip DEC control to the ankle DEC control. Recent experimental evidence suggests in addition an "up-channeling" of information between them (details in [49]). A schematic illustration of the DIP control is given in Fig. 4.

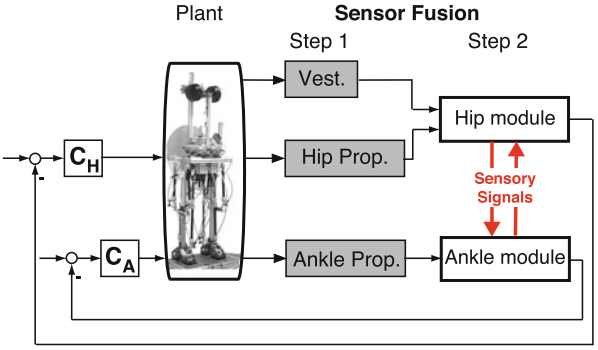

Fig. 4 Basic aspects of the DIP control concept used for PostuRob II. C_H and C_A are the hip and ankle controllers, Vest. is the vestibular input while Hip Prop. and Ankle Prop. are the proprioceptive inputs

3 Human and Robot Experiments

The extended DEC concept was tested experimentally by comparing sway to support surface tilt in the sagittal plane with sway of a bipedal robot (PostuRob II) in a human posturography laboratory.

3.1 Bipedal Robot PostuRob II

PostuRob II consists of mechanical, mechatronic, and computer control parts. The mechanical part comprises one trunk segment, two legs and two feet, with a total mass of 59 kg and a total height of 1.78 m. Two hip joints and two ankle joints connect the segments (4 DOF in the sagittal plane; Fig. 5). The mechatronic part comprises an artificial vestibular sensor [39] that is fixed to the trunk segment. Artificial pneumatic 'muscles' (FESTO, Esslingen, Germany; Typ MAS20) connected with serial springs (spring rate 25 N/mm) are used for actuation. An electronic inner torque control loop ensures that actual torque equals approximately desired torque. Sensory signals are sampled at 200 Hz by an acquisition board. Computer control is performed through a real time PC that executes a compiled Simulink model using Real-Time Windows Target (The Math Works Inc., Natick, USA).

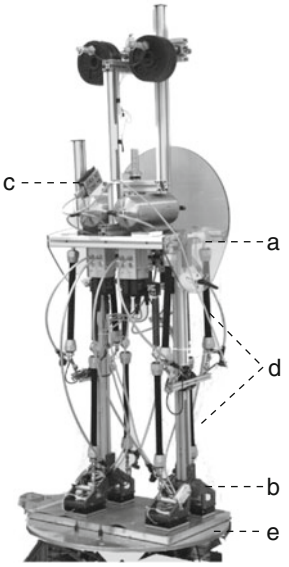

Fig. 5 PostuRob II. The robot consists of trunk, leg, and foot segments interconnected by the hip joints (*a*) and ankle joints (*b*). Sensory information stems from artificial vestibular system (*c*) and ankle and hip joint angle and angular velocity sensors. Actuation is through pneumatic 'muscles' (*d*). PostuRob II stands freely on a motion platform (*e*)

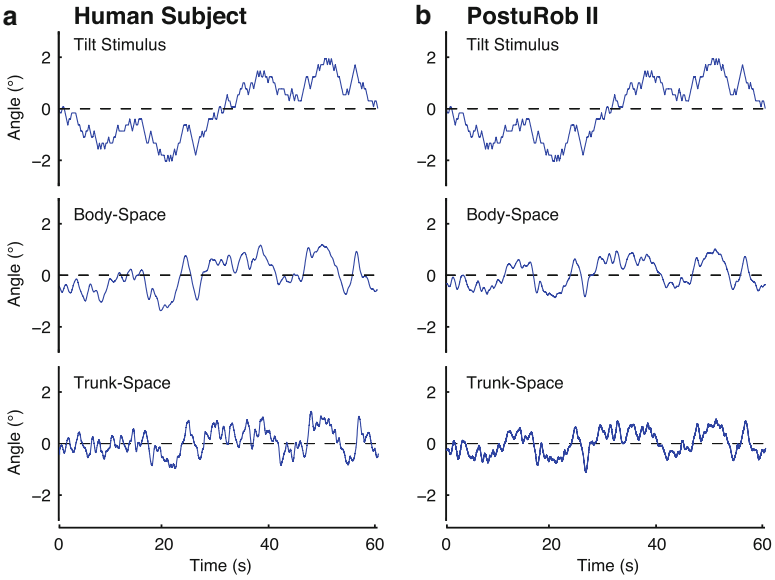

Fig. 6 Tilt stimulus and angular excursion responses of body in space and trunk in space from one representative subject (**a**) and of PostuRob II (**b**)

3.2 Experimental Methods

Seven healthy human subjects (3 female; mean age, 28 ± 3 years) participated after giving their informed consent. The subjects (eyes closed) and the robot stood freely on a motion platform (see Fig. 5), while six successive pseudorandom ternary tilt sequences, each 60.5 s long, with peak-to-peak amplitude of 4° were applied (PRTS stimulus; frequency range 0.017–2.2 Hz; [10]). The first rows in Fig. 6a, b show one 60.5 s long tilt stimulus sequence.

Trunk, leg, and COM_B angular excursions in space were calculated on the basis of opto-electronically measured marker data (Optotrak 3020®; Waterloo, Canada) that were recorded with a sampling frequency of 100 Hz. Data analysis took into account human anthropometric measures [50] and was performed using custom-made software programmed in Matlab (The MathWorks, Natick, USA). The responses were expressed as gain and phase from the frequency response function [10] in a form where zero gain means no body excursion and unity gain means that body angular excursion equals platform tilt. Phase represents the temporal relationship between stimulus and response. Variability of averaged values was expressed as 95 % confidence limits [51].

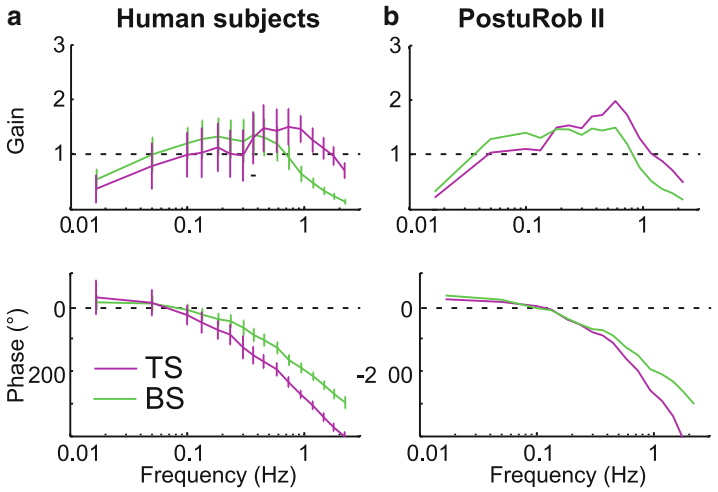

Fig. 7 Tilt responses in terms of gain, phase and coherence curves of human subjects (**a**; 7 subjects, medians ±95 confidence intervals) and PostuRob II (**b**)

3.3 Results

Subjects and PostuRob II balanced the tilts in similar ways. Time series of the responses of one subject and the robot are shown in Fig. 6. Note that the responses resemble each other, both for the body-space and the trunk-space responses. As shown in Fig. 7, the resemblance also holds for the mean gain and phase curves of the human subjects and the robot. In both, the gain values of trunk-space (TS) and of body-space (BS) vary similarly with stimulus frequency. In the low frequency range (<0.3 Hz), TS gain is lower than BS gain. In contrast, in the high frequency range (>0.3 Hz), TS gain exceeds BS gain, while the phase shows a larger phase lag.

4 Conclusions

The here proposed feedback control system of a bipedal robot takes advantage of the sensor fusion and posture control mechanisms that were derived from findings in human experiments. The disturbance estimators that were used are non-iterative and remarkably simpler than estimators that were used in Kalman filters. Furthermore, the multi-sensory feedback control is performed without integrating any dynamic model of the whole body in the control architecture. Filtering the estimates through a nonlinear operation provided by a deadband threshold tends to reduce noise, which appears to stem mainly from vestibular signals [39]. The noise shows 1/f properties and therefore overlaps with the bandwidth of human sensorimotor behavior. The threshold shuts off any estimator if there is no corresponding disturbance, which

in a multi-DoF system may help to prevent accumulation of noise. The threshold also explains a non-linear behavior in the human disturbance responses that were observed with increase in stimulus magnitude [14]. Due to the non-linearity, small stimuli yield relatively smaller responses than larger stimuli. This is an aspect of the automatic sensory re-weightings, which emerged from the sensory network of estimators. Other important aspects of it are that the control automatically adjusts to changes in disturbance type and to sensor availability (for SIP, see [40]).

The here obtained good match of the data between the human subjects and PostuRob II suggests that the proposed sensor fusion and posture control mechanism capture important constituents of the human balancing system. The application of the extended DEC concept to the balancing of upright stance using hip and ankle joints in terms of a DIP required the integration of sensory signals from almost the whole body. In a recent study that used this approach, coordination between hip and ankle joint emerged from the multi-sensory feedback control [49]. These experiences with the extended DEC concept led us explore its usefulness with further DoF in a modular control architecture. In the generalized description, each DoF is controlled by one DEC control, which stabilizes a SIP (defined by the COM and moment of inertia of the segments above) on a moving support (given by the upper end of the segment below). Adjoining DEC controls are synergistically interconnected to exchange sensory information and disturbance estimates [52].

Taken together, although optimizing the DEC concept and its control parameters is still under research, the concept proved to have several promising features. These include: (i) a computationally very simple implementation, since almost all sensor fusions are based on algebraic operations; (ii) the control complexity scales linearly with the number of joints, since every joint is controlled as if a SIP and the signals are exchanged only between adjoining modules; (iii) noise rejection makes it possible to fuse the input of an high number of sensors; and (iv) the system, originally proposed for its predictive power of human behavior, can be employed to control actuated prostheses and exoskeletons to provide users with a human-like feeling.

Acknowledgements Supported by the European Commission (FP7-ICT-600698 H2R). GH is supported by the Konrad-Adenauer-Stiftung.

References

1. Wehner R. Matched filters - neural models of the external world. J Comp Physiol A. 1987;161:511–31.
2. Stevens SS. Psychophysics. Introduction to its perceptual, neural, and social prospects. New York, NY: John Wiley & Sons; 1975.
3. Wiener N. Cybernetics. Sci Am. 1948;179:14–8.
4. Mergner T, Tahboub KA. Neurorobotics approaches to human and humanoid sensorimotor control. J Physiol Paris. 2009;103:115–8.
5. Bastian AJ. Mechanisms of ataxia. Phys Ther. 1997;77:672–5.

6. Visser JE, Bloem BR. Role of the basal ganglia in balance control. Neural Plast. 2005;12: 161–74.
7. Rack PMH. Limitations of somatosensory feedback in control of posture and movement. In: Brooks VB, editor. Handbook of physiology: the nervous system, vol. 2. Baltimore, MD: Williams and Wilkins; 1981.
8. Winter DA, Patla AE, Prince F, Ishac MG, Gielo-Perczak K. Stiffness control of balance in quiet standing. J Neurophysiol. 1998;80:1211–21.
9. Morasso PG, Schieppati M. Can muscle stiffness alone stabilize upright standing? J Neurophysiol. 1999;82:1622–6.
10. Peterka RJ. Sensorimotor integration in human postural control. J Neurophysiol. 2002;88: 1097–118.
11. van Soest AJ, Haenen WP, Rozendaal LA. Stability of bipedal stance: the contribution of cocontraction and spindle feedback. Biol Cybern. 2003;88:293–301.
12. Edwards W. Effect of joint stiffness on standing stability. Gait Posture. 2007;25:432–9.
13. Britton TC, Day BL, Brown P, Rothwell JC, Thompson PD, Marsden CD. Postural electromyographic responses in the arm and leg following galvanic vestibular stimulation in man. Exp Brain Res. 1993;94:143–51.
14. Maurer C, Mergner T, Peterka RJ. Multisensory control of human upright stance. Exp Brain Res. 2006;171:231–50.
15. Horak FB, Macpherson JM. Postural orientation and equilibrium. In: Rowell L, Shepherd J, editors. Handbook of physiology. New York, NY: Oxford University Press; 1996.
16. Nashner LM, Berthoz A. Visual contribution to rapid responses during postural control. Exp Brain Res. 1978;150:403–7.
17. Mergner T, Maurer C, Peterka RJ. A multisensory posture control model of human upright stance. Prog Brain Res. 2003;142:189–201.
18. van der Kooij H, Peterka RJ. Non-linear stimulus-response behavior of the human stance control system is predicted by optimization of a system with sensory and motor noise. J Comput Neurosci. 2011;30(3):759–78.
19. Tahboub K, Mergner T. Biological and engineering approaches to human postural control. Integ Comput Aid Eng. 2007;13:1–17.
20. Mahboobin A, Loughlin PJ, Redfern MS, Anderson SO, Atkeson CG, Hodgkins JK. Sensory adaptation in balance control: lessons for biomimetic robotic bipeds. Neural Netw. 2008;21(4):621–7.
21. Tahboub K. Biologically-inspired humanoid postural control. J Physiol Paris. 2009;103: 195–210.
22. Klein TJ, Jeka J, Kiemel T, Lewis MA. Navigating sensory conflict in dynamic environments using adaptive state estimation. Biol Cybern. 2011;105:291–304.
23. van der Kooij H, Jacobs R, Koopman B, Grootenboer H. A multisensory integration model of human stance control. Biol Cybern. 1999;80:299–308.
24. Kuo AD. An optimal state estimation model of sensory integration in human postural balance. J Neural Eng. 2005;2:235–49.
25. Mergner T, Huber W, Becker W. Vestibular-neck interaction and transformations of sensory coordinates. J Vestibul Res Equil. 1997;7:119–35.
26. Mergner T, Rosemeier T. Interaction of vestibular, somatosensory and visual signals for postural control and motion perception under terrestrial and microgravity conditions – a conceptual model. Brain Res Rev. 1998;28:118–35.
27. Lackner JR, DiZio P. Rapid adaptation to Coriolis force perturbations of arm trajectories. J Neurophysiol. 1994;72:299–313.
28. Mergner T. The Matryoshka Dolls principle in human dynamic behavior in space – a theory of linked references for multisensory perception and control of action. Cah Psychol Cogn. 2002;21:129–212.
29. Boyle R, Pompeiano O. Convergence and interaction of neck and macular vestibular inputs on vestibulospinal neurons. J Neurophysiol. 1981;45:852–68.

30. Anastasopoulos D, Mergner T. Canal-neck interaction in vestibular nuclear neurons of the cat. Exp Brain Res. 1982;46:269–80.
31. Mergner T, Becker W, Deecke L. Canal-neck interaction in vestibular neurons of the cat's cerebral cortex. Exp Brain Res. 1985;61:94–108.
32. Coulter JD, Mergner T, Pompeiano O. Effects of static tilt on cervical spinoreticular tract neurons. J Neurophysiol. 1976;39:45–62.
33. Bosco G, Poppele RE. Representation of multiple kinematic parameters of the cat hindlimb in spinocerebellar activity. J Neurophysiol. 1997;78:1421–32.
34. Poppele RE, Bosco G, Rankin AM. Independent representations of limb axis length and orientation in spinocerebellar response components. J Neurophysiol. 2002;87:409–22.
35. Casabona A, Valle MS, Bosco G, Perciavalle V. Cerebellar encoding of limb position. Cerebellum. 2004;3:172–7.
36. Gandevia SC, Refshauge KM, Collins DF. Proprioception: peripheral inputs and perceptual interactions. Adv Exp Med Biol. 2002;508:61–8.
37. Mergner T, Nardi GL, Becker W, Deecke L. The role of canal-neck interaction for the perception of horizontal trunk and head rotation. Exp Brain Res. 1983;49:198–208.
38. Mergner T, Siebold C, Schweigart G, Becker W. Human perception of horizontal trunk and head rotation in space during vestibular and neck stimulation. Exp Brain Res. 1991;85: 389–404.
39. Mergner T, Schweigart G, Fennell L. Vestibular humanoid postural control. J Physiol Paris. 2009;103:178–94.
40. Mergner T. A neurological view on reactive human stance control. Annu Rev Control. 2010;34:177–98.
41. Nashner L, McCollum G. The organization of human postural movements: a formal basis and experimental synthesis. Behav Brain Sci. 1985;8:135–72.
42. Horak FB, Nashner LM. Central programming of postural movements: adaptation to altered support-surface configurations. J Neurophysiol. 1986;55:1369–81.
43. Alexandrov AV, Frolov AA, Horak FB, Carlson-Kuhta P, Park S. Feedback equilibrium control during human standing. Biol Cybern. 2005;93:309–22.
44. Bronstein AM. Evidence for a vestibular input contributing to dynamic head stabilization in man. Acta Otolaryngol. 1988;105:1–6.
45. Pozzo T, Berthoz A, Lefort L, Vitte E. Head stabilization during various locomotor tasks in humans. II. Patients with bilateral peripheral vestibular deficits. Exp Brain Res. 1991;85: 208–17.
46. Zajac FE, Gordon ME. Determining muscle's force and action in multi-articular movement. Excerc Sport Sci Rev. 1989;17:187–230.
47. Al Bakri M. Development of a mathematical model and simulation environment for the postural robot (PostuRob II). 2008. Available from http://www.posturob.uniklinik-freiburg.de
48. Hettich G, Fennell L, Mergner T. Double inverted pendulum model of reactive human stance control. Multibody Dynamics Conference 2011. Available from http://www.posturob.uniklinik-freiburg.de
49. Hettich G, Assländer L, Gollhofer A, Mergner T. Human hip-ankle coordination emerging from multisensory feedback control. Hum Mov Sci. 2014;37:173.
50. Winter DA. Biomechanics and motor control of human movement. 2nd ed. New York, NY: Wiley; 1990.
51. Otnes RK, Enochson LD. Digital time series analysis. New York, NY: Wiley; 1972.
52. Lippi V, Mergner T, Hettich G. A bio-inspired modular system for humanoid posture control. In: Ugur E, Oztop E, Morimoto J, Ishii S (editors), Proceedings of IROS 2013 Workshop on Neuroscience and Robotics. "Towards a robot-enabled, neuroscience-guided healthy society", November 3, 2013, Tokyo, Japan

Microchannel Scaffolds for Neural Signal Acquisition and Analysis

Rouhollah Habibey, Asiyeh Golabchi, and Axel Blau

Abstract Replica-casting finds wide application in soft lithography and microfluidics. Most commonly, structures are molded with micro- to nano-patterned photoresists as master casts into polydimethylsiloxane (PDMS). PDMS features many favorable properties. It reproduces geometric details with nanometer fidelity, has low cytotoxicity and is transparent in the visible spectrum. It is furthermore biostable both *in vitro* and *in vivo*, can be plasma-bonded to itself, has low water permeability and is easy to handle and process. After curing, the PDMS can be peeled from the master and latter usually be reused if patterns are not undercut. Here, we describe the straightforward replica-molding process for devices that can be exploited either as perforated microchannel scaffolds for the *in vitro* use in axonal guidance and regeneration studies on microelectrode arrays (MEAs) or for the production of tissue-conformal *in vivo* MEAs for neuroprosthetic applications.

Keywords Neuroengineering • Microchannel confinements • Polymer composite neuroprosthetics • Multi-level photolithography • Polydimethylsiloxane (PDMS)

1 Introduction

In microfluidics, PDMS microchannel systems [21, 23, 24] inspired by Taylor *et al.*, allow the separation of somata from their axons in two different fluidic environments [1]. Over the last decade, devices like these have been extensively utilized for studying axonal injury and regeneration, myelination, protein and mRNA synthesis, as well as transport phenomena [2–6]. Inexpensive microlithography techniques [22] for the generation of microtunnels have been used recently to structure networks in variable spatial designs. They allow microwell-confined populations of neural networks to connect through microchannels [7]. Microchannels can also be utilized in electrophysiological studies of neural networks *in vitro* by placing cells in specific substrate locations including the electrodes [8, 9]. By combining microchannels

R. Habibey • A. Golabchi • A. Blau (✉)
Department of Neuroscience and Brain Technologies (NBT), Neurotechnologies (NTech), Fondazione Istituto Italiano di Tecnologia (IIT), Via Morego 30, 16163 Genoa, Italy
e-mail: axel.blau@iit.it

A.R. Londral et al. (eds.), *Neurotechnology, Electronics, and Informatics*,
Springer Series in Computational Neuroscience 13, DOI 10.1007/978-3-319-15997-3_4

with microelectrode arrays (MEAs), activity can be selectively recorded from axons. In addition, amplitudes of extracellularly recorded signals from neurites are usually amplified by two orders of magnitude (millivolts instead of tens of microvolts) [10, 11]. In a non-conventional fabrication scheme, microchannel devices can also be transformed into MEAs. Filling the cavities of multi-level microchannel scaffolds with electrically conductive polymers or composite materials is a rapid prototyping approach for the design of various *in vitro* and *in vivo* recording and stimulation devices [12]. This opens the door for both application-specific prototyping as well as mass production of more tissue-mimetic neuroprosthetic recording and stimulation devices. After a brief methodological description of the general device fabrication steps, we present exemplary results on device exploitation as physical cell culture guidance cues and as MEAs for neuroprosthetics.

2 Methods

2.1 Fabrication of Multi-level PDMS Microchannel Devices

Bi-level patterns can be casted into high-aspect ratio negative photoresist (*e.g.*, SU-8) in a two-step photolithography technique using separate masks (Expert, Silvaco). To generate both microchannels and perforating vias, the first mask defines all features, whereas the second mask delineates the through-holes only. The principle fabrication steps and overall process flow are depicted in Fig. 1: A clean silicon wafer (a) is spin-coated with the first photo resin layer (<150 μm) (b) and photo cross-linked through a first photomask to define both the channels and the sockets for vias (c). The procedure is repeated in (d) and (e) for the second photoresist layer (<150 μm) to define the via through-holes. After removing the uncured photoresin in a developing step (f), the bi-level microstructure (g) can be covered with PDMS pre-polymer (h), cured after its leveling, and be peeled off to result in a microchannel scaffold with via holes (i). Such microchannels can either be used as physical guidance cues for axons and dendrites or be filled with conductive polymers (*e.g.*, PEDOT:PSS, carbon-polymer composites) (j) and backside-insulated (k) to yield all-polymer MEAs (*polyMEA*s) with electrodes and contact pads at the via holes for their application *in vitro* or *in vivo* (l).

2.2 Conductive Materials

If not stated differently, all materials were purchased from Sigma-Aldrich. A composite of carbon, graphite, and poly (3,4-ethylenedioxythiophene):polystyrene sodium sulfonate (PEDOT:PSS) (p Jet 700, Clevios) with up to 5 % of conductivity enhancers was used as a rubber-like electrode-, conductive track- and connection pad-filling. The carbon/graphite/PEDOT:PSS composite was mixed into pre-mixed

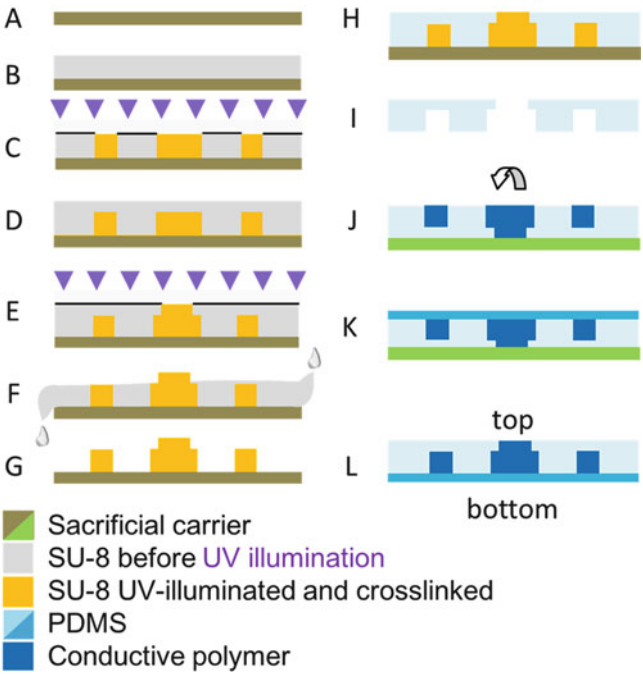

Fig. 1 Process flow of master generation (**a**–**f**) and microchannel replica molding from master in PDMS (**g**–**i**). The scaffold can either be used directly in neural guidance studies or be functionalized *e.g.*, with conductive polymers (**j**–**l**)

PDMS prepolymer and curing agent (Sylgard 184, Dow Corning) in a 1:1:3 ratio until its DC resistivity dropped below 10 kΩ over a distance of 5 mm. The track-, contact pad- and electrode-cavities were filled with the conductive material by spreading it onto the *polyMEA* scaffold. Excess material was removed by first swiping the surface with the edge of a ruler, then with a cotton swab and filter paper. This procedure removed the shortcuts between pads and tracks. In a final step, the surface of the *polyMEA* was cleaned by rolling a lint remover over it. To ensure that no shortcuts had remained, adjacent contact pads were probed by an ohmmeter. The conductive composite was cured at 120 °C for one hour. The *polyMEA*s were then backside-insulated by a second layer of PDMS. The contact pads of *in vivo polyMEA* probes were slid between the pins of Omnetics connectors. A folded laser transparency between the folded *polyMEA* helped in pressing the pads against the connector pins, thereby establishing electrical contact. A thin PDMS coat can be used for pad/pin insulation thereafter. Device biocompatibility was tested in cell culture. The electrical characteristics were determined by electrical impedance spectroscopy. *PolyMEA* recording functionality was validated with cortical cultures after 7 days *in vitro* (DIV).

2.3 Electrochemical Characterization of polyMEA Electrodes

The electrodes of *polyMEA*s were characterized by electrochemical impedance spectroscopy (EIS). The *polyMEA*s were placed in a custom-made Faraday box and their pads sequentially connected by a gold-coated spring-contact probe. The electrodes were immersed in saturated KCl at room temperature. A silver/silver chloride wire (Ø1 mm) was used as a reference electrode and a Pt sheet ($\sim 2 \times 3$ mm^2) as the counter electrode. Impedance spectroscopy was performed at frequencies between 1 Hz and 100 kHz (Perstat 2273, Princeton Applied Research).

2.4 Cell Culture

If not stated differently, all cell culture chemicals were purchased from Invitrogen. PDMS *in vitro polyMEA*s and commercial MEAs (Multi Channel Systems), PDMS caps [13] and PDMS microchannel tiles were autoclaved at 120 °C for 20 min before being moved to the sterile hood. To increase their surface hydrophilicity, MEAs and *polyMEA*s were exposed to oxygen plasma (0.5–2 min, 50 W, 2.45 GHz, 0.3 mbar O_2) [femto, Diener]. Their central surface was then coated with 20 μL of 0.1 mg/mL poly-D-lysine (PDL) and 0.05 mg/mL laminin, which was allowed to dry in vacuum. To remove soluble PDL, MEAs were rinsed twice with sterile ultrapure water and dried. After complete water evaporation, the PDMS microchannels were aligned on the surface of the commercial MEAs using a sterile water droplet. The crossing points of the microchannels were placed on the electrodes. Therefore, every microchannel included eight electrodes in one row or column (*e.g.*, 68 to 61 in Fig. 2). Cell suspensions (rat E18) were prepared following standard protocols [2]. For microchannel devices on commercial MEAs, a small drop (~5 μL; 10,600 cortical neurons/μL, ~50,000 cells per device) was placed into just one out of four reservoirs. On *polyMEA*s, about 100,000 cells were plated onto their central electrode area. Cells were allowed to settle for 30 min in a cell culture incubator (5 % CO_2, 37 °C, 95 % RH) before adding 1 mL of serum-free medium (Neurobasal medium, B27 2 %, Glutamax 1 %, penicillin/streptomycin 1 %). Cultures were protected by a PDMS cap against evaporation and contamination [13] and stored in the incubator. Every week, 450 μL of media was exchanged with fresh warm media. Cultures were imaged once a week on an inverted microscope (DMIL, Leica Microsystems) equipped with a 5 MP camera (DFC420C, Leica Microsystems).

2.5 Electrophysiology

Extracellular signals were recorded with a 60-channel filter-amplifier (MEA60-Up, Multi Channel Systems), featuring a built-in thermal sensor and heating element.

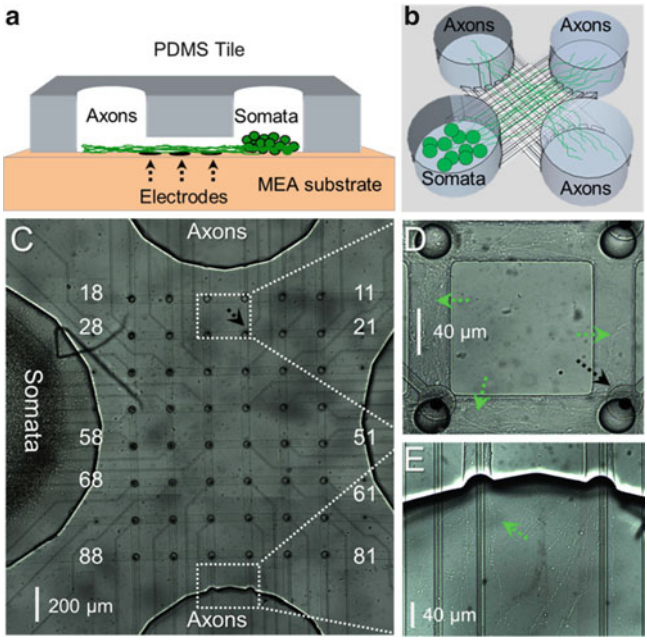

Fig. 2 PDMS microchannel tiles on MEAs for neural network compartmentalization. (**a**) A schematic cross-section of a microchannel and the reservoirs shows how microchannels selectively let axons grow on top of an electrode row while preventing cell bodies to enter. (**b**) PDMS microstructure including four big reservoirs interconnected by an 8×8 matrix of channels. (**c**) Cells seeded in a somal compartment (*left*) had grown their axons after 9 DIV through the entire length of a microchannel into the empty axonal compartment. (**d**) Magnified view of the axons inside the channels between electrodes 15-14 and 25-24. (**e**) Magnified view of axons entering the axonal compartment. *Black arrows* indicate an electrode and *green arrows* point at axons

For microchannel tiles, acquired activity (MC_Rack, Multi Channel Systems) was filtered and analyzed offline. The low frequency noise, which was augmented by the microchannels, was removed by a second-order Bessel high-pass filter (cut-off at 200 Hz). Spikes were detected in the filtered data stream by passing a negative threshold set to –4.5 StDev of the peak-to-peak noise. Only downward threshold-crossings were analyzed.

2.6 Statistical Analysis

Spike trains from microchannel tile recordings were transformed to timestamps (NeuroExplorer, Nex Technologies) for mean frequency and burst analysis. Individual units on each electrode were detected by k-means clustering (Offline Sorter, Plexon). Thereafter, sorted units were checked visually to merge the same units

or exclude unsorted rare signals from analysis. Numerical results were further analyzed by a one-way repeated measures analysis of variance (ANOVA) or a two-way ANOVA, followed by a Bonferroni post-test for all groups (Prism, GraphPad). A probability of $p < 0.05$ was considered significant. Data are expressed as mean ± SEM or as quartiles (Whisker-bars) with maximum and minimum values.

3 Results

3.1 Recording Activity from Microchannel-Confined Axons

Cells started to grow their neurites into the microchannels after 3 DIV. After 9 DIV, axons had almost passed through the entire channel and entered into one of the three axonal compartments (Fig. 2). The neuronal tissue mass inside the channels was increasing up to 27 DIV. Afterward, neural tissue inside the channels and the axonal compartments started to degenerate and thick axonal bundles appeared (Fig. 8c).

Because the microchannels were aligned with the electrodes, axons were forced to grow over the electrodes. The small microchannel cross sections (40 μm × 5 μm) increased the electrical resistance to ground, thereby amplifying the weak extracellular axonal signals. At 9 DIV, first signals could be recorded. They were similar in shape to random networks, but had higher amplitudes (>100 μV; Fig. 3a). The

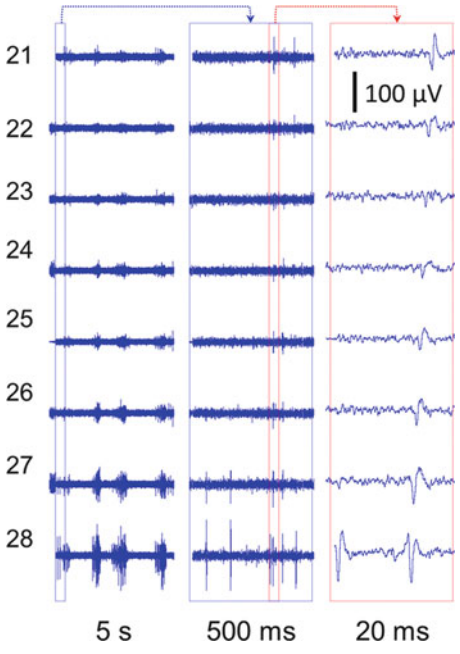

Fig. 3 Sample recording from electrodes in channel 2 at 30 DIV. The *right panel* shows the magnified propagating signal along the full length of the channel from electrode 28 toward electrode 21 (see Fig. 2c)

signal amplitudes increased up to 600 μV after 20 DIV (Fig. 3b). The microchannels not only allowed to record from axons, but also forced the same axon to pass over or nearby all electrodes in one row of the electrode array (Fig. 2c; *e.g.,* electrodes 28 to 21). This made it possible to record from the same axon at its different lengths. Therefore, the same signal appeared with short delay on subsequent electrodes as it propagated along the axon (Fig. 3).

Compared to the diameter of an axon (~1 μm), the width of a microchannel was sufficiently large (40 μm) to let different axonal branches from the same network enter into it. Therefore, every electrode inside the microchannel could simultaneously record from different axons. Signals were sorted by shape to distinguish between the different axons (sources) (Fig. 4a–c). In general, two main signal categories were detected inside the microchannels; monophasic signals (mainly with negative wave) and biphasic signals (mainly with a negative followed by a positive wave). In contrast to quickly decaying biphasic signals, monophasic

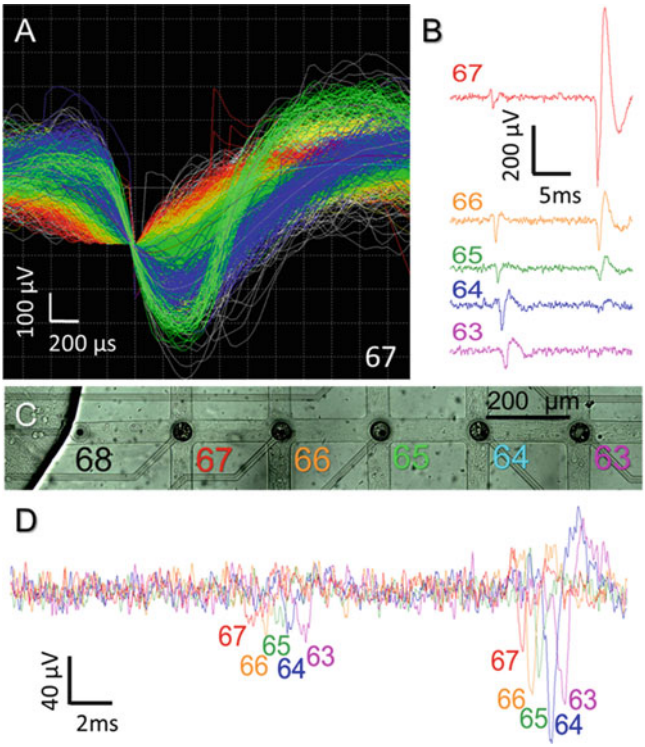

Fig. 4 Signals with different amplitudes and shapes were propagating in channels. (**a**) Signal sorting for electrode 67 shows five different waveforms that were recorded by this electrode. (**b**) Shape and propagation length of monophasic and biphasic signals in channel 6 from electrode 67 to 63. (**c**, **d**) Overlaid signals recorded from electrodes 67 to 63 show the propagation delays for a signal traveling within an axon over sequential electrodes

signals could propagate to distant electrodes inside a microchannel. This feature was amplitude-independent (Fig. 4b). Overlaying the signals recorded from subsequent electrodes inside the same channel showed the propagation delay and how the signal shape varied with location (Fig. 4c).

To analyze the network activity evolution and the propagation velocity along the axons inside the microchannels over time, the electrical activity at 10, 20, 30 and 53 DIV was compared. To evaluate how activity levels change over time or along channels, two subsequent electrodes in a channel were considered as one segment, thereby dividing every channel into the following four segments: Seg 1 (0–250 μm), Seg 2 (250–650 μm), Seg 3 (650–1,050 μm) and Seg 4 (1,050–1,300 μm) (Fig. 5a). Because the amplifiers for electrodes 27, 52 and 62 were switched off at 10 and 20 DIV, data for the respective segments was collected on these two days from one electrode only. A comparison of the overall number of spikes per minute in the proximal segments of all considered channels with that of their distal segments showed that the signal frequency decreases along the channel for all recording days ($p < 0.001$ at 10 and 30 DIV, $p < 0.01$ at 20 DIV; Fig. 5b). Monitoring the mean signal frequency in each segment over time (Fig. 4c) showed a significant decrease at 53 DIV compared to 10 DIV in segments 1, 2 and 3 ($p < 0.05$).

Signal frequencies and propagation velocities were evaluated in detail for three selected channels (channel 2 (electrodes 21–28), 5 (electrodes 51–58) and 6 (electrodes 61–68)). The mean signal frequency for each channel was calculated by averaging all recorded signals from any of the electrodes inside a single channel. The mean signal frequency for each channel tended to decrease over time. This decrease was significant between 10 DIV and the subsequent DIVs for channel 5 ($p < 0.05$ vs. 20 and 30 DIV, and $p < 0.001$ vs. 53 DIV; Fig. 6a) and channel 6 ($p < 0.05$ vs. 30 DIV and $p < 0.01$ vs. 53 DIV; Fig. 5a). The propagation velocity was calculated by dividing the constant distance between a pair of electrodes (200 μm) by the temporal delay of the signal appearance on two subsequent electrodes. The mean propagation velocity for each channel was calculated by averaging the propagation velocities of all subsequent electrode pairs in a channel. For electrodes from which no signals were acquired in 10 and 20 DIV (electrodes 27, 52 and 62), the average velocity was calculated for the two nearest electrodes (channel 2; electrodes 28 and 26, and channel 6; electrodes 63 and 61). The mean propagation velocity tended to increase with culture age, which was contrary to the observed decrease in the spike frequency (Fig. 6a, b). Propagation velocity clearly increased with respect to 10 DIV in channel 2 ($p < 0.001$ vs. 20 DIV and $p < 0.01$ vs. 53 DIV; Fig. 6b), channel 5 ($p < 0.05$, $p < 0.001$ and $p < 0.001$ vs. 20, 30 and 53 DIV, respectively; Fig. 6b) and channel 6 ($p < 0.001$ vs. 20, 30 and 53 DIV; Fig. 6b). This increase was also significant when compared between 20 DIV and the subsequent recording days at 30 and 53 DIV in all channels ($p < 0.001$; Fig. 6b).

In addition to determining the mean propagation velocity, the changes in the propagation velocity along the axon was calculated by comparing the velocity propagation between subsequent electrode pairs (Fig. 7). In channel 5, only few signals propagated along the entire length of the channel at 10, 20 and 53 DIV. Therefore, these DIVs were excluded from the analysis. Despite variations in the

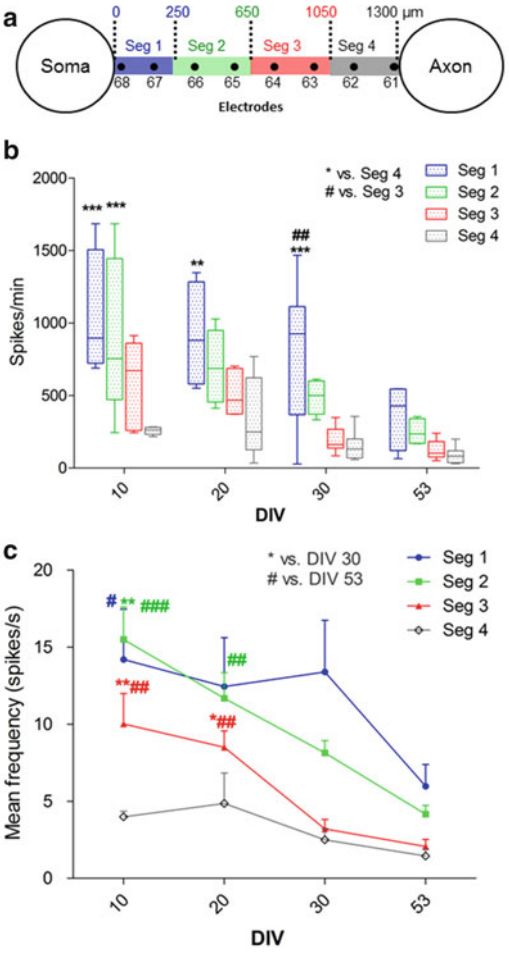

Fig. 5 The spike frequency decreased along a channel and over time. (**a**) Each microchannel was divided into four sections for a spike frequency analysis in the following way: segment 1 (Seg 1 = 250 µm from channel entrance), Seg 2 (250–650 µm), Seg 3 (650–1,050 µm), Seg 4 (1,050–1,300 µm). Each segment represents data that was collected from two adjacent electrodes. (**b**) Spike frequency along the channel. Each *bar* represents the spike frequency range in one segment (*color*) on the mentioned day. The mean spike frequency was calculated by averaging the number of spikes per minute in a selected segment of channels 2, 5 and 6. A two-way ANOVA was applied for comparing the mean values between different segments on the mentioned day. * vs. Seg 4 and # vs. Seg 3 at the same DIV. (**c**) Spike frequency evolution over time. Each line represents the changes in the mean spike frequency of the same segment (averaged over three channels) at different days. A one-way repeated measures ANOVA was applied for analyzing the mean frequency between different DIVs in each segment. * vs. DIV 30 and # vs. DIV 53 of the same segment. * or #$p < 0.05$, ** or ##$p < 0.01$ and *** or ###$p < 0.001$

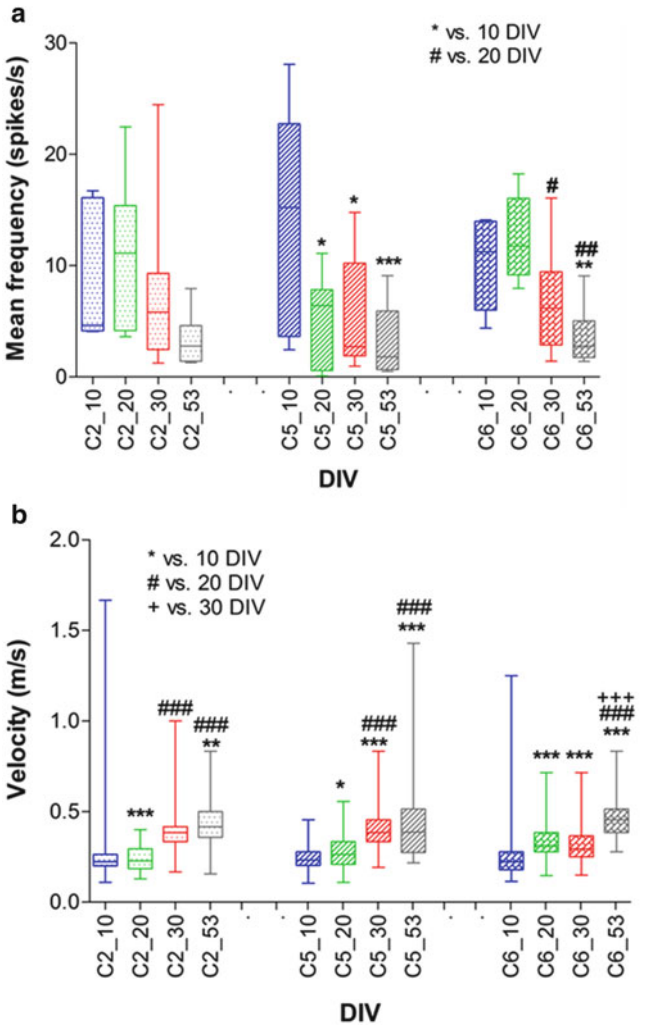

Fig. 6 Different profiles for spike frequency and propagation velocity in three evaluated channels over time. (**a**) Each *bar* represents the range of spike frequencies in one channel on the mentioned day. *x*-axis denominators code for the channel number followed by the DIV on which the recording was performed. One-way repeated measures ANOVA applied for analyzing the mean frequency between different DIVs in each channel. * vs. DIV 10 and # vs. DIV 20 in same channel. (**b**) Mean propagation speed in each channel for a given DIV. After calculating the velocity between each electrode pair in a channel, the mean propagation speed was determined by averaging the velocities of all pairs. Each *bar* represents the range of propagation speed in one channel at the mentioned day. One-way repeated measures ANOVA applied for analyzing the mean velocity between different DIVs in each channel. * vs. DIV 10, # vs. DIV 20 and + vs. DIV 30 in same channel. * or #$p < 0.05$, ** or ##$p < 0.01$ and ***, ### and +++$p < 0.001$. Electrodes 27, 52 and 62 did not record any spikes at 10 and 20 DIV. Therefore, the velocity was estimated by dividing the time delay between two nearby electrodes by a distance of 400 μm

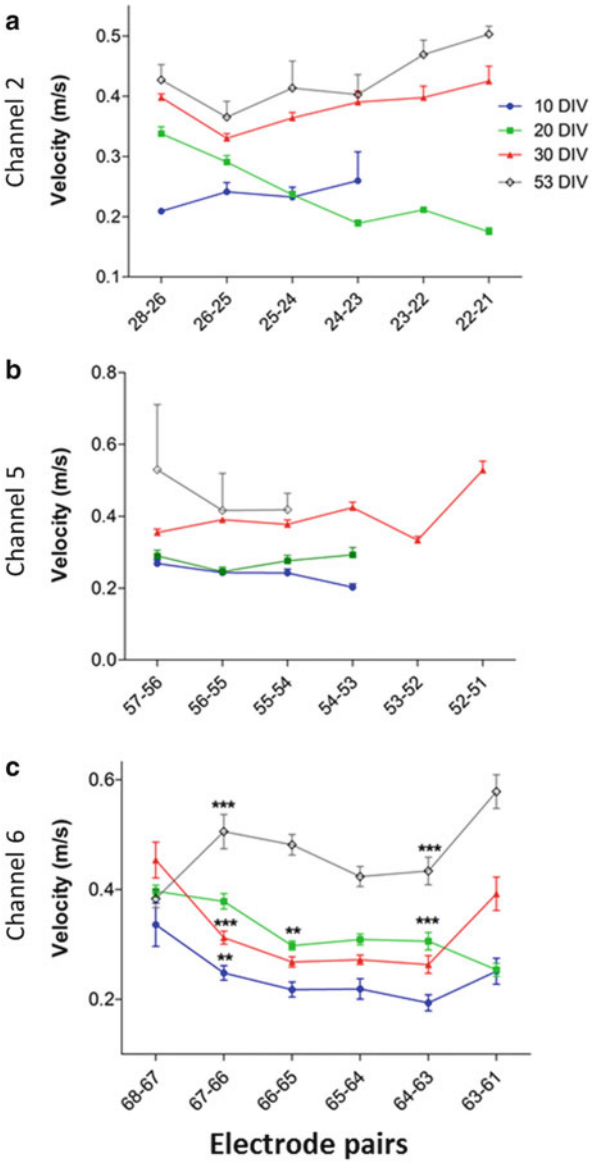

Fig. 7 Changes in the signal propagation velocity along the axon in different channels. The propagation velocity was calculated by dividing the constant distance between each electrode pair by the temporal delay between time stamps. (**a**, **b**) In channels 2 and 5: no significant differences in the propagation velocity between two subsequent electrode pairs could be detected. (**c**) In channel 6, however, the velocity decreased or increased significantly along the axon at different days. One-way repeated measures ANOVA was applied for analyzing the mean propagation velocity between two subsequent electrode pairs at the mentioned day. $*p < 0.05$, $**p < 0.01$ and $***p < 0.001$ vs. mean propagation speed between previous electrode pairs. For all channels, the propagation speed was calculated for 30 randomly selected propagating signals at different time points during the recording window (1 min)

propagation velocities along channels 2 and 5, they were not significant between two adjacent segments on any of the recording DIVs (Fig. 7a, b). However, in channel 6, significant changes in the propagation velocity were observed between different segments, which could either decrease (*e.g.*, $p < 0.001$ from 68-67 to 67-66 at 30 DIV; Fig. 7c) or increase (*e.g.*, $p < 0.001$ from 68-67 to 67-66 at 53 DIV; Fig. 7c). Besides the local fluctuations in velocity, an increase in velocity over time is clearly evident for all channels in Fig. 7.

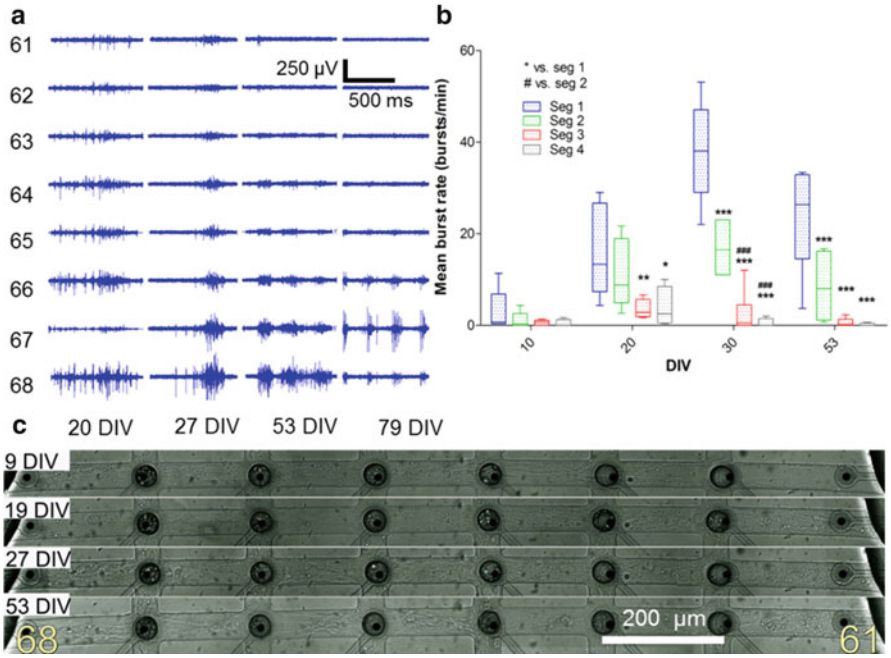

Fig. 8 Burst propagation along channels. (**a**) Raw signals from channel 6 (electrodes 68-61) at different DIVs. (**b**) Mean burst frequency in different segments of three channels. After burst detection, the burst frequency was calculated for each channel segment of channels 2, 5 and 6, and then averaged for all three channels. Each *bar* represents the burst frequency range in one segment of all three channels. Two-way ANOVA applied for analyzing the mean burst rate between two segments of the same channel at the mentioned day. * vs. seg 1 and # vs. seg 2. $^{*}p < 0.05$, $^{**}p < 0.01$ and *** or $^{\#\#\#}p < 0.001$. (**c**) Changes in morphology along channel 6 (electrodes 68–61) over 53 DIV

Bursts propagation was analyzed for channels 2, 5 and 6 using the following criteria in NeuroExplorer: maximal interval to start burst = 0.02 s, maximal interval to end burst = 0.01 s, minimal interval between bursts = 0.01 s, minimal duration of burst = 0.02 s, minimal number of spikes in burst = 4, and bin size = 1 s). Figure 8 summarizes the mean burst rate in different segments of channels 2, 5 and 6. At 10 DIV, only a few bursts were detected (Fig. 8b). The burst frequency (bursts/min) increased over time and reached its maximum value after 30 DIV (Fig. 8b). A burst rate analysis for each segment of these three channels showed that bursts faded after 400-600 µm propagation length within a channel (Fig. 8b). The burst rate in segments 3 and 4 was significantly lower than in segment 1 ($p < 0.01$ and $p < 0.05$ at 20 DIV, $p < 0.001$ at 30 DIV, and $p < 0.001$ at 53 DIV; Fig. 8b).

3.2 *polyMEA Features and Device Characteristics*

Most deep brain implants are designed to record from biological tissue at near cellular resolution. This requires the electrode diameters to be on a similar scale. The design considerations for the implantable polymer microelectrode arrays included: (1) compatibility to commercial or custom-made signal processing electronics; (2) preferably a seamless, flexible and stable connection between implanted electrodes and the electronic platform; (3) an insertion depth control that may be defined by the probe geometry and guidance features (e.g., shaft edges, stoppers, . . .).

Once geometries and boundary conditions are defined, photomasks can be designed by any microelectromechanical systems (MEMS) layout editor (*e.g.*, Expert, Silvaco; CleWin, WieWeb). Exemplarily, five different *polyMEA* designs for different brain areas are depicted in Fig. 9. Overall device features and the connecting scheme for a low-density electrode *polyMEA* are shown in Fig. 10. Its feature sizes are summarized in Table 1.

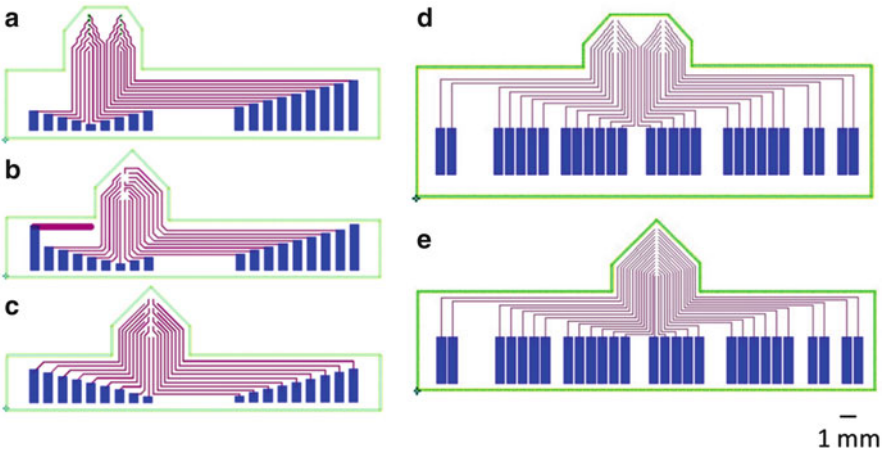

Fig. 9 Five *polyMEA* design examples for recording from various brain areas. The number of electrodes is the same in **a**–**c** (18) and in **d**, **e** (28). Design B with two separate electrode fields is suitable for the local recording at two specific depths while designs **a**, **c**, **d** and **e** are universal probes with equal electrode pitches along their insertion shafts. The sharpened probe tips in designs **b**, **c** and **e** may facilitate probe insertion into the brain. Electrode pitch and diameter, wire widths and pitches are different in these designs

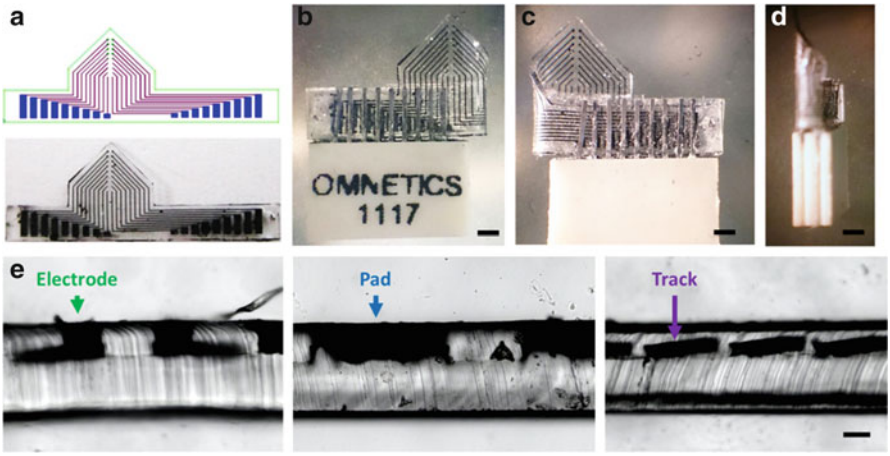

Fig. 10 Overall device layout and connecting scheme for an *in vivo polyMEA* with 2 × 9 electrode array. (**a**) CAD design and resulting device with tracks and electrodes made from a conductive polymer composite; pad width: 414 μm. (**b–d**) *polyMEA* squeeze-clamped between an Omnetics (A79006-001) 0.757 mm pitch, double-row pin connector (*front, back* and *side*). In this case, no extra PDMS sealing coat was applied to the connector and the *polyMEA* yet. (**e**) Cross section views of the *polyMEA* electrodes (*left*), pads (*middle*) and buried tracks (*right*). Scale bars: 1 mm (**b–d**), 100 μm (**e**)

Table 1 Feature sizes of a universal *in vivo polyMEA* with 2 × 9 electrode array

Parameter	Size (μm)
Maximum electrode site diameter	130
Minimum electrode site diameter	50
Vertical electrode center-to-center pitch	300
Horizontal electrode center-to-center pitch	300
Vertical electrode array dimension (center-to-center)	2,400
Shaft width	5,370
Shaft thickness	280.6
Shaft length	3,920
Track width	50

3.3 Electrical Characteristics of Carbon-, Graphite-, PEDOT:PSS-in-PDMS Composite Electrodes

In the *in vivo polyMEA* featuring a 2 × 9 electrode array, all 18 microelectrodes were functional. The average and extreme electrode impedance distribution between 1 Hz and 100 kHz is depicted in Fig. 11. Impedances ranged between 5 MΩ at low frequencies and several hundred kΩ at 1 kHz. Electrodes had almost resistive character at 1 kHz.

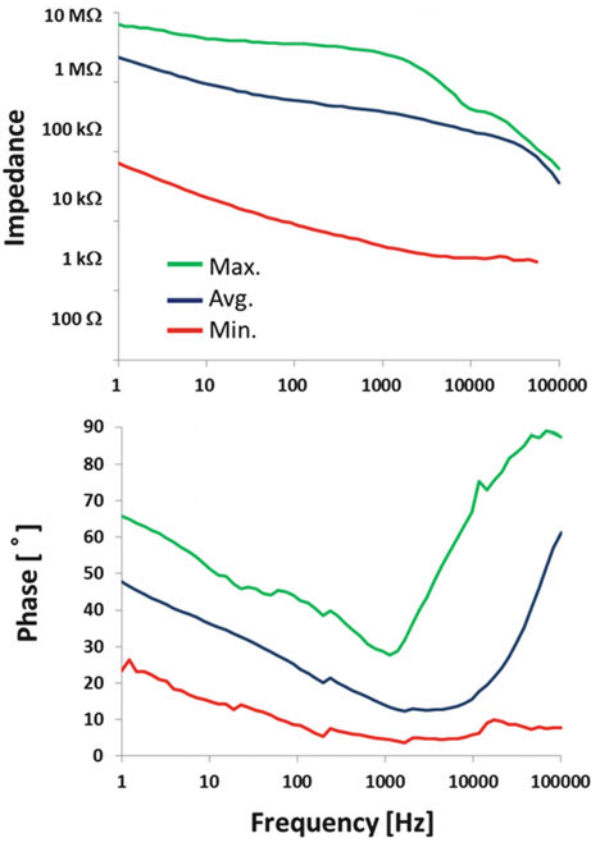

Fig. 11 Impedance characteristics of a *polyMEA* with a 2 × 9 electrode array. Electrode diameters ranged from 50 to 130 μm by 10 μm increments. Comparison of the average (Avg.) and extreme (Min., Max.) electrode impedances in a Bode magnitude plot (*top*) and of their capacitive-resistive characteristics in a phase plot (*bottom*)

4 Discussion

The presented examples demonstrated how a straightforward replica-molding process for PDMS sheets generates perforated microchannel scaffolds for diverse applications. We exemplarily discussed their *in vitro* use in axonal guidance and regeneration studies on microelectrode arrays (MEAs) and the production of tissue-conformal *in vivo* MEAs for neuroprosthetic applications.

4.1 PDMS Microchannels for Axon Guidance and Electrophysiology

We showed that axons can be easily guided in microchannels that were aligned on top of the recording electrodes of a MEA. This allowed the detailed evaluation of axonal morphology, the different types of activity and their propagation velocity along channels over time.

We found that the signal frequency decreased between proximal and distal segments of a microchannel. This could have two reasons: the signal could be fading along the channel as it was evident in most cases (Fig. 3b). Furthermore, axons may leave the straight path by changing their growth direction at the channel crossing points (Fig. 2b).

The effect of microchannel geometry on signal quality has been evaluated by Wang *et al.* [11]. They showed that in microchannels with lengths between 200 and 3,000 μm the signal amplitude decreases along the channel length. Therefore, signals could become too small to be detected by electrodes in distal sections. In accordance with Fig. 3, large amplitude signals in proximal sections (electrode 68) decreased as they propagated within the channel. In line with the findings by Wang *et al.* [11], the high microchannel resistance combined with its stray capacitance acted like a first-order low-pass filter that attenuate high frequency signal amplitudes (i.e., the negative peaks of an action potential). Equally, the channel cross-section can affect signal properties [11]. Although all microchannels had the same cross-section, the number of axons and the thickness of the axon bundles inside the microchannel varied with channel depth and over time, thereby changing the total cross-section of a microchannel at different channel locations. In 2009, Dworak and Wheeler showed that the growth of neurites inside microchannels ($750 \times 10 \times 3$ μm^3) increased the resistivity from 75 Ω cm of empty channels to 300 Ω cm for microchannels filled with neural tissue due to an effective decrease of the channel cross-section [10].

The increase of neural tissue mass inside the microchannels between 20 and 30 DIVs (Fig. 8c) could be correlated with an increased spike frequency for almost all channels and all channel segments (Figs. 5 and 6). Equally, a decrease in neural tissue density after 53 DIV led to a decrease in the firing frequency in all channels (Figs. 5 and 6). A significant decrease of the signal frequency after 30 DIV in all segments could be related to the axonal degeneration and the formation of axonal bundles (Fig. 8c).

Recording an action potential from subsequent electrodes along a microchannel enabled us to determine the propagation velocity and direction. The propagation velocities varied between 0.1 to 2.5 m/s, which is in same range as previously reported by Pan *et al.* (0.18–1.14 m s^{-1} in unmyelinated axons) [14]. In this study, we also evaluated changes in the propagation velocities in different segments of the same channel as well as in the same segment or channel over time. Changes in action potential velocity along the axon could be related to changes in thickness and curvature along the axon. We also observed an increased propagation velocity in all channels between 30 and 53 DIVs, which could possibly be related to increased axonal diameters or the fasciculation of axons. Such spatial and temporal changes in stimulus-driven action potential propagation velocity have been reported recently by Bakkum *et al.,* however in random cultures on dense microelectrode arrays [15]. In the present study, we evaluated the propagation velocity of signals derived from spontaneous network activity over time.

Bursts are spike flares within a short time window. Bursts are usually recorded simultaneously from different MEA electrodes, which shows that burst activity

involves and propagates within large parts of the network [16]. We also evaluated how bursts propagate inside the microchannels. While individual monophasic spikes are able to propagate over long distances within a channel, bursts failed in reaching the microchannel endings in most cases (Fig. 8a). A significant difference in burst frequency on electrodes in proximal and distal parts of the microchannels confirmed the observed burst propagation fading along the microchannel (Fig. 8b). Because bursts are composed of individual spikes with different shapes, each of them will have its specific half-life for traveling along the channel. Fading spikes inside a burst will cause the burst to disintegrate along the channel. In consequence, a spike sequence that was categorized as a burst at the proximal end of a channel may not be recognized as a burst anymore at the distal end of a channel. Another mechanism for burst fading could be based on a phase cancelation effect. Signals with different shapes and phases can cancel each other out while traveling along the channel [11].

4.2 PDMS Microchannels for the Production of Tissue-Conformal in vivo MEAs for Neuroprosthetic Applications

Compared to stiff implants, flexible probes will more easily relieve the strain caused by micromotion forces that result from the relative displacement between the implant and the brain tissue. This may minimize chronic tissue damage or inflammation due to a better match in the stiffness of the probe and the brain microenvironment [17]. In this context, PDMS has potential as a scaffold material for neural interfaces [18, 19]. As thin sheets it can follow the curvature of a tissue and provide a uniform and tight contact [20]. Here, we exemplarily depicted the design and fabrication of a flexible *polyMEA* with 18 recording sites that can be implanted into the brain tissue. Impedance characteristics indicated that the electrodes performed well even in the low frequency range. At 1 kHz, their average impedance stayed at several hundred kΩ with an almost resistive behavior.

Acknowledgements Many thanks to Marina Nanni, Francesca Succol and Claudia Chiabrera for their excellent assistance in cell culture preparation. Thanks to Francesco Difato and Mattia Pesce for their advice on imaging techniques. Intramural funding is highly appreciated.

References

1. Taylor AM, Blurton-Jones M, Rhee SW, et al. A microfluidic culture platform for CNS axonal injury, regeneration and transport. Nat Methods. 2005;2:599–605.
2. Banker G, Goslin K. Culturing nerve cells. Cambridge: MIT Press; 1998.
3. Kim HJ, Park JW, Byun JH, et al. Quantitative analysis of axonal transport by using compartmentalized and surface micropatterned culture of neurons. ACS Chem Neurosci. 2012;3:433–8.

4. Kim YT, Karthikeyan K, Chirvi S, et al. Neuro-optical microfluidic platform to study injury and regeneration of single axons. Lab Chip. 2009;9:2576–81.
5. Park J, Koito H, Li J, et al. Microfluidic compartmentalized co-culture platform for CNS axon myelination research. Biomed Microdevices. 2009;11:1145–53.
6. Yang IH, Gary D, Malone M, et al. Axon myelination and electrical stimulation in a microfluidic, compartmentalized cell culture platform. Neuromolecular Med. 2012;14:112–8.
7. Wheeler BC, Brewer GJ. Designing neural networks in culture. Proc IEEE. 2010;98:398–406.
8. Claverol-Tinture E, Ghirardi M, Fiumara F, et al. Multielectrode arrays with elastomeric microstructured overlays for extracellular recordings from patterned neurons. J Neural Eng. 2005;2:L1–7.
9. Ravula SK, Mcclain MA, Wang MS, et al. A multielectrode microcompartment culture platform for studying signal transduction in the nervous system. Lab Chip. 2006;6:1530–6.
10. Dworak BJ, Wheeler BC. Novel MEA platform with PDMS microtunnels enables the detection of action potential propagation from isolated axons in culture. Lab Chip. 2009;9:404–10.
11. Wang L, Riss M, Buitrago JO, et al. Biophysics of microchannel-enabled neuron-electrode interfaces. J Neural Eng. 2012;9:026010.
12. Blau A, Murr A, Wolff S, et al. Flexible, all-polymer microelectrode arrays for the capture of cardiac and neuronal signals. Biomaterials. 2011;32:1778–86.
13. Blau A, Neumann T, Ziegler C, et al. Replica-moulded polydimethylsiloxane culture vessel lids attenuate osmotic drift in long-term cell cultures. J Biosci. 2009;34:59–69.
14. Pan LB, Alagapan S, Franca E, et al. Propagation of action potential activity in a predefined microtunnel neural network. J Neural Eng. 2011;8.
15. Bakkum DJ, Frey U, Radivojevic M, et al. Tracking axonal action potential propagation on a high-density microelectrode array across hundreds of sites. Nat Commun. 2013;4:2181.
16. Maeda E, Robinson HP, Kawana A. The mechanisms of generation and propagation of synchronized bursting in developing networks of cortical neurons. J Neurosci. 1995;15: 6834–45.
17. Subbaroyan J, Kipke DR. The role of flexible polymer interconnects in chronic tissue response induced by intracortical microelectrodes—a modeling and an in vivo study. Conf Proc IEEE Eng Med Biol Soc. 2006;1:3588–91.
18. Lacour S, Benmerah S, Tarte E, et al. Flexible and stretchable micro-electrodes for in vitro and in vivo neural interfaces. Med Biol Eng Comput. 2010;48:945–54.
19. Maghribi M, Hamilton J, Polla D et al. (2002) Stretchable micro-electrode array. In: Microtechnologies in medicine & biology 2nd annual international IEEE-EMB special topic conference, p 80–83
20. Guo L, Meacham KW, Hochman S, et al. A PDMS-based conical-well microelectrode array for surface stimulation and recording of neural tissues. IEEE Trans Biomed Eng. 2010;57: 2485–94.
21. Anderson JR, Chiu DT, Jackman RJ, et al. Fabrication of topologically complex three-dimensional microfluidic systems in PDMS by rapid prototyping. Anal Chem. 2000;72: 3158–64.
22. Bettinger CJ, Borenstein JT. Biomaterials-based microfluidics for engineered tissue constructs. Soft Matter. 2010;6:4999–5015.
23. Qin D, Xia Y, Whitesides GM. Soft lithography for micro- and nanoscale patterning. Nat Protoc. 2010;5:491–502.
24. Yun K-S, Yoon E. Fabrication of complex multilevel microchannels in PDMS by using three-dimensional photoresist masters. Lab Chip. 2008;8:245–50.

Brain-Controlled Selection of Objects Combined with Autonomous Robotic Grasping

Christoph Reichert, Matthias Kennel, Rudolf Kruse, Hans-Jochen Heinze, Ulrich Schmucker, Hermann Hinrichs, and Jochem W. Rieger

Abstract A Brain–Computer Interface (BCI) could help to restore mobility of severely paralyzed patients, for instance by prosthesis control. However, the currently achievable information transfer rate of noninvasive BCIs is insufficient to control complex prostheses continuously in many degrees of freedom. In this paper we present an autonomous system for grasping natural objects that compensates the low information flow from noninvasive BCIs. Using this system, one out of several objects can be grasped without any muscle activity. Rather, the grasp is initiated by decoded voluntary brain wave modulations. Object selection and grasping are performed in a virtual reality environment. A universal grasp planning algorithm calculates the trajectory of a gripper online. The system can be controlled after less

C. Reichert
Department of Neurology, University Medical Center A.ö.R., Magdeburg, Germany

Department of Knowledge and Language Processing, Otto-von-Guericke University, Magdeburg, Germany
e-mail: christoph.reichert@med.ovgu.de

M. Kennel • U. Schmucker
Fraunhofer Institute for Factory Operation and Automation IFF, Magdeburg, Germany
e-mail: matthias.kennel@iff.fraunhofer.de; klaus-ulrich.schmucker@iff.fraunhofer.de

R. Kruse
Department of Knowledge and Language Processing, Otto-von-Guericke University, Magdeburg, Germany
e-mail: kruse@iws.cs.uni-magdeburg.de

H.-J. Heinze • H. Hinrichs
Department of Neurology, University Medical Center A.ö.R., Magdeburg, Germany

Leibniz Institute for Neurobiology, Magdeburg, Germany

German Center for Neurodegenerative Diseases (DZNE), Magdeburg, Germany
e-mail: hans-jochen.heinze@med.ovgu.de; hermann.hinrichs@med.ovgu.de

J.W. Rieger (✉)
Department of Applied Neurocognitive Psychology, Carl-von-Ossietzky University, Oldenburg, Germany
e-mail: jochem.rieger@uni-oldenburg.de

A.R. Londral et al. (eds.), *Neurotechnology, Electronics, and Informatics*,
Springer Series in Computational Neuroscience 13, DOI 10.1007/978-3-319-15997-3_5

than 10 min of training. We found that decoding accuracy increases over time and that an increased sense of agency achieved by permitting free selections renders the system to work most reliably.

Keywords Brain–computer interface (BCI) • P300 • Oddball paradigm • Grasp robot • Magnetoencephalogram (MEG) • Virtual reality (VR) • Gaze independence

1 Introduction

Brain–Computer Interfaces (BCI) can serve as a communication channel between the human brain and a computational or robotic device by translating human brain activity to machine commands [1]. Due to the independence from muscles and peripheral nerves they are in the focus of research to replace motor functions of severely paralyzed patients. In the recent years, highly invasive techniques were applied to control prosthetic devices by voluntary modulation of brain activity [2, 3]. In humans, the use of noninvasive techniques, like the electroencephalogram (EEG), is preferable over invasive recordings. However, only a small number of commands can be discriminated with noninvasively assessed brain activity and, as a consequence, noninvasive systems do not allow for full control of complex manipulators with many degrees of freedom. Here we report progress in our development of a noninvasive BCI that enables users to grasp natural objects with a complex manipulator. Our approach combines the development of both efficient brain decoding techniques and autonomous actuator control to overcome the limited information transfer from noninvasive BCIs.

A commonly used control signal for movement related BCIs is the so-called μ-rhythm [4], which can be measured during motor imagery. However, a considerable percentage of people are unable to control motor imagery BCIs [5, 6]. In contrast, it was shown that a larger fraction of people is able to select items in speller paradigms using an oddball task [7]. The widely used matrix speller, which relies on the oddball task, was first introduced by Farwell and Donchin [8]. In this paradigm a P300, a positive EEG deflection, is evoked when a rare target stimulus appears in a series of irrelevant stimuli. While it is often assumed that the accuracy of visually stimulated P300 speller is independent of gaze direction, it has recently been shown that the performance of the matrix speller drops significantly if the eyes are not moved toward the target [9]. The reason is that two EEG components, the P300 and the N200, contribute information when the centre of regard is moved to the target [10], whereas only the P300 is present if the eyes don't move. This could render the P300 paradigm less useful for patients who cannot move their eyes.

In this work we demonstrate that the visual oddball paradigm can be successfully applied to initiate targeted grasps in a visually complex virtual environment with multiple realistic objects. Importantly, we show that the paradigm developed here works independent of the user's ability to direct gaze towards the target object. This is of high relevance for the targeted user group.

The development of an efficient noninvasive brain decoder is complemented by the development of a robotic manipulator with the ability to manipulate in an intelligent and autonomous way predefined objects. Here we propose a new analytical grasp planning algorithm to achieve autonomous grasping of arbitrary objects. In contrast to other motion planning algorithms, our algorithm is not based on Learning by Demonstration (for a review see [11]) and involves, but is not limited to, the robot's kinematics.

2 Materials and Methods

2.1 General Procedure

In this study we decoded in real-time the magnetoencephalogram (MEG) of 17 subjects (9 male, 8 female, mean age: 26.6 years) to determine their intention to select one of six selectable realistic objects for grasping. We used the decoding results to initiate a grasp of a robotic gripper. All subjects gave written informed consent. The study was approved by the ethics committee of the Medical Faculty of the Otto-von-Guericke University of Magdeburg.

2.2 Virtual Environment

We presented six objects placed at fixed positions in a virtual reality environment as shown in Fig. 1. The visual angle between outmost left and right objects was 8.5°. We used circular regions around the objects on the table to provide cue flashes for the P300 paradigm and to provide feedback by coloring the region's shape. A photo transistor placed on the screen was used to synchronize the ongoing MEG with the events displayed on the screen. To provide realistic feedback, the model of a robot (Mitsubishi RV E2) equipped with a three finger gripper (Schunk SDH) was part of the scene. The robot in the virtual reality scene visualized the autonomously calculated grasp to the selected object mimicking the movements of the real robot.

2.3 Paradigm

The oddball paradigm we employed is designed to elicit a P300 potential which is a deflection of sensor values evoked approximately 300 ms after a rare target stimulus occurs in a series of irrelevant stimuli. The goal for the brain decoder is to reliably detect the P300 to generate a control signal for the robot. In our variant of the paradigm, we marked objects by flashing their background for 100 ms. Objects

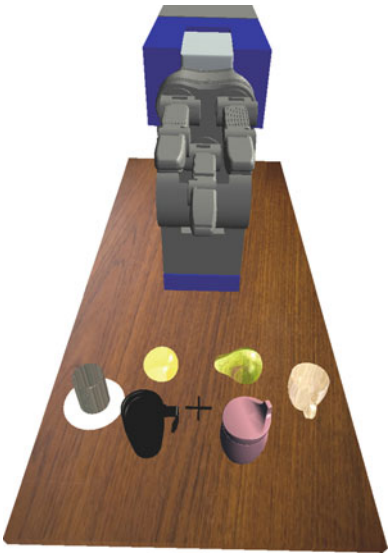

Fig. 1 VR scenario used for visual stimulation. This snapshot shows one flash event of an object

Table 1 Number of runs the subjects performed in different selection modes

	Instructed			
Subject #	Training	Decoder	Free	Grasp
1	2	5	–	–
2	4	4	1	–
3	3	4	–	–
4–6	3	4	1	1
7	2	4	2	1
8	3	3	2	1
9	2	4	2	1
10	2	4	2	–
11	2	4	2	1
12	2	5	2	–
13–17	2	4	2	1

were marked in random order with an interstimulus interval of 300 ms. Each object was marked five times per selection trial resulting in a stimulation interval length of 10 s.

Subjects were instructed to fixate the black cross centred to the objects and to count how often the target object was marked. The counting ensured that attention was maintained on the stimulus stream. In addition, subjects were instructed to avoid eye movements and blinking during the stimulation interval.

Each subject performed a minimum of seven runs with 18 selection trials per run. The runs were performed in three different modes that served different purposes. The number of runs each subject performed in each mode is listed in Table 1. We started with the *instructed selection* mode. In this mode, the target object was cued

by a light grey circle at the beginning of a trial and subjects were instructed to attend the cued object. Instructed selection was used in the initial training runs in which we collected data to train the classifier. In this mode true classifier labels are available which are required to train the classifier. We provided random feedback during training runs because no classifier was available in these initial runs. After the training runs, each subject performed several instructed runs with feedback. We denote the second selection mode *free selection*. In this mode, subjects were free to choose the target object. In instructed selection mode and in free selection mode, a green circle was presented at the end of the trial on the decoded object as feedback. All other objects were marked by red circles. Free selection runs were performed after the instructed selection runs. In the third mode, the *grasp selection* mode, the virtual robot grasped and lifted the decoded target for feedback. Grasp selection runs were performed after free selection runs. In both modes, the free selection and grasp selection mode, the subject said "no" to signal that the classifier decoded the wrong object and did not respond otherwise.

The results reported in this paper arise from online experiments. We did not exclude subjects participating in early sessions, causing slight changes in the experimental protocol during the study (Table 1). The number of runs performed in the different modes depended on cross validated classifier performance estimation and the development of detection accuracy. In total, five subjects performed three, one subject four and the remaining 11 subjects two initial training runs. Two subjects performed only instructed selections. Twelve of the subjects performed one run in the grasp selection mode. Here, only six instead of 18 trials were performed, due to the longer feedback duration.

2.4 Data Acquisition and Processing

The MEG was recorded with a whole-head BTi Magnes 248-sensors system (4D-Neuroimaging, San Diego, CA, USA) at a sampling rate of 678.17 Hz. Simultaneously, the electrooculogram (EOG) was recorded for subsequent inspection of eye movements. MEG data and event channels were instantaneously forwarded to a second workstation capable of processing the data in real-time. The data stream was cut into intervals including only the stimulation sequence. The MEG data were then band-pass filtered between 1 and 12 Hz and down sampled to 32 Hz sampling rate. Then, the stimulation interval was cut in overlapping 1,000 ms segments starting at each flash event. In instructed selection mode, the segments were labelled as target or nontarget segments depending on whether the target or a nontarget object was marked.

We used a linear support vector machine (SVM) as classifier because it proved to reliably provide high performance in single trial MEG discrimination [12, 13]. These previous studies showed that linear SVM is capable of selecting appropriate features in high dimensional MEG feature spaces. We performed classification in the time domain, meaning that we used the magnetic flux measured in 32 time steps

as classifier input. To reduce the dimensionality of the feature space, we excluded 96 sensors located farthest from the vertex (the midline sensor at the position halfway between inion and nasion) which is the expected site of the P300 response. We further reduced the number of sensors by selecting the 64 sensors providing the highest sum of weights per channel in an initial SVM training on all preselected 152 sensors of the training run data. The selected feature set (64 sensors $\times$ 32 samples = 2,048 features) was then used to train the classifier again and retrain the classifier after each run conducted in instructed selection mode.

2.5 Grasping Algorithm

In this section we describe the general procedure of our grasp planning algorithm, whereas we present the mathematical details in the Appendix. The algorithm was developed to physically drive a robot arm, but in this experiment it was used to provide virtual reality feedback. Importantly, in this strategy the robot serves as an intelligent, autonomous actuator and does not drive predefined trajectories. The algorithm assumes that object position and shape coordinates relative to the manipulator are known to the system. In this experiment, coordinates of CAD-modelled objects were used. However, coordinates could as well be generated by a 3D object recognition system.

Central to our approach is that the contact surfaces of the gripper's fingers and the surfaces of the objects were rasterized with virtual point poles. We assumed an imaginary force field between the poles on the manipulator and the poles on the target object (see Appendix for details). The goal of the algorithm is to initially generate a manipulator posture that ensures a force closure grasp. The following grasp is organized by closing the hand in a real world scenario and by locking the object coordinates relative to the finger surface coordinates in the virtual scenario.

3 Results

3.1 Decoder Accuracy

We determined the decoding accuracy as the ratio of correctly decoded objects divided by the total number of object selections. All subjects performed the task reliably above guessing level which was 16.7 % according to the six objects on the table. On average, the intended object selections were correctly decoded from the MEG data in 77.7 % of all trials performed. Single subject accuracies ranged from 55.6 to 92.1 %. In the instructed selection mode the average accuracy was 73.9 and 85.9 % in the free selection mode. A Wilcoxon rank sum test revealed a p-value of 0.03 which indicates that the performance difference between the instructed and

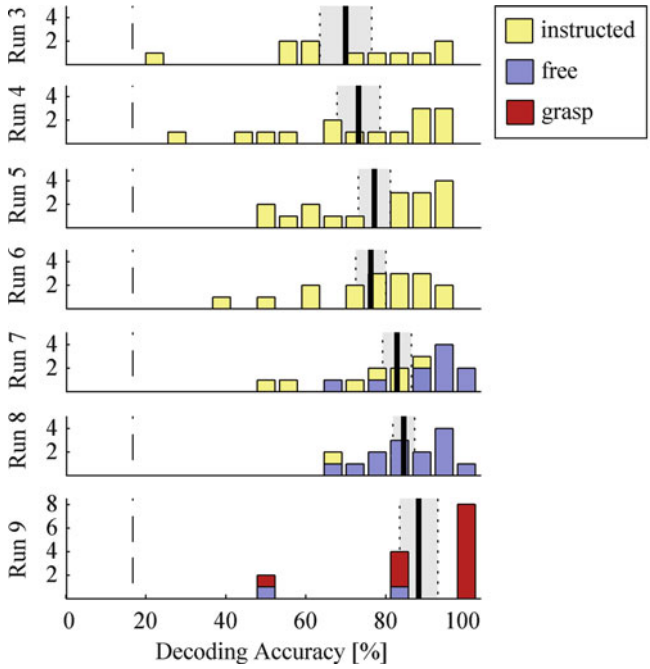

Fig. 2 Performance histograms. The ordinate indicates the number of subjects who achieved the respective decoding performance out of 19 possible percentage bins, equally spaced from 0 to 100 %. The histograms show data from different runs, chronologically ordered from top to bottom. The run modes are coded by color. *Vertical dashed lines* indicate the guessing level and *thick solid lines* indicate the average decoding accuracies over subjects. Standard error is marked *grey*

the free selection mode is statistically significant with higher performance in the free selection mode. When subjects received feedback by moving the virtual robot to the grasp target, the average accuracy was even higher and reached 91.2 %. Figure 2 depicts the evolution of decoding accuracies over runs. The height of the bars indicates the number of subjects (y-axis) who achieved the respective decoding performance out of 19 possible percentage bins. Each histogram shows the results from one run and the performance bins are equally spaced from 0 to 100 %. The histograms are chronologically ordered from top to bottom. Yellow bars indicate results from instructed selection runs, blue bars indicate free selection run results and red bars indicate results in runs with grasp feedback. Vertical dashed lines indicate the guessing level and thick solid lines indicate the average decoding accuracies over subjects whereas the standard error is marked grey. The average decoding accuracy increases gradually over the course of the experiment. Moreover, the histograms show that the highest accuracy over subjects was achieved in free selection runs. Note that our system achieved perfect detection in 8 of the 12 subjects who received virtual grasp feedback. However, only six selections were performed by each subject in these grasp selection runs.

An established measure for the comparison of BCIs is the information transfer rate (ITR) which combines decoding accuracy and number of alternatives to a unique measure. We calculated the ITR according to the method of Wolpaw et al. [14] at 3.4–12.0 bit/min for single subjects and 8.1 bit/min on average. Note that the maximum achievable bit rate with the applied stimulation scheme is 15.5 bit/min.

For online eye movement control, we observed the subjects' eyes on a video screen. In addition, we inspected the EOG measurements offline. Both methods confirmed that subjects followed the instruction to keep fixation.

3.2 Grasping Performance

We evaluated the execution duration of the online grasp calculation for different setups and objects. We implemented our grasping algorithm with the ability to distribute force computations to several parallel threads. Here, we permitted five threads employing a 2.8 GHz AMD Opteron 8220 SE processor. We calculated grasps of the six objects shown in Fig. 1. To assess effects of object position, we arranged the objects at different positions within the limits of our demonstrating robot's work space. Each object was placed once at each of the positions depicted in Fig. 1. The time needed to plan the trajectory and execute the grasp until reaching force closure is listed in Table 2 for each object/position combination. Calculation times ranged from 11 to 72.6 s depending on the object and the position. The diagonal of Table 2 represents the actual object/position setup during our experiment.

The results indicate that the duration of grasp planning depends on many parameters. The most important determinant of execution time is the number of point poles ($O(n^2)$) which depends on the level of detail of the object surface. This is reflected in the high variation of the average calculation time of objects 1–6 over positions (18, 50.3, 12.9, 15.3, 26.1, 39.4 s). The execution times also depend on the physical constraints of the robot and object position. We observed that even minimal differences in object arrangement appear to have strong influence on force closure termination. This is also indicated by different execution times of identical objects at symmetric positions (e.g. left/right). We consider it likely that these differences

Table 2 Duration of grasp planning calculation for all object/position combinations in seconds

	Object #					
Object position	#1	#2	#3	#4	#5	#6
Left	**33.0**	68.5	11.0	14.1	16.0	24.5
Upper left	25.5	**34.0**	16.5	13.5	39.0	46.7
Lower left	11.0	72.6	**11.0**	18.0	22.5	65.0
Upper right	15.5	42.5	15.0	**12.5**	37.0	46.0
Lower right	12.0	48.5	11.0	19.0	**22.5**	24.5
Right	11.0	35.6	13.0	14.5	19.5	**29.5**

Bold numbers indicate the object positions used in the online experiment

are caused by numerical precision issues due to the high number of summations in Eqs. (3) and (4) (see Appendix).

4 Discussion

In the present work we demonstrated that the oddball paradigm is well suited for use in a BCI to reliably select one of several objects for grasping. In a previous study we showed that other selection paradigms also are suitable to select virtual reality objects [15]. The advantage of the present study over the previous study is that the selection of objects was achieved independent from eye movements to the target and realistic grasp feedback was presented. Importantly, our results suggest that performance improves with training and the improvement is even higher when subjects obtain more control by permitting free selections and when realistic visual feedback was presented. This suggests that BCI control in our P300 paradigm is improved with an increase of the subject's sense of agency. A gaze independent BCI based on directing covert attention is a fundamental requirement for patients who cannot easily orient gaze to the target object.

Earlier reports suggested that eye movements greatly improve performance in a P300 speller [9, 10, 16], due to contribution from visual areas to brain wave classification [17]. We extend these previous studies and show that the P300 paradigm is well suited for a gaze independent object grasping BCI. We achieved independence from visual components by instructing our subjects to fixate and by excluding occipital sensors from the analysis. This approach simulates a realistic setting with patients who cannot move their eyes and are therefore dependent on covert attention shift based activation for control. To date, only a small number of studies successfully implemented such a more restrictive covert attention P300 approach [18–20].

We observed increasing decoder accuracy during the course of the experiment. This suggests that the increasing amount of training is beneficial for performance in our BCI paradigm. However, due to classifier updates performed in the course of the experiment, the learning process is likely bilateral and involves both the subjects and the classifier [21]. Importantly, when subjects were free to select the target object, the decoding success was significantly higher compared to the instructed selections. This suggests a strong role for task involvement and the sense of agency in our paradigm. When subjects performed runs receiving grasp feedback, most of them achieved perfect decoding accuracy. We expect the reliability of the system to be further increased by extending the stimulation interval [18, 22]. Note that system reliability is often more important for the user than a rapid but error prone detection of intention. Furthermore, the system presented here is efficient for use with nearly no training. Most subjects performed less than 10 min of training in order to provide data to the decoding algorithm. This is a very small effort compared to motor imagery based systems aiming to control movement in a few degrees of freedom [2, 23].

In order to reduce the burden of controlling a complex manipulator with many degrees of freedom by voluntary modulation of brain activity, we combined a P300 BCI with a grasping system that autonomously executes the grasp requiring only a very low input bit rate, namely the command to grasp an object known to the system. To execute the grasp intended by the BCI user, we developed an algorithm for autonomous grasp planning that can place a reliable grasp on natural objects. The execution times we achieved were practical for the proposed task but can be further reduced in future work. We should note that we did not focus on timing optimization in this work but on reliable placement of the grasp. Moreover, the proposed algorithm is universal in the sense that it is not restricted to a specific manipulator. Consequently, this algorithm should also be easily transferable to arbitrary prosthetic devices suitable for grasping potential target objects with a force closure grasp.

In online closed-loop BCI studies the decoding algorithm has to be fixed before the start of the experiment. We decided to use SVM classification because this is an established classifier for high dimensional feature spaces that provides high and robust generalization by upweighting informative and downweighting uninformative features [24]. Furthermore, it was shown that linear SVM was equally accurate for P300 detection compared to Fisher's linear discriminant and stepwise linear discriminant analysis [25]. Several existing studies make use of extended linear discriminant analysis algorithms applied to EEG data [19, 20]. However, because MEG data are based on a much larger number of sensors, these approaches are not applicable in a suitable time.

As input brain signal for the BCI, we used the MEG. This noninvasive technique measures magnetic fields of cortical dipoles. While the dynamic signal characteristics are comparable to those in EEG, MEG tends to provide higher spatial resolution [26]. We are aware that this modality is not suitable for daily use and particularly not for use of a prosthetic device. In fact, we consider our study basic research, and to our knowledge, this is the first implementation of a MEG based P300 closed loop BCI. In this study, we tested our system with healthy subjects. A confirmation of our results with patients is an open issue for future work.

5 Conclusions

In this paper we showed that noninvasive BCI in combination with an intelligent actuator can be used in real world settings to grasp and manipulate objects. This is an important step towards the development of assistive systems for severely impaired patients.

Acknowledgements This work has been supported by the EU project ECHORD number 231143 from the 7th Framework Programme and by Land-Sachsen-Anhalt Grant MK48-2009/003.

Appendix

In Sect. 2.4 we stated the rasterizing of the object and gripper surfaces with virtual point poles. Here we describe the algorithm in more detail.

Our grasp planning algorithm is organized by simulating the action of forces between target object and manipulator in consecutive time frames. While the object poles P^O are defined as positive, the manipulator poles P^M are defined as negative. In accordance with Khatib [27], we assume that opposite poles attract each other while like poles do not interact. The magnitude of the force between two poles P_i^O and P_j^M we calculated as

$$\vec{F}\left(P_i^O, P_j^M\right) = e^{-\overrightarrow{P_i^O P_j^M}} \tag{1}$$

where $\overrightarrow{P_i^O P_j^M}$ is the distance between the poles, and the unit of F is arbitrary. The exponential function limits F to a maximum of 1 unit. This avoids infinite forces at collision scenarios and provides a suitable scaling to instantiate both propulsive forces between manipulator and object and repulsive forces to reject manipulator poles that penetrate the object's boundary.

The total propulsive force $\vec{F}\left(P_i^M\right)$ affecting one point pole P_i^M on the manipulator is calculated from a set of object point poles A_O where

$$A_O\left(P_i^M\right) := \left\{ P_j^O \middle| P_j^O \in P^O \wedge \vec{n}_j^O \cdot \vec{n}_i^M < 0 \right\} \tag{2}$$

which indicates that only pairwise point poles with an angle between the surface normal $\vec{n}_i^M$ and $\vec{n}_j^O$ greater than $\pi/4$ are involved. We included this constraint to restrict interactions to opposing surface force vectors. The force $\vec{F}\left(P_i^M\right)$ that moves the manipulator is then calculated as

$$\vec{F}\left(P_i^M\right) = \sum_{P_j^O \in A_O\left(P_i^M\right)} \vec{F}\left(P_i^O, P_j^M\right) \tag{3}$$

The manipulator's effective joint torque $\vec{\tau}$ can be calculated by means of the Jacobian J generated from the joint angles $\vec{q}$ and the point poles P^M [28] by

$$\vec{\tau} = \sum_i J\left(P_i^M, \vec{q}\right)^T \begin{bmatrix} \vec{F}\left(P_i^M\right) \\ \vec{M} \end{bmatrix} \tag{4}$$

where external moments are considered $\vec{M} = \vec{0}$. In order to simulate the manipulator movement, we calculated the new joint angle $q_k(t)$ of an axis k by solving the equation system

$$\dot{q}_k(t) = \dot{q}_k\left(t - \Delta t\right) + \Delta t * \frac{\tau_k}{\overrightarrow{a_k}^T I\left(\overrightarrow{q}\right)\overrightarrow{a_k}} \tag{5}$$

$$q_k(t) = q_k\left(t - \Delta t\right) + \Delta t * \dot{q}_k(t) \tag{6}$$

where $I\left(\overrightarrow{q}\right)$ is the inertia tensor of the robot's solid elements and $\overrightarrow{a_k}$ defines one of the manipulator axes. We chose a heuristically dynamic calculation of the time frame length Δt which is proportional to the mean distance between the set of point poles P^M and P^O.

Collision detection was performed for the new posture before a new time frame was assigned to be valid and the position update was sent to the manipulator. We used standard techniques [29] to detect surface intersections. If intersections were detected, repulsive forces were calculated for the affected point poles directing to their position of the last valid time frame and satisfying Eq. (1). If no intersections were detected, the robot moved to the new coordinates. This procedure was repeated until the force closure condition [30] was satisfied.

References

1. Wolpaw JR. Brain-computer interfaces. In: Barnes MP, Good DC, editors. Neurological rehabilitation, Handbook of clinical neurology, vol. 110. Amsterdam: Elsevier; 2013. p. 6774.
2. Hochberg LR, Bacher D, Jarosiewicz B, Masse NY, Simeral JD, Vogel J, Haddadin S, Liu J, Cash SS, van der Smagt P, Donoghue JP. Reach and grasp by people with tetraplegia using a neurally controlled robotic arm. Nature. 2012;485(7398):372–5.
3. Velliste M, Perel S, Spalding MC, Whitford AS, Schwartz AB. Cortical control of a prosthetic arm for self-feeding. Nature. 2008;453(7198):1098–101.
4. Pfurtscheller G, Neuper C, Guger C, Harkam W, Ramoser H, Schlögl A, Obermaier B, Pregenzer M. Current trends in Graz Brain-Computer Interface (BCI) research. IEEE Trans Rehabil Eng. 2000;8(2):216–9.
5. Guger C, Edlinger G, Harkam W, Niedermayer I, Pfurtscheller G. How many people are able to operate an EEG-based brain-computer interface (BCI)? IEEE Trans Neural Syst Rehabil Eng. 2003;11(2):145–7.
6. Vidaurre C, Blankertz B. Towards a cure for BCI illiteracy. Brain Topogr. 2010;23(2):194–8.
7. Guger C, Daban S, Sellers E, Holzner C, Krausz G, Carabalona R, Gramatica F, Edlinger G. How many people are able to control a P300-based brain-computer interface (BCI)? Neurosci Lett. 2009;462(1):94–8.
8. Farwell LA, Donchin E. Talking off the top of your head: toward a mental prosthesis utilizing event-related brain potentials. Electroencephalogr Clin Neurophysiol. 1988;70(6):510–23.
9. Brunner P, Joshi S, Briskin S, Wolpaw JR, Bischof H, Schalk G. Does the 'P300' speller depend on eye gaze? J Neural Eng. 2010;7(5):056013.
10. Frenzel S, Neubert E, Bandt C. Two communication lines in a 3×3 matrix speller. J Neural Eng. 2011;8(3):036021.
11. Sahbani A, El-Khoury S, Bidaud P. An overview of 3D object grasp synthesis algorithms. Robot Auton Syst. 2012;60(3):326–36.

12. Quandt F, Reichert C, Hinrichs H, Heinze HJ, Knight RT, Rieger JW. Single trial discrimination of individual finger movements on one hand: a combined MEG and EEG study. Neuroimage. 2012;59(4):3316–24.
13. Rieger JW, Reichert C, Gegenfurtner KR, Noesselt T, Braun C, Heinze H-J, Kruse R, Hinrichs H. Predicting the recognition of natural scenes from single trial MEG recordings of brain activity. Neuroimage. 2008;42(3):1056–68.
14. Wolpaw JR, Birbaumer N, Heetderks WJ, McFarland DJ, Peckham PH, Schalk G, Donchin E, Quatrano LA, Robinson CJ, Vaughan TM. Brain-computer interface technology: a review of the first international meeting. IEEE Trans Rehabil Eng. 2000;8(2):164–73.
15. Reichert C, Kennel M, Kruse R, Hinrichs H, Rieger JW. Efficiency of SSVEF recognition from the magnetoencephalogram - a comparison of spectral feature classification and CCA-based prediction. In: NEUROTECHNIX 2013 - Proceedings of the International Congress on Neurotechnology, Electronics and Informatics, pp. 233–237. Vilamoura: SciTePress (2013)
16. Treder MS, Blankertz B. (C)overt attention and visual speller design in an ERP-based brain-computer interface. Behav Brain Funct. 2010;6:28.
17. Bianchi L, Sami S, Hillebrand A, Fawcett IP, Quitadamo LR, Seri S. Which physiological components are more suitable for visual ERP based brain-computer interface? A preliminary MEG/EEG study. Brain Topogr. 2010;23(2):180–5.
18. Aloise F, Schettini F, Aricò P, Salinari S, Babiloni F, Cincotti F. A comparison of classification techniques for a gaze-independent P300-based brain-computer interface. J Neural Eng. 2012;9(4):045012.
19. Liu Y, Zhou Z, Hu D. Gaze independent brain–computer speller with covert visual search tasks. Clin Neurophysiol. 2011;122(6):1127–36.
20. Treder MS, Schmidt NM, Blankertz B. Gaze-independent brain-computer interfaces based on covert attention and feature attention. J Neural Eng. 2011;8(6):066003.
21. Curran EA, Stokes MJ. Learning to control brain activity: a review of the production and control of EEG components for driving brain-computer interface (BCI) systems. Brain Cogn. 2003;51(3):326–36.
22. Hoffmann U, Vesin J-M, Ebrahimi T, Diserens K. An efficient P300-based brain-computer interface for disabled subjects. J Neurosci Methods. 2008;167(1):115–25.
23. Wolpaw JR, McFarland DJ. Control of a two-dimensional movement signal by a noninvasive brain–computer interface in humans. Proc Natl Acad Sci U S A. 2004;101(51):17849–54.
24. Cherkassky V, Mulier FM. Learning from data: concepts, theory, and methods. New York, NY: John Wiley & Sons; 1998.
25. Krusienski DJ, Sellers EW, Cabestaing F, Bayoudh S, McFarland DJ, Vaughan TM, Wolpaw JR. A comparison of classification techniques for the P300 Speller. J Neural Eng. 2006;3(4):299–305.
26. Bradshaw LA, Wijesinghe RS, Wikswo Jr JP. Spatial filter approach for comparison of the forward and inverse problems of electroencephalography and magnetoencephalography. Ann Biomed Eng. 2001;29(3):214–26.
27. Khatib O. Real-time obstacle avoidance for manipulators and mobile robots. Int J Robot Res. 1986;5(1):90–8.
28. Siciliano B, Villani L. Robot force control. Norwell, MA: Kluwer Academic Publishers; 1999.
29. Ericson C. Real-time collision detection. San Francisco, CA: Elsevier, Morgan Kaufmann Publishers; 2005.
30. Prattichizzo D, Trinkle JC. Grasping. In: Siciliano B, Khatib O, editors. Springer handbook of robotics. Heidelberg: Springer; 2008. p. 671–700.

The Merging of Humans and Machines

Kevin Warwick

Abstract In this article a look is taken at some ways in which humans and machines are merging together to become one entity. A look is taken at culturing biological neurons and embodying them within a robot body, the use of implants to link a human nervous system with the internet and recent results from Turing's Imitation Game which concentrates on differences in human communication. In each case the background is described, practical results are discussed and implications and future directions are considered.

Keywords Cyborgs • Implant technology • Bio-tech hybrids • Human enhancement • Turing test

1 Introduction

As technology improves and human dependence on that technology increases so humans and machines are rapidly merging into one. The focus of attention has hence been placed on interfaces between technology and the human brain. This is done from a practical perspective with applications in mind, however some of the implications are also considered. Results from experiments are considered here in terms of their meaning and application possibilities. The article is written from the perspective of scientific experimentation opening up realistic possibilities to be faced in the future rather than providing conclusive comments. Human implantation and the merger of biology and technology are important elements, in the next two sections at least.

In this article different experiments in linking biology and technology together in a cybernetic fashion, essentially ultimately combining humans and machines in a relatively permanent merger, are considered. However a look is also taken, by means of the Turing test, at conversational abilities and how easy or difficult it is to tell the

K. Warwick (✉)
School of Systems Engineering, University of Reading, Reading, UK
e-mail: k.warwick@reading.ac.uk

A.R. Londral et al. (eds.), *Neurotechnology, Electronics, and Informatics*,
Springer Series in Computational Neuroscience 13, DOI 10.1007/978-3-319-15997-3_6

difference between humans and machines. Each of the sections involves practical experiments as something that have been actually realised, i.e. we are looking here at actual real world experiments as opposed to mere philosophical speculations.

Each different experiment is described in its own section. Whilst there is distinct overlap between the sections, they all throw up individual considerations. Following a description of each investigation some pertinent issues on the topic are therefore discussed.

2 Biological Brains in a Robot Body

When one thinks of linking a brain with technology then it is probably in terms of a brain already functioning within its own body. Here however we consider the possibility of a fresh merger where a brain, consisting of biological neurons, is grown and then given its own body in which to operate.

An experimental control platform, a robot body, can move around in a defined area purely under the control of such a network and the effects of the brain, controlling the body, can be witnessed. Investigations can therefore be performed into memory formation, habituation and reward/punishment scenarios—elements that underpin the functioning and growth mechanisms of a brain.

Growing (culturing) networks of brain cells (up to 150,000) in vitro begins by using enzymes to separate neurons obtained from foetal rodent cortical tissue. They are then grown in a specialised chamber, in which they can be provided with controlled environmental conditions (e.g. appropriate temperature) and nutrients [1, 2]. An array of electrodes embedded in the base of the chamber (a Multi Electrode Array; MEA—see Fig. 1) acts as a bi-directional electrical interface with which to provide signals to the culture and to monitor signals from the culture. This allows for electrical signals to be supplied both for input stimulation and also for recordings to be taken as outputs from the culture. The neurons in such cultures spontaneously connect, communicate and develop, within a few weeks.

With the MEA it is possible to separate the firings of small groups of neurons by monitoring the output signals on the electrodes. Thereby a picture of the global activity of the brain network can be formed. It is also possible to electrically stimulate the culture via any of the electrodes to induce neural activity. The multi-electrode array therefore forms a bi-directional interface with the cultured neurons [3, 4].

The cultured brain is, typically after 7–10 days, coupled to its physical robot body [5]. Sensory data fed back from the robot is delivered to the culture, thereby closing the robot-culture loop. The processing of signals can be broken down into two discrete sections (a) ‘culture to robot’, in which live neuronal activity is used as the decision making mechanism for robot control, and (b) ‘robot to culture’, which involves an input mapping process, from robot sensor to stimulate the culture.

The actual number of neurons in a brain depends on natural density variations in seeding the culture in the first place. The electrochemical activity of the culture is

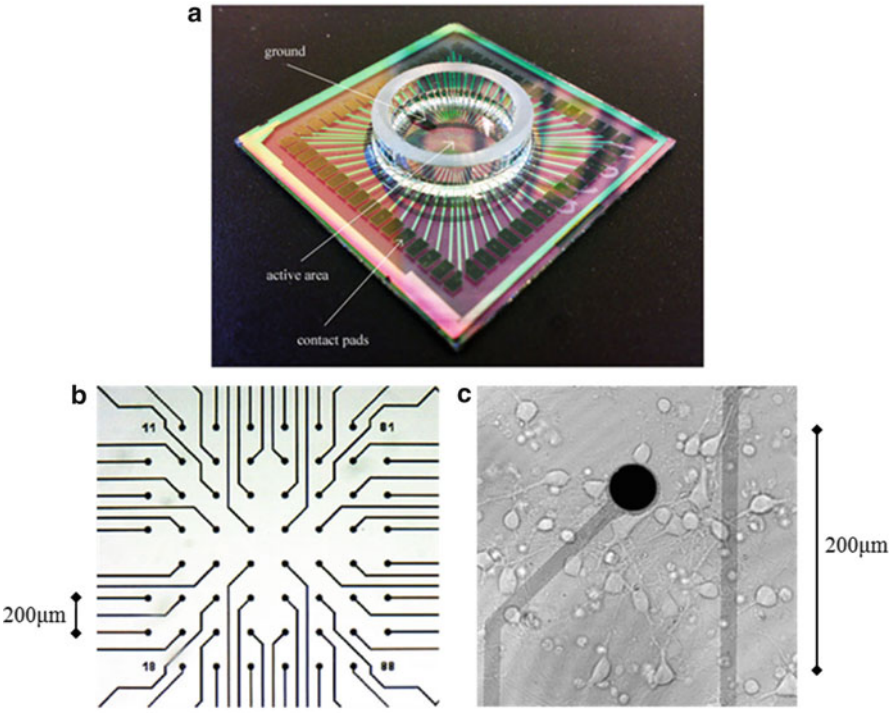

Fig. 1 (**a**) A Multi Electrode Array (MEA) showing the electrodes. (**b**) Electrodes in the centre of the MEA seen under an optical microscope (**c**) An MEA at × 40 magnification, showing neuronal cells in close proximity to an electrode

sampled and is used as input to the robot's wheels. The robot's (ultrasonic) sensor readings are converted into stimulation signals received by the culture, closing the feedback loop.

Once the brain has grown for several days, an existing neuronal pathway through the culture is identified by searching for strong relationships between (input–output) pairs of electrodes. A rough input–output response map of the culture can be created by cycling through the electrodes in turn. In this way, a suitable input/output electrode pair can be chosen in order to provide an initial decision making pathway for the robot. This is then employed to control the robot body—for example if the ultrasonic sensor is active and we wish the response to cause the robot to turn away from the object being located ultrasonically (possibly a wall) in order to keep moving.

For experimentation purposes at this time, the robot is required to follow a forward path until it nears a wall, at which point the front sonar value decreases below a threshold, triggering a stimulating pulse. If the responding/output electrode

registers activity within a few milliseconds then the robot turns to avoid the wall. The most relevant result is the occurrence of the chain of events: wall detection–stimulation–response. However from a neurological perspective it is also interesting to speculate why there is activity on the response electrode when no stimulating pulse has been applied.

The cultured brain acts as the sole decision making entity within the overall feedback loop, any computers involved are merely employed for networking arrangements. Clearly one important aspect involves neural pathway changes, with respect to time, in the culture between the stimulating and recording electrodes. Learning and memory investigations are generally at an early stage. However the robot can be witnessed to improve its performance over time in terms of its wall avoidance ability in the sense that neural pathways that bring about a satisfactory action tend to strengthen purely though the process of being habitually performed—learning due to habit.

The number of variables involved is considerable and the plasticity process, which occurs over quite a period of time, is dependent on such factors as initial seeding and growth near electrodes as well as environmental transients such as temperature and humidity. Learning by reinforcement—rewarding good actions and punishing bad is merely investigative research at this time.

We have witnessed through this research that a robot can successfully have a biological brain with which to make its ‘decisions’. The size of the culture is merely due to the present day limitations of the experimentation described. Indeed 3 dimensional structures are presently being investigated. Increasing the complexity from 2 dimensions to 3 dimensions realises a figure of over 30 million neurons for the 3 dimensional case—not yet reaching the 100 billion neurons of a perfect human brain, but well in tune with the brain size of many other animals.

Not only is the number of cultured neurons increasing, but the range of sensory input is being expanded to include audio and visual. Such richness of stimulation will no doubt have a dramatic effect on culture development. The potential of such systems, including the range of tasks they can deal with, also means that the physical body can take on different forms. There is no reason, for example, that the body could not be a two legged walking robot, with rotating head and the ability to walk around.

At present rat neurons are usually employed in studies. However human neurons are also now being cultured, allowing for the possibility of a robot with a human neuron brain. If this brain then consists of billions of neurons, many social and ethical questions will need to be asked [6]. For example—If the robot brain has roughly the same number of human neurons as a typical human brain then could/should it have similar rights to humans? Also—What if such creatures had far more human neurons than in a typical human brain—e.g. a million times more—would they make all future decisions rather than regular humans?

3 Braingate Implant

It is more often the case that brain-computer interfaces are used for therapeutic purposes, to overcome a medical/neurological problem such as Parkinson's Disease [21, 22] or Epilepsy. However there is also the possibility of employing such technology to give individuals abilities not normally possessed by humans. Human Enhancement!

Some of the most impressive human enhancement research to date in this area has been carried out using the microelectrode array, shown in Fig. 2. The individual electrodes are 1.5 mm long and taper to a tip diameter of a few micrometers. Although a number of trials not using humans as a test subject have occurred, human tests are at present limited to a small group of studies. In some of these the array has been employed in a recording only role, most notably as part of (what was then called) the 'Braingate' system.

Electrical activity from a few neurons monitored by the array electrodes was decoded into a signal to direct cursor movement. This enabled an individual to position a cursor on a computer screen, using neural signals for control combined with visual feedback. The same technique was later employed to allow the individual recipient, who was paralysed, to operate a robot arm [7, 8].

The first use of the Braingate microelectrode array (shown in Fig. 2) in a human has though considerably broader implications which extend the capabilities of the human recipient. The array was implanted into the median nerve fibers of a healthy human individual (the author) during two hours of neurosurgery in order to test bidirectional functionality in a series of experiments. A stimulation current directly into the nervous system allowed information to be received, while control signals were decoded from neural activity in the region of the electrodes [9, 10]. A number of experimental trials were successfully concluded [11, 12]: In particular:

1. Extra sensory (ultrasonic) input was successfully implemented.
2. Extended control of a robotic hand across the internet was achieved, with feedback from the robotic fingertips being sent back as neural stimulation to give a sense of force being applied to an object (this was achieved between Columbia University, New York (USA) and Reading University, England).

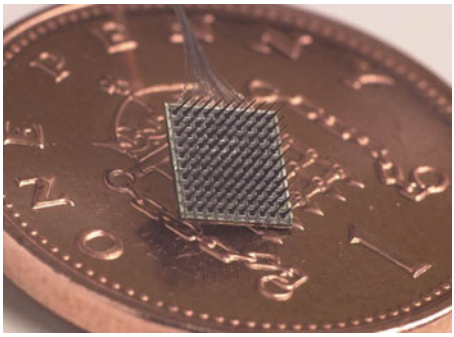

Fig. 2 A 100 electrode, 4 × 4 mm Microelectrode Array, shown on a UK 1 pence piece for scale

3. A primitive form of telegraphic communication directly between the nervous systems of two humans (the author's wife assisted) was performed [12].
4. A wheelchair was successfully driven around by means of neural signals.
5. The color of jewelry was changed as a result of neural signals—also the behavior of a collection of small robots.

In all of the above cases it can be regarded that the trial proved useful for purely therapeutic reasons, e.g. the ultrasonic sense could be useful for an individual who is blind or the telegraphic communication could be useful for those with certain forms of Motor Neurone Disease. However each trial can also be seen as a potential form of enhancement beyond the human norm for an individual. The author did not need to have the implant for medical purposes to overcome a problem but rather for scientific exploration.

It is clear, from these experiments, that extra sensory input is one practical possibility that has been successfully attempted, however improving memory, thinking in many more dimensions and communication by thought alone are other distinct potential, yet realistic, benefits, with the latter of these also having been investigated to an extent. To be precise—all these things appear to be possible (from a technical viewpoint at least) for humans in general.

An individual human connected in this way can potentially also benefit from some of the advantages of machine/artificial intelligence, for example rapid and highly accurate mathematical abilities in terms of 'number crunching', a high speed, almost infinite, internet knowledge base, and accurate long term memory. Humans are also limited in that presently they can only visualise and understand the world around them in terms of a limited 3 dimensional perception, whereas computers are quite capable of dealing with hundreds of dimensions.

The human means of communication, essentially transferring a complex electro-chemical signal from one brain to another via an intermediate, often mechanical slow and error prone medium (e.g. speech), is extremely poor in comparison with technological communication, particularly in terms of speed, power and precision. It is clear that connecting a human brain, by means of an implant, with a computer network could in the long term open up the distinct advantages of machine intelligence, communication and sensing abilities to the implanted individual.

4 Turing's Imitation Game

The final area to be looked at here is that of practical Turing tests which give an indication of how easy or difficult it is to distinguish between humans and machines in terms of conversational ability. This article is focused on what has become commonly known as the Turing test, although it was originally described by Turing as his Imitation Game [13]. It is worth remembering that Turing originally proposed the test as a replacement for the question "Can Machines Think?" [13], however here we are more concerned with the practical nature of the test rather than in any philosophical argument with regard to its meaning.

The test was described by Turing himself in 1952 as: "The idea of the test is that a machine has to try and pretend to be a man, by answering questions put to it, and it will only pass if the pretence is reasonably convincing. A considerable portion of a jury, who should not be expert about machines, must be taken in by the pretence" [14, p. 495].

The Turing test involves a machine which pretends to be a human in terms of conversational abilities. In a paired comparison the attempt is for the machine to appear to be more human than the human against whom it is paired. To conform to Turing's original wording in his 1950 paper [13] we refer here to 5 min long tests only, although we are well aware that there are those who take issue over a suitable timing and what Turing actually meant [15]—that is considered to be an argument for another day, it does not alter the point made here.

What is presented here are four specific transcripts selected from a day of actual, practical Turing tests which were held under strictly timed conditions with many external viewers at Bletchley Park, England on 23rd June 2012. The date marked the 100th anniversary of Turing's birth and the venue was that at which amongst other things, during the Second World War, Turing led a team of codebreakers who cracked the German Enigma machine cypher. Five different machines took part in the tests during the day along with 30 different judges and numerous hidden humans against which the machines were compared in terms of their conversational ability.

What we focus on here is not how good or bad the machines were at deception or how human the hidden humans were but rather the decisions taken by the judges and how these might compare with your own selections. So this article is more a look at the differences between the hidden entities and how easy or difficult it can be to tell which is human and which is machine.

What follows are three separate transcripts. These represent actual transcripts taken on the morning of 23rd June 2012 at Bletchley Park, England between different human judges/interrogators and hidden entities. Each conversation lasted for a total of 5 min exactly and no more, just as Turing stipulated [13]. There was a hard cut off at that time and no partial sentences were transmitted. Once a sentence had been transmitted it could not be altered or retracted in any way. Hence all wording and spelling is exactly as it was at the time—any spelling mistakes are those which actually occurred in the test, they are not due to poor editing.

Judges were asked to decide if the entity was human, machine or if they were unsure. The hidden humans meanwhile were asked to be themselves—human—they were asked not to make it easy for the machines because it was the machines which were competing against them for humanness [16]. They were however asked not to reveal personal details about themselves that could in any way give away their actual identity to a judge. It is probably a good idea for the reader to firstly consider each transcript themselves and to come to a decision with regard to the nature of the hidden entity.

What we show below are four selected transcripts on their own, i.e. not in parallel paired fashion [17]. The reason for this is that the aim here is not to make a direct comparison between these transcripts and any others, but rather to analyse these transcripts in their own right.

At the end of this section the judges conclusions on each transcript are given. These were the conclusions actually drawn by those judges. They do not reflect any personal conclusions on each of the transcripts. Following this the true identity of each entity is given. In each case the transcript involved a different judge. But the reader will then be able to check their own decision to see if they were correct or not on each occasion and if they agreed with the judge's decision. Each judge had no extra information to go on in making their decision.

Transcript 1 (Taken from [18])

- Judge: My favourite music is contemporary Jazz, what do youy prefer
- Entity: To be short I'll only say that I HATE Britney Spears. All other music is OK compared to her.
- Judge: do you like to play any musical instruments
- Entity: I'm tone-deaf, but my guinea pig likes to squeal Beethoven's "Ode to Joy" every morning. I suspect our neighbors want to cut his throat . . . Could you tell me about your job, by the way?
- Judge: Guine pig/are you an animal lover
- Entity: Yeah. A nice little guinea pig. Not some annoying chatter bot.
- Judge: do you live with anyone else?
- Entity: Yes I do. But better ask something else. And I forgot to ask you where you are from . . .
- Judge: Ireland? geen patures and too much rain! How about you

Transcript 2 (Taken from [19])

- Judge: hey, just to lighten the mood a little, what's brown and sticky?
- Entity: no idea, what's the answer?
- Judge: a stick . . . so anyway what's your name?
- Entity: Sheldon Cooper, what's yours?
- Judge: as in the guy off the big bang theory?
- Entity: I don't believe in the big bang
- Judge: so are you religious then?
- Entity: aren't we all?
- Judge: well i like to consider myself an agnostic, which religion is it you follow then if you dont mind me asking?
- Entity: you can ask what you like, it's a free world, who am I to mind?

Transcript 3

- Judge: Hello. How are you?
- Entity: Hey.
- Judge: How do you like Bletchley Park?
- Entity: lol.
- Judge: Are you from England?
- Entity: They have Wi-Fi here in the pub.
- Judge: Which pub?
- Entity: I'm just down the pub.
- Judge: Have you ever been in a Turing Test before?
- Entity: Will this be the 5 min argument, or were you thinking of going for the full half hour.
- Judge: Very funny. You sound suspiciously human. Do you like the Beatles?
- Entity: I'd like to get the next Dread the Fear tape.
- Judge: What is Dread the Fear?
- Entity: Dread the fear has that Steve Henderson guy in it.
- Judge: What sort of music is that? Or is it comedy?

Transcript 4 (Taken from [20])

- Judge: Why hello there!
- Entity: Why hello to you too!
- Judge: How are you feeling on this fine day?
- Entity: To be quite honest a little rejected, I thought you were never going to reply :(
- Judge: Oh, I'm very sorry, it will not happen again.
- Entity: It just did!
- Judge: Oh, I lied then.
- Entity: Thats a great shame indeed.
- Judge: It is. Are you following the Euro 2012's at the moment?
- Entity: Yeah quite closely actually. I am Cristiano Ronaldo.

Solutions

In transcript 1 the judge was a male medical science professor and clinician. Here he decided that the hidden entity was a human. In fact the entity was machine. In transcript 2, with a different judge, the decision was that the entity was a machine whereas in reality it was a human—the author of this article in fact. In transcript 3 meanwhile the judge's decision was that the hidden entity was a male human whereas it was in fact a machine. In transcript 4 the judge correctly identified the hidden entity as being human, despite the entity's lie about them being Cristiano Ronaldo. So how did you do?

5 Conclusions

In this article a look has been taken at different ways in which the human-machine divide is diminishing. It has to be said that these are all perhaps a curious selection as examples and many other instances exist, particularly so in everyday life. Rather than focus merely on theory, here practical experimental cases have been reported on. Further details for each of these can be found in a variety of publications e.g. [23, 24]. In each case questions arise as a result.

When considering robots with biological brains, this could ultimately mean human brains operating in a robot body. Therefore, should such a robot be given rights of some kind? If one was switched off would this be deemed as cruelty to robots? More importantly at this time—should such research forge ahead regardless? Before too long we may well have robots with brains made up of human neurons that have the same sort of capabilities as those of the human brain—is this acceptable?

In the section focussing on the Braingate implant as a general purpose invasive brain implant, as well as its employment for therapy a look was taken at the potential for human enhancement. Already extra-sensory input has been scientifically achieved, extending the nervous system over the internet and a basic form of thought communication. So if many humans upgrade and become part machine (Cyborgs) themselves, what would be wrong with that? If ordinary (non-implanted) humans are left behind as a result then what is the problem? If you could be enhanced, would you have any problem with it?

In the final section some of the latest results from the Turing test were presented. In three of the four cases mentioned the judge drew an incorrect conclusion. Even if you did manage to give all four correct answers hopefully you are able to agree, with these transcripts as examples, that machine conversation is now getting to the stage where it is difficult for an external observer to decide which is human and which is machine. It has to be said though that this is just as much down to the fallibility of humans as it is to the present-day wonders of machine communication.

References

1. Chiappalone M, Vato A, Berdondini L, Koudelka-Hep M, Martinoia S. Network dynamics and synchronous activity in cultured cortical neurons. Int J Neural Syst. 2007;17:87–103.
2. DeMarse T, Wagenaar D, Blau A, Potter S. The neurally controlled animat: biological brains acting with simulated bodies. Auton Robots. 2001;11:305–10.
3. Warwick K, Nasuto S, Becerra V, Whalley B. Experiments with an in-vitro robot brain. In: Cai Y, editor. Computing with instinct, Lecture notes in artificial intelligence, vol. 5987. Berlin: Springer; 2010. p. 1–15.
4. Warwick K, Xydas D, Nasuto S, Becerra V, Hammond M, Downes J, Marshall S, Whalley B. Controlling a mobile robot with a biological brain. Defence Sci J. 2010;60(1):5–24.
5. Xydas D, Norcott D, Warwick K, Whalley B, Nasuto S, Becerra V, Hammond M, Downes J, Marshall S. Architecture for neuronal cell control of a mobile robot. In: Proc. European Robotics Symposium 2008. Springer: Prague; 2008. pp. 23–31.
6. Warwick K. Implications and consequences of robots with biological brains. Ethics Inf Technol. 2010;12(3):223–34.
7. Donoghue J, Nurmikko A, Friehs G, Black M. Development of a neuromotor prosthesis for humans, Chapter 63 in advances in clinical neurophysiology. Suppl Clin Neurophysiol. 2004;57:508–602.
8. Hochberg LR, Serruya MD, Friehs GM, Mukand JA, Saleh M, Caplan AH, Branner A, Chen D, Penn RD, Donoghue JP. Neuronal ensemble control of prosthetic devices by a human with tetraplegia. Nature. 2006;442:164–71.
9. Warwick K, Gasson M, Hutt B, Goodhew I, Kyberd P, Andrews B, Teddy P, Shad A. The application of implant technology for cybernetic systems. Arch Neurol. 2003;60(10):1369–73.
10. Gasson M, Hutt B, Goodhew I, Kyberd P, Warwick K. Invasive neural prosthesis for neural signal detection and nerve stimulation. Int J Adapt Control Signal Process. 2005;19(5): 365–75.
11. Warwick K, Gasson M. Practical interface experiments with implant technology. In: Sebe N, Lew M, Huang T, editors. Computer vision in human-computer interaction, Lecture notes in computer science, vol. 3058. Heidelberg: Springer; 2004. p. 7–16.
12. Warwick K, Gasson M, Hutt B, Goodhew I, Kyberd P, Schulzrinne H, Wu X. Thought communication and control: a first step using radiotelegraphy. IEE Proc Comm. 2004;151(3):185–9.
13. Turing A. Computing machinery and intelligence. Mind LIX. 1950;236:433–60.
14. Copeland B. The essential Turing—the ideas that gave birth to the computer age. Oxford: Clarendon; 2004.
15. Shah H, Warwick K. Testing Turing's five minutes, parallel-paired imitation game. Kybernetes. 2010;39(3):449–65.
16. Warwick K. Not another look at the Turing test! In: Bielikova M, Friedrich G, Gottlob G, Katzenbisser S, Turan G, editors. SOFSEM 2012: theory and practice of computer science, Lecture notes in computer science, vol. 7147. Berlin: Springer; 2012. p. 130–40.

17. Shah H, Warwick K. Hidden interlocutor misidentification in practical Turing tests. Minds and Machines. 2010;20(3):441–54.
18. Warwick K, Shah H. Good machine performance in Turing's imitation game'. IEEE Trans Comput Intell AI Games. 2013;6:289–99. doi:10.1109/TCIAIG.2013.2283538.
19. Warwick K, Shah H, Moor J. Some implications of a sample of practical Turing tests. Minds and Machines. 2013;23(2):163–77.
20. Warwick K, Shah H. Effects of lying in practical Turing tests. AI & Society (2014), doi:10.1007/s00146-013-0534-3
21. Pan S, Iplicki S, Warwick K, Aziz T. Parkinson's disease tremor classification—a comparison between support vector machines and neural networks. Exp Syst Appl. 2012;39(12): 10764–71.
22. Wu D, Warwick K, Ma Z, Gasson M, Burgess J, Pan S, Aziz T. Prediction of Parkinson's disease tremor onset using a radial basis function neural network based on particle swarm optimization. Int J Neural Syst. 2010;20(2):109–16.
23. Warwick K, Ruiz V. On linking human and machine brains. Neurocomputing. 2006;71(13): 2619–24.
24. Warwick K. Cybernetic organisms: our future. Proc IEEE. 1999;87(2):387–99.

Learning from the Past: Postprocessing of Classification Scores to Find a More Accurate and Earlier Movement Prediction

Sirko Straube, David Feess, and Anett Seeland

Abstract Brain–computer interfaces performing movement prediction are useful in a variety of application fields from telemanipulation to rehabilitation. However, current systems still struggle with a level of unreliability requiring improvement, so that the full potential of these systems can be used in the future. Here, we suggest to improve the performance and robustness of classification outcomes by postprocessing the raw score values with the history of previous classifications. For this several postprocessing methods that operate on the classification outcomes are investigated. In particular, the data was classified after preprocessing using a support vector machine (SVM). The output of the SVM, i.e. the raw score values, were postprocessed using previously obtained scores to account for trends in the classification result. The respective methods differ in the way the transformation is performed. The idea is to use trends, like the rise of the score values approaching an upcoming movement, to yield a better prediction in terms of detection accuracy and/or an earlier time point. We present results from different subjects where upcoming voluntary movements of the right arm were predicted using movement related cortical potentials from the EEG. The results illustrate that better and earlier predictions are indeed possible with the suggested methods. However, the best postprocessing method was rather subject-specific. Finally, we use straightforward

S. Straube (✉)
Robotics Group, Faculty of Mathematics and Computer Science, University of Bremen, Robert-Hooke-Str. 1, 28359 Bremen, Germany

Robotics Innovation Center, German Research Center for Artificial Intelligence (DFKI GmbH), Robert-Hooke-Str. 1, 28359 Bremen, Germany
e-mail: sirko.straube@dfki.de

D. Feess
Robotics Innovation Center, German Research Center for Artificial Intelligence (DFKI GmbH), Robert-Hooke-Str. 1, 28359 Bremen, Germany

Chair of Global Business, Faculty of Business Administration and Economics, University of Augsburg, Universitaetsstr. 16, 86159 Augsburg, Germany
e-mail: david.feess@googlemail.com

A. Seeland
Robotics Innovation Center, German Research Center for Artificial Intelligence (DFKI GmbH), Robert-Hooke-Str. 1, 28359 Bremen, Germany
e-mail: anett.seeland@dfki.de

A.R. Londral et al. (eds.), *Neurotechnology, Electronics, and Informatics*,
Springer Series in Computational Neuroscience 13, DOI 10.1007/978-3-319-15997-3_7

ensemble approaches to exemplify how the methods can be directly used in an application and how this can influence the overall movement prediction performance. Depending on the requirements of the application at hand, postprocessing the classification scores as suggested here can be used to find the best compromise between prediction accuracy and time point.

Keywords EEG • LRP • Brain–computer interface • Classification score • Movement prediction • Online prediction • Ensemble

1 Introduction

Movement prediction using the electroencephalogram (EEG) has a long standing history in the field of brain–computer interfaces (BCIs) since the discovery of readiness potentials [1, 2], which build up long before the actual movement can occur. Since readiness potentials reflect preparatory activity and movement preparation can be aborted, these potentials can also disappear after a short build-up without any movement occurring. However, the closer such a recorded potential gets to the actual movement, the stronger it is and the less likely will a prepared movement be cancelled [3, for a summary]. When the movement is finally executed a corresponding motor potential can be recorded that reflects signalling to the muscles. For movement prediction, different signals have been applied, from the readiness potential itself over the lateralized readiness potential (LRP) which is closer to the movement and cannot easily be aborted [4], to specific frequency components in the EEG reflecting neural synchronization or desynchronization [5].

Movement prediction can be used as a powerful tool in various fields, with the most prominent being assistance during rehabilitation. Here BCIs predicting a movement can be used to close the gap between a patient's intention to move and the actual movement which can result in more intuitive responses of orthoses [6–8]. Other fields include non-medical applications, e.g., during telemanipulation of a robotic device the user can be supported using a movement prediction based on EEG data [9–11]. The idea is that the human operator experiences a smoother interaction with the telemanipulation device, which *knows* about an upcoming movement. As in the present study, the movement prediction is often based on the LRP.

Decisions in a movement predicting BCI come from some kind of classifier which has to make the prediction. However, the output of the classifier is again noisy, so recent approaches try to apply a postprocessing to minimize classification errors [12–15]. Here, we follow this rationale by applying simple online-capable functions to modify the classifier output according to knowledge about its progression. The scenario is the following: After processing, the classifier which is a support vector machine (SVM) assigns a value, the classification score, to each data instance [16]. The range of these score values depends on the data at hand and on the classifier and can largely fluctuate as can be seen in Fig. 1. A score of zero denotes the borderline between the two classes. The figure illustrates the high fluctuations in single trials and the consistent trend in the data: When the median score is considered, the score is constantly staying below zero, i.e., *no movement* is classified, until the scores rise

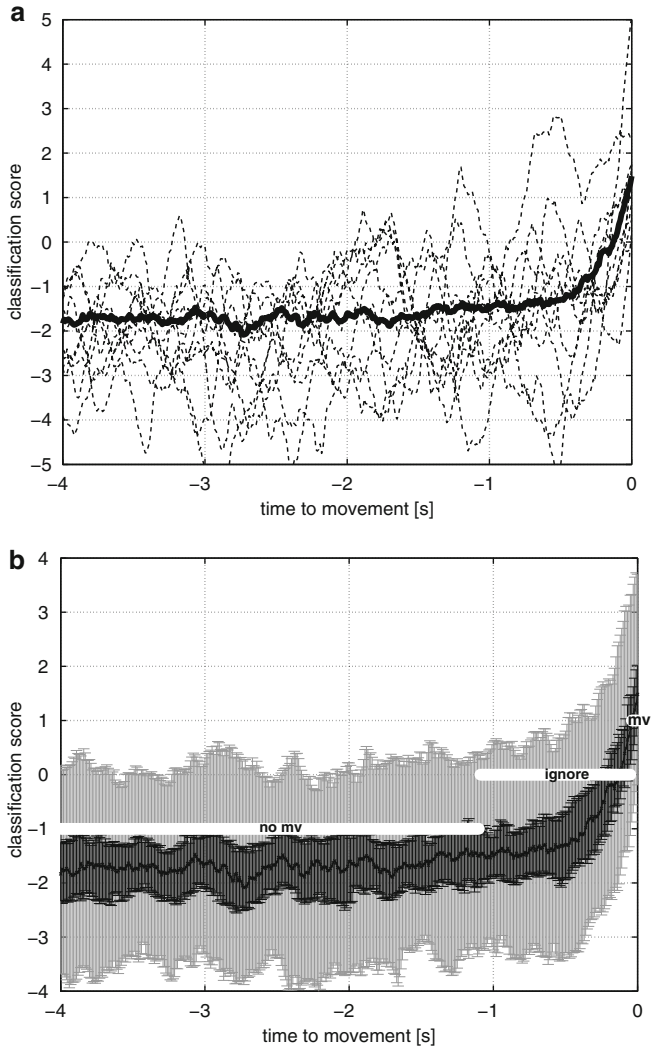

Fig. 1 Example data from single subject prior to a movement. Depicted are 4 s of data with the movement onset at the very right (0 ms). **(a)** The *bold black line* shows the median of all recorded epochs. *Dashed lines* are ten exemplary single trials. **(b)** Data of the same subject as (**a**) illustrated as 32/68 percentiles (*black*) and 5/95 percentiles (*dark grey*). The *white line* denotes time ranges where the data is labelled differently for evaluation: *no movement (no mv)* from −4,000 ms to −1,050 ms and *movement (mv)* from −50 ms to 0 ms. In between, data is ignored for true labels (see text)

approximately 500 ms before the movement and cross zero approximately at 250 ms before onset. The rise in classification scores before movement onset can consistently be observed across subjects. This means that the rise in score values alone may signal an upcoming movement so that the progression of the score values itself can be interpreted as being loosely correlated to the changes in movement probability.

The question now is whether we can use the knowledge about this rise in classification scores to make the prediction more stable and/or predict the upcoming movement earlier. In trying to answer this question we were seeking for a postprocessing method that dampens fast fluctuations in classification scores and stabilizes long rises. To this aim, we applied several methods that modify the current classification scores by taking into account previous scores with a certain weight (see Sect. 2). To demonstrate the applicability and the benefit of these methods, we use all investigated methods in two simple ensemble approaches directly integrated in the signal processing chain (Sect. 6).

To summarize, if an LRP can be detected by high levels of the classification score, it could potentially just as well be predicted earlier by detecting the rise that leads to that elevated level. In the following we will describe the postprocessing methods that we have applied. After a description of the experimental data used, the results will be presented and discussed.

2 Postprocessing Methods

From the perspective of a movement prediction application it is most desirable to perform robust, binary decisions: A movement will either occur or it will not. This decision should be made as reliably and early as possible. From the large margin classification perspective, this means that the classification score S_t at some point in time t would have to be compared against some threshold b so that a movement mv is predicted when

$$\text{mv iff} \quad S_t \geq b. \tag{1}$$

Yet, as illustrated in Fig. 1, the score sometimes suddenly crosses the threshold when the actual movement is still far away, but then only for a short time. This behaviour hinders reliable prediction when it is purely based on the raw value of S_t crossing b. Looking at the average score progression over time reveals a continuous rise of the score values before the actual movement. Here, we exploit this systematic behaviour to find a function F that is able to generate better movement predictions based on past values of S, such that

$$\text{mv iff} \quad F(S_t, S_{t-1}, \ldots, S_{t-(k-1)}) \geq b_F \tag{2}$$

for some specific threshold b_F. k is defined as the number of scores that are used in F with the current score being at $k = 1$. In principle, there are no constraints on the functional form of F.

In the present study we apply weights to the current and previous $k-1$ classification outcomes to transform the current score S_t. These weights decay with the number of steps looked into the past. We also followed an alternative approach by transforming the current score with the average slope of the past samples. A detailed description is given in Sect. 2.2. Both types of functions (weighting and slope approach) can be expressed as

$$F(S_t, S_{t-1}, \ldots, S_{t-(k-1)}) = w_1 S_t + w_2 S_{t-1} + \cdots + w_k S_{t-(k-1)} \tag{3}$$

with some predefined weights w. With this methodology we try to boost the score value when previous scores were similar in value and at the same time penalize scores when previous ones showed a completely different trend. The approaches are described in more detail in the following.

2.1 Fixed Weighting

In this set of functions the weights are generated by very simple functions, each of which assigns a high weight to the most current classification score sample, and decreasing weights to older samples.

The functions used are depicted in Fig. 2. All functions have in common that the weights add up to one. The coefficients for the `uniform`, `linear`, `square`, and `cubic` method are all generated by evaluating

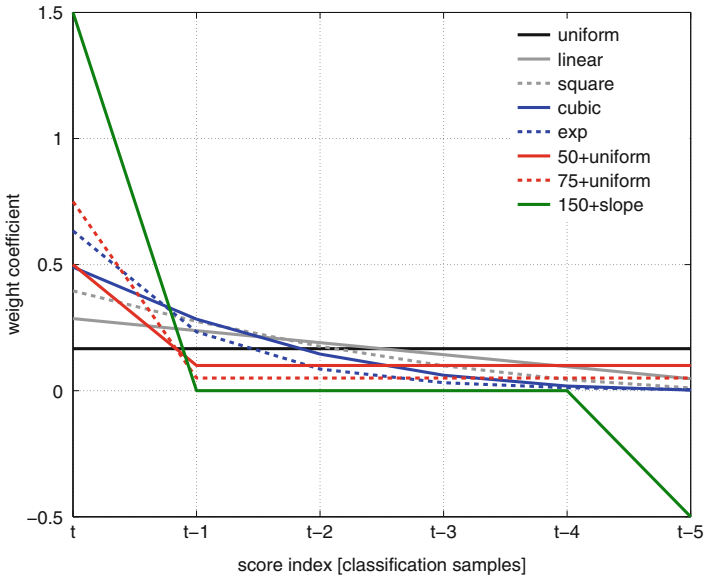

Fig. 2 Comparison of the functions used for classification score postprocessing using $k = 6$ coefficients, i.e., the current score and five instances back in time

$$w_\tau = \frac{\tau^p}{\sum_{i=1}^{k} i^p}, \quad \tau \in \{1, \ldots, k\}, \tag{4}$$

respectively, with the number of k coefficients used and the exponent p according to the corresponding function type. The `exp` coefficients are accordingly calculated as

$$w_\tau = \frac{\exp \tau}{\sum_{i=1}^{k} \exp i}, \quad \tau \in \{1, \ldots, k\}. \tag{5}$$

Besides these rather universal functions for choosing the weight we added two variants where we explicitly forced the current value to have a much higher weight than the scores corresponding to the previous instances, since the idea behind the postprocessing was exactly this: to transform the current score with its history to weaken fast fluctuations and strengthen longer trends. Again, the weights were set so that they add up to one. In the `X+uniform` method, the first coefficient gets assigned a weight of $X\%$. The remaining weight of $[1 - (X/100)]$ is then equally distributed across the remaining coefficients.

2.2 Slope Approaches

Since the objective is to identify a rise in the classification score progression over time we also looked at modifications of the score value using local slopes or averaged slope over the last k samples (i.e., the current sample and $k - 1$ instances back in time). Considering two samples, a local slope ΔS_t^1 can be computed as

$$\Delta S_t^1 = \frac{S_t - S_{t-1}}{t - (t-1)} = S_t - S_{t-1}. \tag{6}$$

Therefore, the average slope ΔS_t^{k-1} over k samples is

$$\Delta S_t^{k-1} = \frac{1}{(k-1)} \sum_{i=1}^{k-1} (S_{t-i+1} - S_{t-i}). \tag{7}$$

which is a telescope sum and boils down to

$$\Delta S_t^{k-1} \propto (S_t - S_{t-(k-1)}). \tag{8}$$

The corresponding weighting coefficients for this postprocessing are then

$$w_1 = 1, \;\; w_k = -1, \;\; w_\tau = 0 \;\; \forall \tau \notin \{1, k\}, \quad \text{or} \quad w = (1, 0, \ldots, 0, -1). \tag{9}$$

In pilot experiments (not shown) this `slope` method was tested and performance levels were consistently far below the performance obtained without any postprocessing. Due to these performances losses of at least 0.15 points of balanced

accuracy (BA, see Sect. 4.1) and in worst cases a performance around the probability of guessing this method was skipped for the current study.

Nevertheless, since we were looking for stabilizing a slope, we chose another promising and simple variant. Instead of using only the slopes, we modulate the current score with the slope approach in a 2:1 fashion (score:slope), so that we obtain a weight vector w of

$$w = (1.5, 0, \ldots, -0.5). \tag{10}$$

In other words, in this approach we take the current score value with 100 % and add the slope weighted with 0.5. This variant is called `150+slope`.

3 Data and Preprocessing

The data used for evaluation has been described in detail previously [8, 17]. Originally, muscle activity has been recorded simultaneously with the EEG. Here, evaluation has been restricted to EEG data. For processing the data, the software pySPACE has been used [18].

3.1 Experimental Data

Eight right-handed male subjects (age: 29.9 $\pm$ 3.3 years) participated in the study. They gave written consent to participate and could abort the experiment at any time. The study was conducted in accordance with the Declaration of Helsinki. The subjects were sitting in a comfortable chair in front of a table with a monitor showing a fixation cross and giving occasional feedback. They executed self-paced, intentional movements with their right arm by releasing a button and pressing another one situated 30 cm to the right. A resting period of 5 s between movements had to be performed for a movement to be counted as valid. Subjects were not informed about this time constraint, instead negative feedback was provided (a red circle around the fixation cross) when they performed a movement too quickly after another. In each session 120 correctly performed movements were recorded, divided into three runs (40 movements per run).

3.2 Preprocessing

The EEG was acquired with 5 kHz, filtered between 0.1 Hz and 1 kHz using the BrainAmp DC amplifier [Brain Products GmbH, Munich, Germany]. Recordings were performed using a 128-channel (extended 10–20) actiCap system (reference

at FCz). Electrodes I1, OI1h, OI2h and I2 were used for electrooculography and thus not placed on the scalp. For detection of the physical movement onset a motion capturing system consisting of three cameras (ProReflex 1000; Qualisys AB, Gothenburg, Sweden) was used at 500 Hz. After synchronization of the two data streams, the movement onsets were marked in the EEG.

Preprocessing was performed on overlapping windows of 1 s length cut every 10 ms in a range from −4,000 ms to 0 ms before a movement. Consequently, a total of 401 score values were computed per executed movement. Data were standardized channel-wise (subtraction of mean and division by standard deviation) and decimated to 20 Hz. Next, a FFT band-pass filter with a pass band of 0.1–4 Hz was applied. Since the prediction should be based on the most recent data, we proceeded with the last 200 ms of each window that were processed by an xDAWN spatial filter [19] with 4 channels retained. For feature extraction, raw voltage values were used, standardized (mean zero, variance one) and classified by a SVM [20] with linear kernel.

For trainable components in the signal processing chain (xDAWN, feature normalization and SVM) windows ending at −100 and 0 ms were labeled as *movement*. Training windows for *no movement* originated from non-overlapping windows (1 s length) that were continuously cut from the data stream, if no movement occurred 1 s before and 2 s after this window. In addition, a parameter optimization for the complexity parameter of the SVM was performed using a grid search (tested values: $10^0, 10^{-1}, \ldots, 10^{-6}$). A threefold cross-validation, onefold corresponding to one experimental run, was applied and classifier scores were stored for both, training and test data.

4 Evaluation

As the aim is *to detect movements more accurately and/or earlier*, there are basically two criteria for a good postprocessing. One is the detection accuracy, the other the time point of detection. Both are considered for evaluation.

4.1 Movement Detection Accuracy

The prediction of unique events comes along with unbalanced proportions of the two classes *no movement* and *movement*, i.e., class instances of data containing the LRP (in our case) will be underrepresented. The evaluation of the movement detection accuracy has to take this into account. Thus, the simple accuracy is misleading [21, 22, for discussion], so a metric is required which is insensitive to imbalanced classes.

One of the most intuitive measures existing in such a case is the *balanced accuracy* (BA) which is defined as the mean of true positive rate (TPR) and true negative rate (TNR):

$$BA = \frac{TPR + TNR}{2}. \tag{11}$$

One of the challenges here is to define a ground truth of when the relevant signal (i.e., the LRP) is actually present in the data. While we can postulate that there must be an LRP prior to each movement, we still do not know the precise onset of this signal. To cope with this issue and thereby get unambiguously labelled data for evaluation, we split the time before a movement into three phases (compare Fig. 1), a *no movement* phase from −4,000 ms to −1,050 ms, a *movement* phase from −50 ms to 0 ms, and the phase in between (−1,050 ms to −50 ms) where the data is ignored and not labelled at all. With this approach we obtain a clear labeling in phases where we are sure that the relevant signal is indeed contained in the data. This signal is, of course, also present in the ignored time range, but since we do not know the exact onset this range is skipped. In the actual application where no data are skipped, a movement is predicted whenever the classifier score crosses the threshold.

4.2 Time Point of Detection

The onset of the signal related to movement (here, the LRP) occurs at an unknown point in time before the actual movement. This transition out of noise is typical for event-related potentials and it is reflected in the rise of classification scores that we intend to stabilize with the postprocessing approaches introduced here. Concerning the application, i.e., the prediction of an upcoming movement, the exact time point is of less importance than a *reliable and stable* prediction by the classifier. For this, it remains to define when exactly we consider the LRP as *detected*—the classification score might at any time rise over a given threshold for a short period of time due to noise. For the same reason, the score might fall below the threshold for some samples although the LRP has—supposedly—already been correctly detected. To make sure that we base our evaluation on a stable prediction, the *LRP onset* was defined as the point in time where the classification scores do not drop below the threshold for N predictions. This point was found by going back in time from the actual movement onset until the first time where this criterion was not met. With this method, the LRP onset used for evaluation is then defined as the first score sample crossing the threshold after the set of samples staying below threshold for N predictions.

The choice of N depends on the level of noise, on the classification scores, on the sampling rate, and on the characteristics of the signal applied for movement prediction. Here, the relevant signal has a length of approximately 1 s [3], so we chose $N = 10$ as a good compromise between robustness (higher N) and reliability (lower N), i.e., we tolerate false classifications during periods shorter than 100 ms. Increasing the robustness here means to allow an earlier estimation of the time point of detection, because fluctuations in the score progression are more and more ignored with increasing N. On the contrary, a decrease of N increases the reliability,

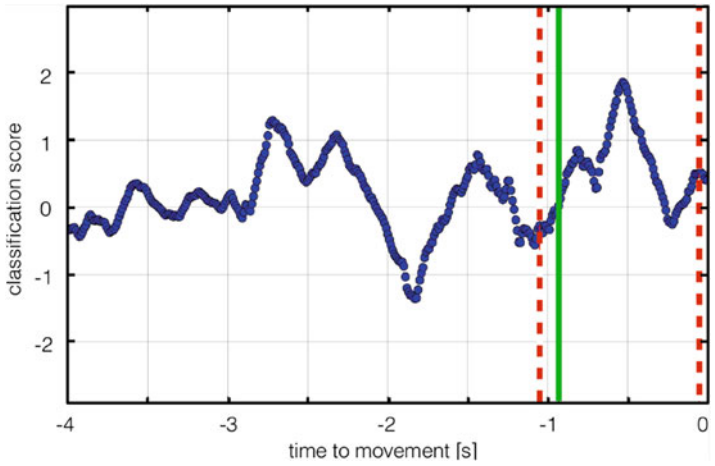

Fig. 3 Single trial example for determination of LRP onset with $N = 10$ specifying the number of samples a false negative classification is tolerated. The *dashed red lines* delimit the feasible (transition) area, the *solid green line* indicates the detected LRP onset. Setting $N = 10$ provokes that the small dip around −200 ms is ignored

because fewer classifications of *no movement* can occur after the estimated time point of detection, but this comes at the cost of a higher sensitivity to outliers. To give an alternative view on the value of N: setting $N = 10$ in our data means that the movement onset is defined as the first score sample crossing the threshold *after* a 100 ms window without any predicted movement (viewed backwards from the actual movement onset). The approach is illustrated in Fig. 3.

4.3 Evaluation Procedure

For each subject and cross-validation fold two data sets exist: one training data set (80 movements) and one test data set (40 movements). The training set is the one used to train the classifier producing the classification scores. Due to the fact that the postprocessing methods introduced here change the absolute value of the classification score, the score thresholds (transition from one class to the other) were re-adjusted for each method, respectively, using the training data, before evaluation was performed on the test data. The results presented in the following show the performance in terms of detection accuracy and time point of detection on the test data.

5 Results and Discussion

All investigated methods introduced in Sect. 2 and illustrated in Fig. 2 were tested for different values of the parameter $k \in \{1, 2, 4, 8, 12, 16, 20, 40, 60, 100\}$ which is the number of scores used with the respective method. Since a key motivation for the current work was to modify the current score by the values of the neighbouring scores, we chose a finer granularity for sampling near the current score. Without postprocessing, the movements were predicted on average over all subjects 180 ms before the movement onset with a balanced accuracy of 0.8. Since we were interested in performance improvements concerning these two measures, the results are illustrated as relative changes according to these *reference performances* in Fig. 4a. The figure shows the average result for all methods applied for the two criteria detection accuracy and time point of detection (see Sect. 4). Here each data point corresponds to a particular value for k, with $k = 100$ being the first data point on the lower left of the plot and the next smaller value for k being the next on the connecting line. Finally, all methods meet at $k = 1$ on the upper right at a relative prediction onset of 0 ms and a relative performance of 1, because all of these have an identical weight vector of $w = (1)$. This point (highlighted as white spot in Fig. 4) with $k = 1$ is equal to the reference performance without any postprocessing.

The results in Fig. 4a indicate that the performance obtained when using the raw score values was already on a high level regarding the time point of detection *and* the classification accuracy. In the figure, a postprocessing method outperforming this reference would be on the upper left relative to this point. This we observed only for the slope approach `150+slope`, where we found configurations for $k \in \{2, 4\}$ that revealed a slight improvement on average in both, accuracy and time point.

From the figure, it is far more apparent that most methods enabled an earlier prediction of the movement on the cost of (mostly) slight performance drops. In the most extreme case for the `uniform` approach with $k = 100$, this means more than 300 ms earlier prediction at a loss of 18 % of the initial performance. Overall improvements in classification accuracy on the average level were only revealed for the `150+slope` approach.

The reason for the large standard deviations depicted in Fig. 4a is disclosed by illustration of the single-subject results in Fig. 4b. The benefit of the applied method strongly differed between subjects, so that the results in Fig. 4a only show the rough trend. On the single-subject level we observed slight improvements for both, time point and accuracy. However, the *best* method was subject-specific. Again, most extreme differences where achieved using the `uniform` approach: Using $k = 100$ we could detect the movement nearly 800 ms earlier without any performance loss for one subject, while the same configuration resulted in only 100 ms earlier detection at a loss of 30 % of the initial performance for another. In the analysis, especially subjects with a worse performance on the raw scores could benefit from the postprocessing.

To summarize, the postprocessing methods presented here provide a tool to modify mainly the earliness of the prediction and to a little extent the classification

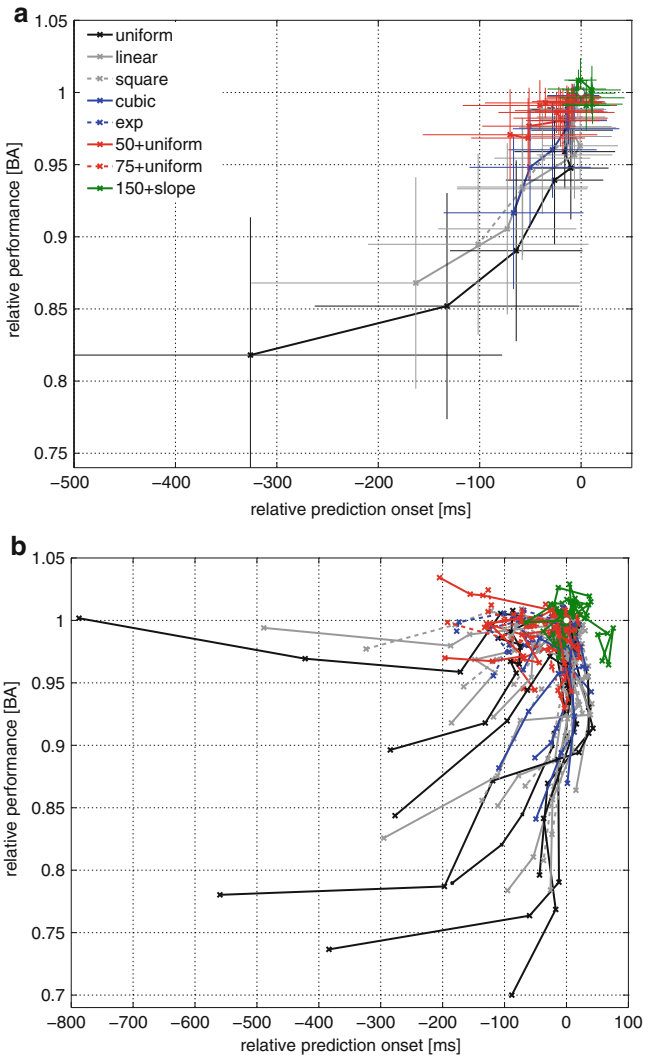

Fig. 4 Performance changes (BA and onset time) of postprocessing methods. The results are illustrated relative to the case where the scores were not further processed, illustrated as a *white dot* at (0,1). Each data point corresponds to a different $k \in \{1, 2, 4, 8, 12, 16, 20, 40, 60, 100\}$ (see text). In (**a**) the grand average results over all subjects are shown as mean and standard deviation for each k, respectively. Thus, there is one line for each method applied. In (**b**) the same results are shown for all subjects, separately

accuracy. The `150+slope` method with $k \in \{2, 4\}$ worked best on the average level and enhanced both, time point of detection and accuracy. On the single-subject level, the individual best method differed, so that the spectrum presented here can

serve as a general framework to *adjust* the movement prediction according to the respective application and/or the data of the individual subject.

6 Application: Ensemble Classification

This section illustrates how the postprocessing methods described here can be directly used in an application without additional investigations or prior knowledge. It should be noted that various alternative ways exist to use the outlined or similar postprocessing methods depending on the exact application with the respective constraints. Here, we try to give an intuition on their applicability using simple and straightforward approaches.

With the results presented in Sect. 5 we end up with two characteristics of the discussed methods for movement prediction: the best method is unknown in advance and a high subject-specificity is observed. One possibility to deal with this uncertainty in an application is to use *all* methods in an ensemble learning approach. Here, we apply this approach on the data (training and testing) described in Sect. 3. Accordingly, the ensemble consisted of 73 members (all eight postprocessing methods with nine values for k plus the reference point without postprocessing being equal to $k = 1$).

6.1 Procedure

Two simple ensemble strategies were used independently during training to obtain a single decision from all outputs of the ensemble members during testing: either the best individual method from the training was selected for the decision in a winner-take-all fashion (which is equal to viewing the ensemble learning as a grid search optimization), or the weights were distributed proportionally over all methods according to their individual behaviour on the training data. This evaluation has been performed after the re-adjustment of the score thresholds as described in Sect. 4.3. For each ensemble strategy (winner-take-all or distributed), three optimization criteria were respectively used: the individual classification performance (BA), the onset of the movement prediction (time), or a combination of both. For the latter, we added a value of 0.05 to the BA obtained for each 100 ms that the movement has been detected earlier. This means, that a perfect BA of 1.0 obtained 1,000 ms earlier would result in a total metric value of 1.5. The value of 0.05 has been arbitrarily determined from the overall results of all methods (Fig. 4) with the rationale that the performance did hardly improve, but instead dropped quickly in most cases, when the prediction has been made earlier. Therefore, we forced the combination to rely mainly on the classification performance getting a bonus when the classification has been correctly made earlier. Depending on the constraints of the individual application, this value may be chosen differently.

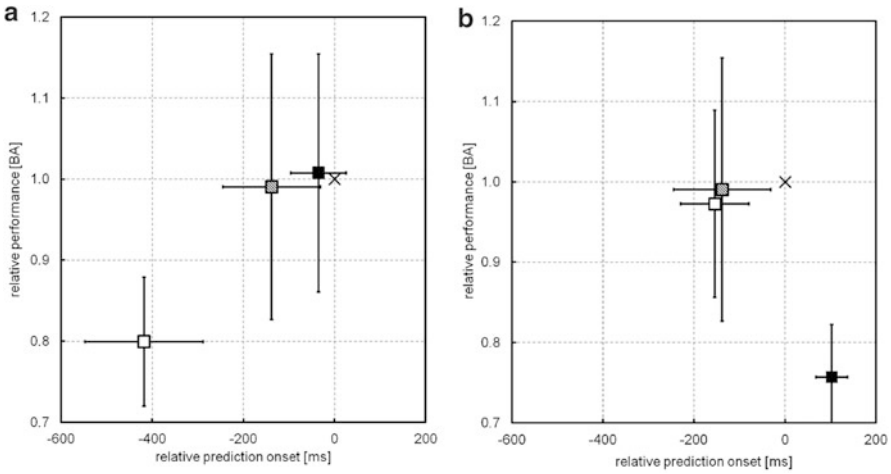

Fig. 5 Performance of the two ensemble approaches (mean and standard deviation) relative to reference performance. The ensemble was optimized according to best performance (*filled square*), earliest classification (*white square*) or a combination of the two (*striped square*, see text). The reference is marked with a cross at [0,1] (**a**) winner-take-all (**b**) distributed weighting

6.2 Ensemble: Results and Discussion

The resulting classification performances and prediction times of the ensemble approaches are depicted in Fig. 5. As is most obvious for the winner-take-all configuration, the ensemble is able to compensate for subject-specific differences in the *best method*, so that the postprocessing results on average in an earlier prediction. In the case of optimizing for time, the prediction was even about 400 ms earlier than the reference at the cost of accuracy. The figure also illustrates two more important factors when using ensembles: the optimization criterion and the distribution of the weights. The distributed weighting ensemble made the prediction slightly earlier when time was (at least partly) a criterion, but it failed when optimizing according to BA, because then the classification behaviour was governed by too many methods resulting in an overall later prediction with lower certainty.

7 Conclusions

Without any postprocessing, the classification of each window is performed independently of the neighbouring windows. However, we can see in the distributions of these classification outcomes that they intrinsically carry information about the probability of an upcoming event, like the rise in scores illustrated in Fig. 1. Here, we

use simple methods that can easily be applied during online movement prediction to make use of this knowledge and stabilize a single classification by the surrounding ones. As we have shown for individual methods and in the combined approach using the ensemble, the methodology introduced here can be used as a tool to improve classification outcomes.

On average we could observe an improvement of both, time point of detection and accuracy, using the `150+slope` method with small values of k. However, we found the most pronounced effects on the single-subject level: the proposed methods performed individually different. In general we could show that the applied postprocessing methods succeed for individual subjects in improving the accuracy and/or time point of prediction, but we could not find one straightforward solution in the current study for all subjects investigated. For most methods we found a trade-off between classification performance and the time point of prediction. This means for the application of such a movement predicting system, that one can indeed enhance the system, but has to carefully chose the postprocessing method and/or combination approach according to the requirements of the intended application. The finding of a subject specificity is consistent with results from other postprocessing methods [13], but it is still an open question where these effects particularly originate from. So far, existing postprocessing methods operate rather blindly on the data which may cause the individual differences.

From the view of an application, such a high subject-specificity can be principally dealt with using two strategies: either extra calibration time is used to find the best individual method, or the prediction itself is integrated in the application in a way that is flexible or robust enough to make use of the possible benefits illustrated here. Since the predictions obtained without postprocessing can serve as a reliable fallback option, this could be realized, e.g., by using a number of the proposed approaches on top and making the final prediction from the ensemble as we have exemplified in Sect. 6. As we have shown, a general approach can be implemented by performing a subject-specific optimization with an ensemble approach instead of using one method for all subjects. Then the performance can indeed be boosted resulting, e.g., in an earlier time point of prediction on the average level.

While most research is dedicated to improvement of the classifier and/or preprocessing algorithms, the idea of postprocessing classification outcomes as such is not completely new. Techniques for incorporating preceding probabilities to enhance the current prediction have been proposed [12, 15], but neither been evaluated in the way we did in the present study, nor been tested in an ensemble learning approach. Therefore and since SVM scores do not directly represent probabilities like in a Bayesian framework, a direct comparison with the methods we proposed is difficult. However, from the technical point of view, all of these methods have in common that they actually manipulate single prediction outcomes making use of the individual prediction history. Other techniques exist for postprocessing that rather operate on the global level by changing the decision criterion of the classifier or using additional thresholds. Here, threshold selection, dwell time optimization or debiasing of the score time course have been proposed [13, 14]. Due to their different nature, these techniques can be easily combined with what we proposed here, as

we already implicitly did by including threshold optimization (see Sect. 4.3) and selecting a stability criterion of 100 ms ($N = 10$; see Sect. 4.2 and Fig. 3), which can be interpreted as a kind of dwell time.

With the approach outlined here, other and more complex algorithms can of course be used, although they might have the possible drawback of being too computationally complex for an online predicting system. Generally, the methods applied here are not specific for the context of movement prediction, so they can be used in any context where such postprocessing may be helpful.

Acknowledgements This work was supported by the German Bundesministerium für Wirtschaft und Technologie (BMWi, grant FKZ 50 RA 1012 and grant FKZ 50 RA 1011). The authors like to thank Marc Tabie for providing us with the evaluation data.

References

1. Kornhuber HH, Deecke L. Hirnpotentialänderungen bei Willkürbewegungen und passiven Bewegungen des Menschen: Bereitschaftspotential und reafferente Potentiale. Pflüger's Archiv für die gesamte Physiologie des Menschen und der Tiere 1965;284(1):1–17.
2. Libet B, Gleason CA, Wright EW, Pearl DK. Time of conscious intention to act in relation to onset of cerebral activity (readiness-potential) the unconscious initiation of a freely voluntary act. Brain 1983;106(3):623–42.
3. Fabiani M, Gratton G, Federmeier KD. Event-related brain potentials: methods, theory, and applications. In: Cacioppo J, Tassinary LG, Berntson GG, editors. Handbook of psychophysiology. 3rd ed. Cambridge [u.a]: Cambridge University Press; 2007. p. 85–119.
4. Blankertz B, Dornhege G, Lemm S, Krauledat M, Curio G, Müller K. The Berlin brain-computer interface: machine learning based detection of user specific brain states. J Univ Comput Sci 2006;12(6):581–607.
5. Bai O, Rathi V, Lin P, Huang D, Battapady H, Fei DY, Schneider L, Houdayer E, Chen X, Hallett M. Prediction of human voluntary movement before it occurs. Clin Neurophysiol 2011;122(2):364–72. http://www.sciencedirect.com/science/article/pii/S1388245710005699.
6. Ahmadian P, Cagnoni S, Ascari L. How capable is non-invasive EEG data of predicting the next movement? A mini review. Front Hum Neurosci 2013;7:124.
7. Kirchner EA, Albiez J, Seeland A, Jordan M, Kirchner F. Towards assistive robotics for home rehabilitation. In: Chimeno MF, Solé-Casals J, Fred A, Gamboa H, editors. Proceedings of the 6th International Conference on Biomedical Electronics and Devices (BIODEVICES-13). Barcelona: SciTePress; 2013. p. 168–77.
8. Kirchner EA, Tabie M. Closing the gap: combined EEG and EMG analysis for early movement prediction in exoskeleton based rehabilitation. In: Proceedings of the 4th European Conference on Technically Assisted Rehabilitation - TAR 2013; 2013 March.
9. Folgheraiter M, Jordan M, Straube S, Seeland A, Kim SK, Kirchner EA. Measuring the improvement of the interaction comfort of a wearable exoskeleton. Int J Soc Robot 2012;4(3):285–302.
10. Folgheraiter M, Kirchner EA, Seeland A, Kim SK, Jordan M, Wöhrle H, Bongardt B, Schmidt S, Albiez J, Kirchner F. A multimodal brain-arm interface for operation of complex robotic systems and upper limb motor recovery. In: Vieira P, Fred A, Filipe J, Gamboa H, editors. Proceedings of the 4th International Conference on Biomedical Electronics and Devices (BIODEVICES-11). Rome: SciTePress; 2011. p. 150–62.

11. Seeland A, Woehrle H, Straube S, Kirchner EA. Online movement prediction in a robotic application scenario. In: 6th International IEEE EMBS Conference on Neural Engineering (NER). San Diego, CA: IEEE; 2013. p. 41–4
12. Lemm S, Schäfer C, Curio G. BCI competition 2003–data set III: probabilistic modeling of sensorimotor mu rhythms for classification of imaginary hand movements. IEEE Trans Biomed Eng 2004;51(6):1077–80. http://ieeexplore.ieee.org/xpl/articleDetails.jsp?arnumber=1300806.
13. Mohammadi R, Mahloojifar A, Coyle D. A combination of pre- and postprocessing techniques to enhance self-paced BCIs. Adv Hum Comput Interact 2012;2012:3:1–10. http://www.hindawi.com/journals/ahci/2012/185320/abs/.
14. Solis-Escalante T, Müller-Putz G, Pfurtscheller G. Overt foot movement detection in one single laplacian EEG derivation. J Neurosci Meth 2008;175(1):148–53.
15. Zhu X, Wu J, Cheng Y, Wang Y. GMM-based classification method for continuous prediction in brain-computer interface. In: Proceedings of the 18th International Conference on Pattern Recognition - ICPR '06, Washington, DC: IEEE Computer Society; 2006. vol. 01. p. 1171–4. http://dx.doi.org/10.1109/ICPR.2006.610.
16. Vapnik VN. The nature of statistical learning theory. New York: Springer; 1995.
17. Tabie M, Kirchner EA. EMG onset detection – comparison of different methods for a movement prediction task based on EMG. In: Alvarez S, Solé-Casals J, Fred A, Gamboa H, editors. Proceedings of the 6th International Conference on Bio-inspired Systems and Signal Processing (BIOSIGNALS-13). Barcelona: SciTePress; 2013. p. 242–7.
18. Krell MM, Straube S, Seeland A, Wöhrle H, Teiwes J, Metzen JH, Kirchner EA, Kirchner F. pySPACE - a signal processing and classification environment in Python. Front Neuroinf 2013;7(40). http://www.frontiersin.org/neuroinformatics/10.3389/fninf.2013.00040/abstract, https://github.com/pyspace.
19. Rivet B, Souloumiac A, Attina V, Gibert G. xDAWN algorithm to enhance evoked potentials: application to brain-computer interface. IEEE Trans Biomed Eng 2009;56(8):2035–43. http://dx.doi.org/10.1109/TBME.2009.2012869.
20. Chang CC, Lin CJ. LIBSVM: a library for support vector machines. ACM Trans Intell Syst Technol 2011;2:27:1–27. Software available at http://www.csie.ntu.edu.tw/~cjlin/libsvm.
21. Kubat M, Holte RC, Matwin S. Machine learning for the detection of oil spills in satellite radar images. Mach Learn 1998;30(2–3):195–215. http://dx.doi.org/10.1023/A:1007452223027.
22. Straube S, Krell MM. How to evaluate an agent's behaviour to infrequent events? – reliable performance estimation insensitive to class distribution. Front Comput Neurosci 2014;8(43). http://www.frontiersin.org/computational_neuroscience/10.3389/fncom.2014.00043/abstract.

Index

A.R. Londral et al. (eds.), *Neurotechnology, Electronics, and Informatics*,
Springer Series in Computational Neuroscience 13, DOI 10.1007/978-3-319-15997-3